

A HIGH-ORDER LOW-ORDER ALGORITHM WITH
EXPONENTIALLY-CONVERGENT MONTE CARLO FOR THERMAL
RADIATIVE TRANSFER PROBLEMS

A Dissertation

by

SIMON RAY BOLDING

Submitted to the Office of Graduate and Professional Studies of
Texas A&M University
in partial fulfillment of the requirements for the degree of

DOCTOR OF PHILOSOPHY

Chair of Committee,	Jim Morel
Committee Members,	Ryan McClarren
	Jean Ragusa
	Jean-Luc Guermond
Head of Department,	Yassin Hassan

May 2017

Major Subject: Nuclear Engineering

Copyright 2017 Simon Ray Bolding

ABSTRACT

We have implemented a new high-order low-order (HOLO) algorithm for solving thermal radiative transfer problems. The low-order (LO) system is based on spatial and angular moments of the transport equation and a linear-discontinuous finite-element spatial representation, producing equations similar to the standard S_2 equations. The LO solver is fully implicit in time and efficiently resolves the non-linear temperature dependence at each time step. The HO solver utilizes exponentially-convergent Monte Carlo (ECMC) to give a globally accurate solution for the angular intensity to a fixed-source, pure absorber transport problem. This global solution is used to compute consistency terms, which require the HO and LO solutions to converge towards the same solution. The use of ECMC allows for the efficient reduction of statistical noise in the MC solution, reducing inaccuracies introduced through the LO consistency terms. We compare results with an implicit Monte Carlo (IMC) code for one-dimensional, gray test problems and demonstrate the efficiency of ECMC over standard Monte Carlo in this HOLO algorithm.

1. INTRODUCTION

We have developed and implemented a new high-order low-order (HOLO) algorithm for solving thermal radiative transfer (TRT) problems. This algorithm has several desirable properties that improve on current computational methods for solving TRT problems. In particular, our HOLO method utilizes an exponentially-convergent Monte Carlo (ECMC) algorithm to solve the associated radiation transport equation. The ECMC method significantly decreases the statistical noise associated with MC calculations to TRT problems. In addition, we use a nonlinear low-order (LO) system that allows for the nonlinear dependencies in the system to be efficiently resolved. The LO system is formed such that it preserves the accuracy of the ECMC treatment of particle transport, upon convergence of the outer iterations. The HOLO algorithm has been developed and implemented for a simplified model with one spatial dimension and frequency-integrated equations.

The LO equations are formed with finite-element (FE) based spatial moments and angular moments over each half-range. A linear-discontinuous representation is used to discretize the temperature field. The LO equations are similar to S_2 equations, but contain intensity-weighted angular averages that are estimated via the HO solver. The LO solver is fully implicit in time and efficiently resolves the non-linear temperature dependence at each time step. The HO transport problem is a fixed-source, pure absorber transport problem, with sources defined by the previous LO solve. This transport equation is solved with ECMC simulation to produce a globally accurate solution. This global solution is used to compute consistency terms, which require the HO and LO solutions to converge towards the same solution. The use of ECMC allows for the efficient reduction of statistical noise in the MC solution,

reducing inaccuracies introduced through the LO consistency terms.

The research herein provides a new HOLO algorithm for radiative transfer. In this work, we propose an S_2 -like LO operator [47] in conjunction with an exponentially-convergent MC (ECMC) method [29] for the HO solver. Our LO system and approach to enforcing consistency contrast greatly from the typical formulation in [41, 40, 28]. We have derived the LO operator directly from the transport equation, using a linear-discontinuous finite-element (LDFE) spatial discretization. Exponentially-convergent Monte Carlo (ECMC)[29, 3] provides an iterative algorithm that can efficiently reduce statistical noise to acceptable levels with significantly less particle histories than standard MC. The ECMC Method has been applied to 1D steady state neutronics problems previously [29]. In particular, ECMC is exceptionally efficient in time-dependent TRT problems because information about the intensity from the previous time step can be used as an accurate initial guess for the new end of time step intensity. However, implementation of ECMC is non-trivial, requiring a finite-element representation of the solution in all phase-space variables that are being sampled with MC. The method contains many of the desired qualities, such as preserving the equilibrium diffusion limit, preserving the maximum principle, and in particular, providing high-fidelity MC solution to the TRT equations in an efficient manner.

Sufficient MC histories must be performed to eliminate statistical noise in the consistency terms that can contaminate the LO solution. Exponentially-convergent Monte Carlo (ECMC)[29, 3] provides an algorithm that can efficiently reduce statistical noise to the same order as the HOLO iteration error with significantly less particle histories than standard MC. In particular, ECMC is exceptionally efficient in time-dependent TRT problems because information about the intensity from the previous time step can be used as an accurate initial guess for the new end of time

step intensity. Additionally, no particle histories are required in regions where the radiation and material energy field are in equilibrium, similar to [41]. However, implementation of ECMC is non-trivial, requiring a finite-element representation of the solution in all phase-space variables that are being sampled with MC. The fundamental transport of particles is the same as standard Monte Carlo transport codes, but the source will now contain positive and negative weight particles.

In this work, we demonstrate the utility of an S_2 -like LO operator [47] in conjunction with an ECMC method [29] for the HO solver. The ECMC algorithm uses information about the intensity from the previous time step to reduce statistical noise to the same order as the HOLO iteration error with significantly less particle histories than standard MC simulations, with less computational cost than IMC per history. We have derived the LO operator directly from the transport equation, using a linear-discontinuous (LD) finite-element (FE) spatial discretization for the HO and LO solutions. Herein we describe the algorithm and present results for 1D, gray test problems.

REWRITE: We have also investigated several extensions and improvements of this method. First, an alternative solution method to the LO equations is explored, using an iterative source iteration method with linear diffusion synthetic acceleration. The goal is to present a solution method for the S_2 -like equations that is more extendable to higher dimensions. Additionally, we have investigated solution methods to resolve issues when the optically thick mesh cells present intensity gradients that are too difficult to resolve with the LDFE interior mesh representation. In the HO equations, we add artificial sources that make the solution more easily representable by the chosen mesh resolution. Finally, higher accuracy in the time variable is investigated by including the time variable in the ECMC transport algorithm. This can produce more accuracy in the transport of particles across optically thin

regions, although a projection error in the intensity is still incurred between time steps. Throughout, we compare results with an implicit Monte Carlo (IMC) code for one-dimensional, gray test problems and demonstrate the efficiency of ECMC over standard Monte Carlo in this HOLO algorithm.

In addition to estimating the angular consistency terms, the HO intensity estimates a relation between volume and face-averaged intensities to eliminate the remaining unknowns from the equations. The goal is for the LO moments to reproduce the HO moments more accurately than the LDFE discretization, although additional statistical noise is introduced through face-based tallies. A projection of the intensity that is separate from the linear extrapolation allows for an accuracy projection of the MC solution at faces, which is incorporated through the HO spatial closure of the LO equations discussed in Sec. 3.6. Additionally, the independent solution at faces allows for face-averaged consistency terms (e.g., Eq. (3.15)) to be directly evaluated.

In the remainder of this chapter, a brief background on TRT problems is given, before the simplified model that will be used for the remainder of the work is derived. Then, related work on MC and HOLO solution methods for TRT are discussed. Herein, a brief description of thermal radiative transfer and the model problem are given, followed by a discussion of the standard Monte Carlo solution method and other related research. Finally, a detailed outline of the dissertation is given.

Most of the work discussed in this dissertation were previously published in [2].

1.1 Thermal Radiative Transfer Background

Thermal radiative transfer (TRT) physics are used to model the time-dependent coupling between a photon radiation field and a high-temperature material, which is typically a plasma. The desired transient unknowns are the spatial energy-density

distributions of the radiation and material. As photons transport through the medium, they interact through scattering and absorption by the material, depositing momentum and energy. The material is heated through absorption of photons and is cooled by emission of thermal x-ray photons into the radiation field. The emission process is a strongly nonlinear function of temperature [25]. Additionally, the material properties are typically a function of temperature, in particular the absorption cross section. The temperature-dependent material properties and absorption and reemission physics lead to systems that require accurate modeling of photon transport through a mix of streaming and optically-thick, diffusive regions.

Accurate modeling of TRT physics becomes relevant in the high-energy, high-density physics regime. Radiative transfer is a dominant form of heat transfer in high-temperature systems, where the material temperature is $O(10^6)$ K or higher. Typical computational applications of TRT include simulation of inertial confinement fusion and astrophysics phenomena. In most applications where TRT is important, the fluid material is typically in motion and exchanges momentum with the radiation field. In this work, we neglect motion of the material, which would require inclusion of hydrodynamics in our model [25]. However, our LO equations are well-suited for coupling to material motion via typical operator-splitting methods for radiation-hydrodynamic systems [34, 16].

1.1.1 The Equations of Thermal Radiative Transfer

First, the photon radiation field, with the appropriate units used throughout this work, is characterized. Photons transporting through a material are described by the particle position vector \mathbf{r} (cm), direction vector $\boldsymbol{\Omega}$ (str, i.e., steradians), time t (sh, where $1 \text{ sh} \equiv 10^{-8} \text{ s}$), and frequency ν (Hz). The primary radiation unknown is the angular intensity $I(\mathbf{r}, \boldsymbol{\Omega}, \nu, t)$ ($\text{jk cm}^{-2} \text{ s}^{-1} \text{ Hz}^{-1} \text{ str}^{-1}$), which represents a

distribution function of energy contained in the radiation field, per unit of phase space. We use the energy unit jerks (jk), where $1 \text{ jk} = 10^9 \text{ joules}$. The intensity can be related to the volumetric density of photons $N(\mathbf{r}, \mathbf{\Omega}, \nu, t)$ (photons $\text{cm}^{-3} \text{ Hz}^{-1} \text{ str}^{-1}$) via the relation $I(\mathbf{r}, \mathbf{\Omega}, \nu, t) = ch\nu N(\mathbf{r}, \mathbf{\Omega}, \nu, t)$, where c is the speed of light (cm sh^{-1}) and h is Planck's constant. The angular intensity is a useful quantity because it is directly related to reaction rates.

The governing conservation equation for the radiation field is a transport equation given by [25, 22, 42]

$$\frac{1}{c} \frac{\partial I(\mathbf{r}, \mathbf{\Omega}, \nu, t)}{\partial t} + \mathbf{\Omega} \cdot \nabla I(\mathbf{r}, \mathbf{\Omega}, \nu, t) + \sigma_t(\mathbf{r}, \nu) I(\mathbf{r}, \mathbf{\Omega}, \nu, t) = \int_0^\infty \int_{4\pi} \sigma_s(\mathbf{\Omega}' \rightarrow \mathbf{\Omega}, \nu' \rightarrow \nu) \phi(\mathbf{r}', \nu', t) d\Omega' d\nu' + \sigma_a(\mathbf{r}, \nu) B_\nu(\mathbf{r}, \nu, T), \quad (1.1)$$

where

$$B_\nu(\mathbf{r}, \nu, T) = \frac{2h\nu^3}{c^2} \frac{1}{e^{h\nu/T} - 1} \quad (1.2)$$

is the black-body Planckian emission spectrum at temperature T (keV) [25], and the macroscopic scattering, absorption, and total cross sections are σ_s , σ_a , and σ_t , respectively. The scattering source includes integration over all possible incoming angles $\mathbf{\Omega}'$ in differential solid angle $d\Omega'$. The absorption cross section σ_a is typically a strong function of temperature, i.e., $\sigma_a \equiv \sigma_a(T)$. Following standard notation, we report temperatures in units of keV as an effective energy, obtained by multiplying by the Boltzmann constant k_B [25]. Thus, all material temperatures are $T \equiv T_K k_B$, where k_B is the Boltzmann constant (keV K^{-1}) and T_K is the temperature in kelvin.

The material is characterized by the material internal energy as a function of position. The internal energy e is related to the material temperature T through an equation of state. In this work, a perfect gas equation of state is assumed [36],

which produces the relation $\rho c_v T = e$, where ρ is the material mass density and c_v is the specific heat. Thus, we will use $T(\mathbf{r}, t)$ as the primary unknown to describe the material energy distribution. The material energy conservation equation is

$$\rho(\mathbf{r})c_v(\mathbf{r})\frac{\partial T(\mathbf{r}, t)}{\partial t} = \int_0^\infty \left(\int_{4\pi} \sigma_a I(\mathbf{r}, \boldsymbol{\Omega}, \nu, t) d\Omega - \sigma_a 4\pi B_\nu(\mathbf{r}, \nu, T) \right) d\nu \quad (1.3)$$

In derivation of the above equations, the conditions of local thermodynamic equilibrium were assumed, i.e., the emission source is described point-wise by the Planck function at the temperature at that position, and the material is well-described by the local temperature [25, 42]. The emission source is a non-linear function of temperature and is proportional to T^4 after integration over frequency.

1.1.2 Derivation of 1D Grey Model

At this point, we introduce the simplified equations that will be used in the remainder of this work. First, the solutions are assumed to only vary in one spatial dimension using Cartesian coordinates, referred to as the 1D slab geometry [22]. The position is described by a single coordinate x and the direction of particle travel is described by μ , which is the cosine of the angle between the particle direction and the positive x axis. The angular intensity is assumed symmetric in angle azimuthally about the x axis. To simplify the equations, the equations are integrated over all frequencies. We also assume that the material properties are independent of photon frequency, or equivalently we know the weighting spectrum of the frequency integrated cross sections. Finally, we assume physical scattering is isotropic in angle. With these assumptions, integration over the azimuthal angle and all frequencies,

with algebraic manipulation, ultimately yields the 1D grey equations [42, 25]

$$\frac{1}{c} \frac{\partial I(x, \mu, t)}{\partial t} + \mu \frac{\partial I(x, \mu, t)}{\partial x} + \sigma_t I(x, \mu, t) = \frac{\sigma_s}{2} \phi(x, t) + \frac{1}{2} \sigma_a a c T^4(x, t) \quad (1.4)$$

$$\rho c_v \frac{\partial T(x, t)}{\partial t} = \sigma_a \phi(x, t) - \sigma_a a c T^4(x, t). \quad (1.5)$$

The equations have associated incident boundary conditions for the angular intensity:

$$I(0, \mu) = I^{inc,+}(\mu), \quad \mu > 0 \quad (1.6)$$

$$I(X, \mu) = I^{inc,-}(\mu), \quad \mu < 0, \quad (1.7)$$

for a spatial domain spanning $0 \leq x \leq X$. In the above equations the fundamental unknowns are the material temperature $T(x, t)$ and the grey angular intensity $I(x, \mu, t) = \int_0^\infty I(x, \mu, \nu, t) d\nu$. The mean radiation intensity $\phi(x, t) = \int_{-1}^1 I(x, \mu, t) d\mu$ is related to the radiation energy density E (J m^{-3}) by the relation $E = \phi/c$. The integral of $B_\nu(\mathbf{r}, \nu, T)$ over all frequencies and angles produced the grey Planckian emission source $\sigma_a a c T^4$ [25] in Eq. (1.5), where $a = 0.01372 \text{ J m}^{-3} \text{ K}^{-4}$ is the radiation constant, which is proportional to the Stefan-Boltzmann constant. The term $\sigma_a \phi$ is the rate of energy absorption by the material, whereas the emission term represents losses to the material internal energy. We have developed and tested our algorithm for efficient solution to Eq. (1.4) and (1.5).

1.1.3 The Equilibrium Diffusion Limit

A critical aspect for any numerical solution to the thermal radiative transfer equations is preservation of the asymptotic, equilibrium diffusion limit (EDL) [26, 21]. In the EDL, the material becomes optically thick and increasingly diffusive, as σ_a becomes large and ρc_v becomes small. The solution approaches equilibrium with $I(x, \mu) = \frac{1}{2} a c T^4$, where the distribution of the solution is well described by the

material temperature [21]. For problems in this limit, spatial mesh cells that resolve the spatial variation of the solution are still $O(100)$ mfps or greater; the solution typically varies relatively smoothly in space. Discretization schemes of the transport equation must correctly limit to the appropriate discretized diffusion equation in the EDL. Spatial discretizations that do not preserve the EDL can produce inaccurate solution, even though the mesh size should accurately capture the variation of the solution, with inaccuracies that are much greater than expected from truncation error. Such methods require spatial mesh resolution on the order of a mfp [26]. The EDL regime is typical in applications of TRT, so discretizations must preserve this limit to prevent unnecessarily fine mesh resolutions.

1.2 Previous and Related Work

This section describes related work on Monte Carlo solution to the TRT equations, as well as some important properties that numerical solution to TRT equations must preserve. The Monte Carlo (MC) method [31] is a standard computational method in the field of radiation transport. It has been used to great success, providing high-accuracy solutions to particle transport problems described by the linear Boltzmann transport equation for many decades. The application of MC to the linear Boltzmann equation is well documented in literature [35, 31, 22]. The Monte Carlo method samples the underlying physics distributions to estimate the average behavior of a field of particles. This can provide highly-accurate results, in particular for treatment of the angular variable associated with particle transport problems. Detailed descriptions of MC simulation of particle tracking, sampling of interactions, etc. can be found in literature [35, 43, 31].

With respect to TRT problems, the temperature equation is almost always solved deterministically to produce a linear particle transport equation. Monte carlo solu-

tion to this transport equation can introduce large statistical noise into the material temperature distribution, which is undesirable when coupling to other physics, e.g., in radiation hydrodynamics. To improve the efficiency of MC solutions, hybrid MC methods utilize a deterministic solution to accelerate the MC solution.

In the remainder of this section, we detail the standard method for MC solution to TRT equations, the implicit Monte Carlo (IMC) method, and then discuss related moment-based acceleration and other alternative solution methods. We also discuss the residual Monte Carlo (RMC) method, which is similar to the HO solver in our method.

1.2.1 The Implicit Monte Carlo Method

The IMC method [11, 43] is the standard approach for applying the MC method to TRT problems. The IMC method partially linearizes Eq. (1.4) & Eq. (1.5) over a discrete time step, with material properties evaluated at the previous-time-step temperature. Linearization of the system produces a linear transport equation that can be solved with MC simulation. The transport equation contains an approximate emission source and an effective scattering cross section representing absorption and reemission of photons over a time step. The transport equation is solved with MC simulation to advance the distribution of radiation to the end of the time step and determine the energy absorbed by the material over the time step. The energy absorption by the material is tallied over a discrete spatial mesh, computed with cell-averaged quantities. Integration of the time-variable is treated continuously for radiation variables over the time step via MC sampling, but the linearized Planckian source in the transport equation is based on a time-discrete approximation.

The IMC method has some notable limitations. In optically thick regions, or for large time steps, the effective scattering dominates interactions. In these diffusive

regions IMC becomes computationally expensive. Acceleration methods typically attempt to improve efficiency by allowing particles to take discrete steps through optically-thick regions based on a spatially-discretized diffusion approximation [13, 6]. In IMC, temperature-dependent material properties, in particular cross sections, are evaluated at the previous-time step temperature. These lagged cross sections can produce inaccurate solutions but do not cause stability issues.

An important aspect for numerical simulation of TRT equations is preservation of the discrete maximum principle (MP). The maximum principle states that the material temperature and mean intensity in the interior of the domain should be bounded by the solution at the boundaries of the domain, in the absence of interior energy sources [44, 19]. The analytic solution to the TRT equations satisfies a maximum principle [19], so we desire numerical approximations that preserve the MP in a discrete sense, for each time step. For some problems, the IMC method can yield non-physical results that violate the MP if the time step size is too large or the cell size is too small [44]. The violation of the maximum principle results in the material temperature being artificially higher than the effective radiation temperature. The violation by IMC is caused by the approximate linearization of the end-of-time-step emission source; the emission source is not truly implicit in time. The linearized estimate of the emission source typically can not be iteratively improved due to the high computational cost of the MC transport. The work in [12] uses less-expensive MC iterations to produce an implicit system which prevents this from happening, but the method has very slow iterative convergence in diffusive problems.

In IMC the material and radiation energy fields are discretized spatially to solve for cell-averaged values. Inaccurate spatial representation of the emission source over a cell can result in energy propagating through the domain artificially fast, yielding non-physical results that are often referred to as “teleportation error” [24].

The IMC method uses a fixup known as source tilting to mitigate this problem. Source tilting reconstructs a more accurate linear-discontinuous representation of the emission source within a cell based on the cell-averaged material temperatures in adjacent cells. Recent work in IMC has incorporated a linear-discontinuous finite-element representation directly into the discretization of the material temperature equation [46].

For TRT simulations, inaccurate spatial representation of the emission source over a cell can result in energy propagating through the domain artificially fast, yielding non-physical results referred to as “teleportation error” [24]. The IMC method uses a fixup known as source tilting to mitigate this problem. Source tilting reconstructs a more accurate linear-discontinuous representation of the emission source within a cell based on the cell-averaged material temperatures in adjacent cells. This linear reconstruction is also necessary to preserve the asymptotic equilibrium diffusion limit (EDL), at least for a more general time step size and class of problems than for a piece-wise constant representation [5].

1.2.2 Previous work on moment-based acceleration methods

An alternative application of MC to the TRT equations is moment-based hybrid MC methods. Recent work has focused on so-called high-order low-order (HOLO) methods [40, 28, 41, 3, 2]. These methods involve fixed-point iterations between high-order (HO) MC solution of a transport equation and a deterministic LO system. The low-order (LO) operator is based on angular moments of the transport equation, formulated over a fixed spatial mesh. Physics operators that are time consuming for MC to resolve, e.g., absorption-reemission physics, are moved to the LO system. The reduced angular dimensionality of the system and Newton methods allow for non-linearities in the LO equations to be fully resolved efficiently [40, 28]. The high-

order (HO) transport problem is defined by Eq. (1.4), with sources estimated from the previous LO solution. The high-order (HO) transport equation is solved via MC to produce a high-fidelity solution for the angular intensity. The MC estimate of the angular intensity is used to estimate consistency terms, present in the LO equations, that require the LO system to preserve the angular accuracy of the MC solution. These consistency terms are present in all spatial-regions of the problem, requiring statistical variance to be reduced sufficiently throughout the entire domain of the problem. The LO equations are typically based on nonlinear Diffusion Acceleration (NDA) [40, 28].

Another area of related research is the application of residual Monte Carlo to TRT problems. The goal of these methods is to solve an auxiliary transport equation with MC simulation for the error in some estimate of the intensity. The error is then added to the estimate of the solution, which can produce an overall solution for the intensity that has less statistical noise than solution of the original transport equation would produce. The work in [41] used residual MC as a HO solver for 1D grey TRT problems. In [41], the residual is formed with a fixed estimate of the solution, based on the previous time intensity, such that only sources on the faces of cells must be sampled. This reduces the dimension of the phase-space to be sampled [41]. The RMC algorithm demonstrated impressive reduction in statistical variance for slowly varying solutions. However, a piecewise constant representation is used for the space-angle representation of the intensity, which does not preserve the EDL and can be inaccurate in angularly complex regions of the problem.

Similar to RMC, a difference formulation has been applied to another algorithm known as the symbolic IMC method (SIMC), for the case of 1D frequency-dependent problems [14]. SIMC forms a standard FE solution to the material energy balance equation, and uses symbolic weights in the MC transport to solve for expansion

coefficients. The difference formulation modifies the transport equation to solve for unknowns representing the deviation of the intensity from equilibrium with the material energy. The difference formulation was also applied to a linear-discontinuous FE spatial representation of the emission source, demonstrating accuracy in the EDL [15]. Both [14] and [41] produced minimal statistical noise in slowly varying problems where the behavior of the system is near equilibrium.

1.3 Outline of the Disertation

In Chapter 2 an overview of the outer HOLO algorithm and how the HO and LO systems interact is given. For the majority of this work, time-discretized equations will be assumed; in Chapter ?? a higher-accuracy MC time treatment is investigated. Chapter 3 gives a detailed derivation of the LO equations and how they are solved. Then, Chapter 4 details the ECMC algorithm that is used to solve the HO transport problem.

2. OVERVIEW OF THE HOLO ALGORITHM

For simplicity, our HOLO method will use a backward Euler (BE) discretization in time, as well as constant specific heats and cell-wise constant cross sections. The time-discretized equations are

$$\mu \frac{\partial I^{n+1}}{\partial x} + \left(\sigma_t^{n+1} + \frac{1}{c\Delta t} \right) I^{n+1} = \frac{\sigma_s}{2} \phi^{n+1} + \frac{1}{2} (\sigma_a a c T^4)^{n+1} + \frac{I^n}{c\Delta t} \quad (2.1)$$

$$\rho c_v \frac{T^{n+1} - T^n}{\Delta t} = \sigma_a^{n+1} \phi^{n+1} - \sigma_a a c (T^4)^{n+1}, \quad (2.2)$$

where Δt is the uniform time step size, the superscript n is used to indicate the n -th time step. Cross sections are evaluated at the end of time step temperature, i.e., $\sigma_a^{n+1} \equiv \sigma_a(T^{n+1})$. It is noted that in IMC the time derivative in Eq. (??) is typically treated continuously using time-dependent MC over each time step. Our HO transport equation is discrete in time for simpler application of ECMC and to avoid difficulties in coupling to the fully-discrete LO solver. However, this does introduce some artificial propagation of energy due to the implicit time differencing in optically thin regions.

The directionality of the S_2 equations is convenient for closing the equations spatially with a discontinuous trial space.

In the HOLO context, the LO solver models isotropic scattering and resolves the material temperature spatial distribution $T(x)$ at each time step. The LO equations are formed via half-range angular and spatial moments of Eq. (2.1) and Eq. (2.2). The spatial moments are formed over a finite-element mesh and linear-discontinuous representation of the temperature is used to close the system. The angular treatment in the LO equations has the same form as those used in the hybrid- S_2 method in [47],

with consistency parameters that represent angularly-weighted averages of the intensity. These consistency parameters are analogous to a variable Eddington factor [4]. If the angular consistency parameters were exact, then the LO equations are exact, neglecting spatial discretization errors. These consistency parameters are lagged in each LO solve, estimated from the previous HO solution for $I^{n+1}(x, \mu)$, as explained below. For the initial LO solve for each time step, the parameters are calculated with $I^n(x, \mu)$. The discrete LO equations always conserve total energy, independent of the accuracy of the consistency terms. The LO system uses a LDFE spatial discretization for the temperature and half-range scalar intensities. The LDFE spatial discretization should correctly preserve the equilibrium diffusion limit, a critical aspect for TRT equations [21, ?]. Additionally, the implicit time discretization with sufficient convergence of the nonlinear emission source will ensure that the method will not exhibit maximum principle violations [19].

We expect our method, with a fully implicit time discretization, to preserve the MP with sufficient convergence of the nonlinear emission source [19].

If the angular consistency parameters were estimated exactly, then the LO equations preserve the exact angular-averaged solution, neglecting spatial discretization errors. These consistency parameters are lagged in each LO solve, estimated from the previous HO solution for the intensity, or from a previous time step. The discrete LO equations always conserve total energy, independent of the accuracy of the consistency terms. It is noted that our LO operator is different from the nonlinear diffusion acceleration (NDA) methods used by other HOLO methods [41, 28, 40]. In NDA methods, an artificial term is added to the LO equations to enforce consistency and estimated using a previous HO solution. In our method we have simply algebraically manipulated space-angle moment equations to produce our consistency terms, which will hopefully produce more stability in optically-thick regions where

NDA methods demonstrate stability issues.

It is noted that the LD projection of the HO solution does not produce the same moments, because MC was used to obtain this projection, the outflow will not agree with the LO equations. For example, the upwinding inflow from a previous cell does not match the actual energy that flowed through that surface due to MC noise.

The solution to the LO system is used to construct a LDFE spatial representation of the isotropic scattering and emission sources on the right hand side of Eq. (2.1). The LDFE representation of the emission source mitigates teleportation error. This defines a fixed-source, pure absorber transport problem for the HO operator. This HO transport problem represents a characteristic method that uses MC to invert the continuous streaming plus removal operator with an LDFE representation of sources; the representation of sources is similar to the linear moments method discussed in [7]. We will solve this transport problem using ECMC. The output from ECMC is $\tilde{I}^{n+1}(x, \mu)$, a space-angle LDFE projection of the exact solution $I^{n+1}(x, \mu)$ to the described transport problem. Once computed, $\tilde{I}^{n+1}(x, \mu)$ is used to directly evaluate the necessary consistency parameters for the next LO solve. Since there is a global, functional representation of the angular intensity, LO parameters are estimated using quadrature and do not require additional tallies. The HO solution is not used to directly estimate a new temperature at the end of the time step; it is only used to estimate the angular consistency parameters for the LO equations, which eliminates typical operator splitting stability issues that require linearization of the emission source.

The process of performing subsequential HO and LO solves, within a single time step, can be repeated to obtain an increasingly accurate solution for $\phi^{n+1}(x)$ and $T^{n+1}(x)$. Thus, the HOLO algorithm, for the n -th time step, is

1. Perform a LO solve to produce an initial guess for $T^{n+1,0}(x)$ and $\phi^{n+1,0}(x)$, based on consistency terms estimated with \tilde{I}^n .
2. Solve the HO system for $\tilde{I}^{n+1,k+1/2}(x, \mu)$ with ECMC, based on the current LO estimate of the emission and scattering sources.
3. Compute LO consistency parameters with $\tilde{I}^{n+1,k+1/2}$.
4. Solve the LO system with HO consistency parameters to produce a new estimate of $\phi^{n+1,k+1}$ and $T^{n+1,k+1}$.
5. Optionally repeat 2 – 4 until desired convergence is achieved.
6. Store $\tilde{I}^n \leftarrow \tilde{I}^{n+1}$, and move to the next time step.

where the superscript k denotes the outer HOLO iteration. The consistency terms force the HO and LO solutions for $\phi^{n+1}(x)$ to be consistent to the order of the current HOLO iteration error, as long as the LDFE spatial representation can accurately represent $\phi(x)$ and $T(x)$.

3. THE MOMENT-BASED LOW-ORDER EQUATIONS

The LO equations are based on moments, i.e., integrals of the equations, to produce a lower-dimensional system. The equations incorporate extra parameters, referred to as consistency terms, that allow for the equations to preserve the accuracy (particularly in angle) of the HO solver, which is detailed in the next chapter. The formulation of the LO equations is similar to a discontinuous FE method. Weighted integrals of the equations are taken using weight functions that have local support. The equations are written with element-wise moments of I and T as unknowns. Leaving the solution in this form allows for use of information from a previous HO solution to eliminate auxiliary unknowns from the equations. This is different than a standard Galerkin or collocation FE method [26, 27] where a functional form of the solution is directly assumed. The final equations will have a similar form to S_2 equations, but we have not used a collocation method in angle, which should limit ray effects [27, 22] in higher spatial dimensions. The backward Euler time discretization is used throughout this section. Chapter 8 includes HO treatment of the radiation variables in the time variable.

The remainder of this chapter is structured as follows: the general moments will be derived and then the use of HO information to close the system in angle is discussed. We then detail two separate spatial closures: a standard linear-discontinuous finite-element (LDFE) method [26] and the use of the HO solution to eliminate extra spatial unknowns from the LO equations.

3.1 Forming the Space-Angle Moment Equations

3.1.1 LO Spatial mesh and Finite-Element Spatial Moments

The LO equations are formulated over a FE mesh. The domain for the i -th spatial element (or cell) has support $x \in [x_{i-1/2}, x_{i+1/2}]$ with width $h_i = x_{i+1/2} - x_{i-1/2}$ and cell center $x_i = x_{i-1/2} + h_i/2$. There is a total of N_c elements, spanning the spatial domain $0 \leq x \leq X$. For simplicity, this spatial mesh is fixed throughout the simulation. Mesh adaptation is only applied in the HO solver, where applicable.

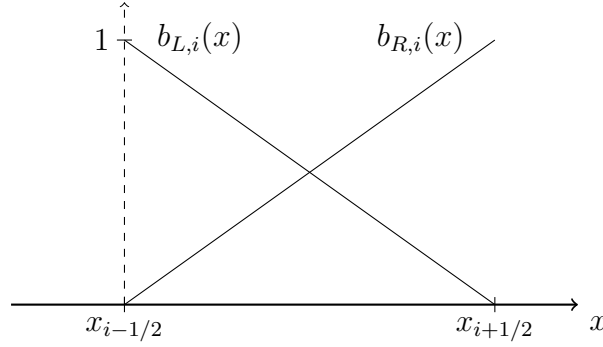


Figure 3.1: Illustration of linear finite element basis functions $b_{L,i}(x)$ and $b_{R,i}(x)$ for spatial element i .

The spatial moments are defined by integrals weighted with the standard linear finite element (FE) interpolatory basis functions. An illustration of the two linear FE basis functions for the i -th element (or cell) is given in Fig. 3.1. The left basis function is defined as

$$b_{L,i}(x) = \begin{cases} \frac{x_{i+1/2} - x}{h_i} & x_{i-1/2} \leq x \leq x_{i+1/2} \\ 0 & \text{elsewhere} \end{cases}, \quad (3.1)$$

corresponding to the node $x_{i-1/2}$. The right basis function is

$$b_{R,i}(x) = \begin{cases} \frac{x - x_{i-1/2}}{h_i} & x_{i-1/2} \leq x \leq x_{i+1/2} \\ 0 & \text{elsewhere} \end{cases}, \quad (3.2)$$

corresponding to the node $x_{i+1/2}$. With these definitions, a local linear approximation to a function f can be formulated as $f(x) \simeq f_{L,i}b_{L,i}(x) + f_{R,i}b_{R,i}(x)$, $x \in [x_{i-1/2}, x_{i+1/2}]$.¹

The spatial moments are defined by integrals over the each element, using the two basis functions. We use $\langle \cdot \rangle$ to indicate weighted integration over a spatial element. The spatial moments are

$$\langle \cdot \rangle_{L,i} = \frac{2}{h_i} \int_{x_{i-1/2}}^{x_{i+1/2}} b_{L,i}(x)(\cdot)dx \quad (3.3)$$

and

$$\langle \cdot \rangle_{R,i} = \frac{2}{h_i} \int_{x_{i-1/2}}^{x_{i+1/2}} b_{R,i}(x)(\cdot)dx, \quad (3.4)$$

where the factor of $2/h_i$ is a normalization constant. In this notation $\langle \phi \rangle_{L,i}$ and $\langle \phi \rangle_{R,i}$ represent spatial moments of the intensity over cell i , opposed to $\phi_{L,i}$ and $\phi_{R,i}$, which represent the interior value of the linear representation of $\phi(x)$ at $x_{i-1/2}$ and $x_{i+1/2}$ within the cell.

To simplify notation and discussion, we also define the slope and average moments over a spatial cell. The element-averaged scalar intensity is

$$\phi_i = \frac{1}{h_i} \int_{x_{i-1/2}}^{x_{i+1/2}} \phi(x)dx \quad (3.5)$$

¹In literature the linear FE basis functions are formally defined with support over two adjacent elements. However, in our notation our functions only have non-zero support in element i . This accommodates our later definition of moments and discontinuous unknowns.

and

$$\phi_{x,i} = \frac{6}{h_i} \int_{x_{i-1/2}}^{x_{i+1/2}} \left(\frac{x - x_i}{h_i} \right) \phi(x) dx. \quad (3.6)$$

The linear representation over a cell can be written as $\phi(x) = \phi_i + 2\phi_{x,i}(x - x_i)/h_i^2$, for $x \in (x_{i-1/2}, x_{i+1/2})$.

3.1.2 Definition of Angular Moments

To reduce the angular dimensionality, positive and negative half-range integrals of the angular intensity are taken. The angular integrals are denoted with a superscript as

$$(\cdot)^\pm = \pm \int_0^{\pm 1} (\cdot) d\mu \quad (3.7)$$

The half-range integrals of I are defined as $\phi^+(x) = \int_0^1 I(x, \mu) d\mu$ and $\phi^-(x) = \int_{-1}^0 I(x, \mu) d\mu$, respectively. Thus, in terms of half-range quantities, the mean intensity is $\phi = \phi^- + \phi^+$. It is noted that in this notation the flux is defined as $J = J^- + J^+$, which is not the standard definition for the half-range fluxes, e.g., in [22].

3.1.3 Space-Angle Moments of the Radiation Transport Equation

The LO radiation equations are formed by applying the space and angle moment operators to the transport equation and performing algebraic manipulation. We provide a detailed derivation of the L and $+$ radiation moment equation and state the final results for the other moment operators. The independent variables are often suppressed for some, or all, of the dependent variables for compactness.

First, the L moment operator is applied to the time-discretized transport equation, i.e., Eq. (2.1); application of integration by parts to the streaming term yields

$$-\frac{2}{h_i} \mu_{i-1/2} I_{i-1/2}^{n+1} + \frac{2}{h_i^2} \int_{x_{i-1/2}}^{x_{i+1/2}} \mu I^{n+1}(x, \mu) dx + \left(\sigma_{t,i}^{n+1} + \frac{1}{c\Delta t} \right) \langle I^{n+1} \rangle_{L,i} - \frac{\sigma_{s,i}}{2} \langle \phi^{n+1} \rangle_{L,i}$$

$$= \frac{1}{2} \langle \sigma_{a,i}^{n+1} acT^{n+1,4} \rangle_{L,i} + \frac{1}{c\Delta t} \langle I^n \rangle_{L,i}. \quad (3.8)$$

Here, $I_{i+1/2}(\mu) \equiv I(x_{i+1/2}, \mu)$, and the cross sections have been assumed constant over a cell and evaluated with T^{n+1} . The mean intensity in the scattering term is expanded in terms of half-range unknowns. The integral can be rewritten in terms of L and R moments by noting that $b_{L,i}(x) + b_{R,i}(x) = 2/h_i$. These substitutions are made and the resulting equation is multiplied by h_i to produce

$$\begin{aligned} & -2\mu_{i-1/2} I_{i-1/2}^{n+1} + \langle \mu I^{n+1} \rangle_{L,i} + \langle \mu I^{n+1} \rangle_{R,i} + \left(\sigma_{t,i}^{n+1} + \frac{1}{c\Delta t} \right) h_i \langle I^{n+1} \rangle_{L,i} \\ & - \frac{\sigma_{s,i} h_i}{2} (\langle \phi \rangle_{L,i}^{n+1,+} + \langle \phi \rangle_{L,i}^{n+1,-}) = \frac{h_i}{2} \langle \sigma_a^{n+1} acT^{n+1,4} \rangle_{L,i} + \frac{h_i}{c\Delta t} \langle I^n \rangle_{L,i}. \end{aligned} \quad (3.9)$$

The resulting equation is integrated over the positive half range:

$$\begin{aligned} & -2 \left(\mu_{i-1/2} I_{i-1/2}^{n+1} \right)^+ + \langle \mu I^{n+1} \rangle_{L,i}^+ + \langle \mu I^{n+1} \rangle_{R,i}^+ + \left(\sigma_{t,i}^{n+1} + \frac{1}{c\Delta t} \right) h_i \langle \phi \rangle_{L,i}^{n+1,+} \\ & - \frac{\sigma_{s,i} h_i}{2} (\langle \phi \rangle_{L,i}^{n+1,+} + \langle \phi \rangle_{L,i}^{n+1,-}) = \frac{h_i}{2} \langle \sigma_a^{n+1} acT^{n+1,4} \rangle_{L,i} + \frac{h_i}{c\Delta t} \langle \phi \rangle_{L,i}^{n,+}. \end{aligned} \quad (3.10)$$

3.1.4 The Angular Consistency Terms

Now, algebraic manipulations are performed on the streaming terms to produce face and volume averages of μ , weighted by the intensity. Each term in the streaming term of Eq. (3.10) is multiplied by a factor of unity, with the desired unknown appropriate to each term in the numerator and denominator, as in [47]. Temporarily dropping the time index for clarity, the manipulations applied to the streaming term are as follows:

$$\left\langle \mu \frac{\partial I}{\partial x} \right\rangle_L^+ = -\frac{2}{h_i} (\mu I_{i-1/2})^+ + \frac{1}{h_i} [\langle \mu I \rangle_{L,i}^+ + \langle \mu I \rangle_{R,i}^+] \quad (3.11)$$

$$= -\frac{2}{h_i} (\mu I_{i-1/2})^+ \frac{(I_{i-1/2})^+}{(I_{i-1/2})^+} + \frac{1}{h_i} \left[\langle \mu I \rangle_{L,i}^+ \frac{\langle I \rangle_{L,i}^+}{\langle I \rangle_{L,i}^+} + \langle \mu I \rangle_{R,i}^+ \frac{\langle I \rangle_{R,i}^+}{\langle I \rangle_{R,i}^+} \right] \quad (3.12)$$

$$= -\frac{2}{h_i} \left\{ \frac{(\mu I)_{i-1/2}^+}{\phi_{i-1/2}^+} \right\} \phi_{i-1/2}^+ + \frac{1}{h_i} \left[\left\{ \frac{\langle \mu I \rangle_{L,i}^+}{\langle \phi \rangle_{L,i}^+} \right\} \langle \phi \rangle_{L,i}^+ + \left\{ \frac{\langle \mu I \rangle_{R,i}^+}{\langle \phi \rangle_{R,i}^+} \right\} \langle \phi \rangle_{R,i}^+ \right] \quad (3.13)$$

The ratios in braces are what we will formally define as *angular consistency terms*. These nonlinear functionals are approximated by the HO solver, similar to the approach in [47]. The angular consistency term for the L and $+$ moments is defined as

$$\{\mu\}_{L,i}^{n+1,+} \equiv \frac{\langle \mu I^{n+1} \rangle_{L,i}^+}{\langle I^{n+1} \rangle_{L,i}^+} = \frac{\frac{2}{h_i} \int_0^1 \int_{x_{i-1/2}}^{x_{i+1/2}} \mu b_{L,i}(x) I^{n+1}(x, \mu) dx d\mu}{\frac{2}{h_i} \int_0^1 \int_{x_{i-1/2}}^{x_{i+1/2}} b_{L,i}(x) I^{n+1}(x, \mu) dx d\mu}. \quad (3.14)$$

The consistency terms on the face represent averaging at a point, with a similar definition as

$$\mu_{i+1/2}^+ \equiv \frac{(\mu I_{i+1/2})^+}{\phi_{i+1/2}^+} = \frac{\int_0^1 \mu I(x_{i+1/2}, \mu) d\mu}{\int_0^1 I(x_{i+1/2}, \mu) d\mu}. \quad (3.15)$$

There are analogous definitions for the R and $-$ moments, e.g.,

$$\{\mu\}_{R,i}^{n+1,-} \equiv \frac{\langle \mu I^{n+1} \rangle_{R,i}^-}{\langle I^{n+1} \rangle_{R,i}^-} = \frac{\frac{2}{h_i} \int_{-1}^0 \int_{x_{i-1/2}}^{x_{i+1/2}} \mu b_{R,i}(x) I^{n+1}(x, \mu) dx d\mu}{\frac{2}{h_i} \int_{-1}^0 \int_{x_{i-1/2}}^{x_{i+1/2}} b_{R,i}(x) I^{n+1}(x, \mu) dx d\mu}. \quad (3.16)$$

Substitution of Eq. (3.24) and (3.24) simplifies moments of the streaming term for the L and $+$ operators:

$$\left\langle \mu \frac{\partial I}{\partial x} \right\rangle_L^+ = -\frac{2}{h_i} \mu_{i-1/2}^+ I_{i-1/2}^+ + \frac{1}{h_i} \left[\{\mu\}_{L,i}^+ \langle \phi \rangle_{L,i}^+ + \{\mu\}_{R,i}^+ \langle \phi \rangle_{R,i}^+ \right] \quad (3.17)$$

It is noted that this expression does not contain a cross section in the denominator, such as in the variable Eddington factor approach [10], eliminating issues in a void where $\sigma_t = 0$.

3.1.5 The Exact Radiation Moment Equations

A final form of the moment equation resulting from application of the L moment and positive half-range integral is obtained by substitution of Eq. (3.17) into Eq. (3.10):

$$\begin{aligned} -2\mu_{i-1/2}^{n+1,+} \phi_{i-1/2}^{n+1,+} + \{\mu\}_{L,i}^{n+1,+} \langle \phi \rangle_{L,i}^{n+1,+} + \{\mu\}_{R,i}^{n+1,+} \langle \phi \rangle_{R,i}^{n+1,+} + \left(\sigma_{t,i}^{n+1} + \frac{1}{c\Delta t} \right) h_i \langle \phi \rangle_{L,i}^{n+1,+} \\ - \frac{\sigma_{s,i} h_i}{2} (\langle \phi \rangle_{L,i}^{n+1,+} + \langle \phi \rangle_{L,i}^{n+1,-}) = \frac{h_i}{2} \langle \sigma_a^{n+1} acT^{n+1,4} \rangle_{L,i} + \frac{h_i}{c\Delta t} \langle \phi \rangle_{L,i}^{n,+}, \end{aligned} \quad (3.18)$$

The other radiation moment equations are derived analogously. Pairwise application of the L and R basis moments with the $+$ and $-$ half-range integrals to Eq. (2.1) ultimately yields four moment equations per cell. The equation for the R and $+$ moment is

$$\begin{aligned} 2\mu_{i+1/2}^{n+1,+} \phi_{i+1/2}^{n+1,+} - \{\mu\}_{L,i}^{n+1,+} \langle \phi \rangle_{L,i}^{n+1,+} - \{\mu\}_{R,i}^{n+1,+} \langle \phi \rangle_{R,i}^{n+1,+} + \left(\sigma_{t,i}^{n+1} + \frac{1}{c\Delta t} \right) h_i \langle \phi \rangle_{R,i}^{n+1,+} \\ - \frac{\sigma_{s,i} h_i}{2} (\langle \phi \rangle_{R,i}^{n+1,+} + \langle \phi \rangle_{R,i}^{n+1,-}) = \frac{h_i}{2} \langle \sigma_a^{n+1} acT^{n+1,4} \rangle_{R,i} + \frac{h_i}{c\Delta t} \langle \phi \rangle_{R,i}^{n,+}, \end{aligned} \quad (3.19)$$

The equations for the negative half-range moment are identical to the above with the negative half-range integrals replacing the positive where applicable. Explicitly,

$$\begin{aligned}
& -2\mu_{i-1/2}^{n+1,-} \phi_{i-1/2}^{n+1,-} + \{\mu\}_{L,i}^{n+1,-} \langle \phi \rangle_{L,i}^{n+1,-} + \{\mu\}_{R,i}^{n+1,-} \langle \phi \rangle_{R,i}^{n+1,-} + \left(\sigma_{t,i}^{n+1} + \frac{1}{c\Delta t} \right) h_i \langle \phi \rangle_{L,i}^{n+1,-} \\
& - \frac{\sigma_{s,i} h_i}{2} (\langle \phi \rangle_{L,i}^{n+1,+} + \langle \phi \rangle_{L,i}^{n+1,-}) = \frac{h_i}{2} \langle \sigma_a^{n+1} ac T^{n+1,4} \rangle_{L,i} + \frac{h_i}{c\Delta t} \langle \phi \rangle_{L,i}^{n,-} \quad (3.20)
\end{aligned}$$

and

$$\begin{aligned}
& 2\mu_{i+1/2}^{n+1,-} \phi_{i+1/2}^{n+1,-} - \{\mu\}_{L,i}^{n+1,-} \langle \phi \rangle_{L,i}^{n+1,-} - \{\mu\}_{R,i}^{n+1,-} \langle \phi \rangle_{R,i}^{n+1,-} + \left(\sigma_{t,i}^{n+1} + \frac{1}{c\Delta t} \right) h_i \langle \phi \rangle_{R,i}^{n+1,-} \\
& - \frac{\sigma_{s,i} h_i}{2} (\langle \phi \rangle_{R,i}^{n+1,+} + \langle \phi \rangle_{R,i}^{n+1,-}) = \frac{h_i}{2} \langle \sigma_a^{n+1} ac T^{n+1,4} \rangle_{R,i} + \frac{h_i}{c\Delta t} \langle \phi \rangle_{R,i}^{n,-}, \quad (3.21)
\end{aligned}$$

Ultimately, the two half-ranges will be treated differently when the equations are closed spatially.

3.1.6 Material Energy Equations

To derive the LO material energy equations, an approximation must be introduced to relate $T(x)$ and $T^4(x)$ within a cell. We represent $T(x)$ spatially with a LDFE trial space, i.e., $T(x) \simeq T_{L,i} b_{L,i}(x) + T_{R,i} b_{R,i}(x)$, $x \in (x_{i-1/2}, x_{i+1/2})$. This trial space will ensure preservation of the equilibrium diffusion limit and limit artificial propagation of energy across the system [24]. Similarly, the emission term is represented in the material and radiation equations with the LDFE interpolant $T^4(x) \simeq T_{L,i}^4 b_{L,i}(x) + T_{R,i}^4 b_{R,i}(x)$. The L and R spatial moments are taken of the material energy equations, and the LDFE representations for $T(x)$ and $\sigma_a ac T^4(x)$ are used to simplify the spatial integrals. The final LO material energy equation resulting from application of the L moment is

$$\begin{aligned}
\frac{\rho_i c_{v,i}}{\Delta t} \left[\left(\frac{2}{3} T_{L,i} + \frac{1}{3} T_{R,i} \right)^{n+1} - \left(\frac{2}{3} T_{L,i} + \frac{1}{3} T_{R,i} \right)^n \right] + \sigma_{a,i}^{n+1} (\langle \phi \rangle_{L,i}^+ + \langle \phi \rangle_{L,i}^-)^{n+1} \\
= \sigma_{a,i}^{n+1} ac \left(\frac{2}{3} T_{L,i}^4 + \frac{1}{3} T_{R,i}^4 \right)^{n+1}. \quad (3.22)
\end{aligned}$$

The equation for the R moment is

$$\begin{aligned}
\frac{\rho_i c_{v,i}}{\Delta t} \left[\left(\frac{1}{3} T_{L,i} + \frac{2}{3} T_{R,i} \right)^{n+1} - \left(\frac{1}{3} T_{L,i} + \frac{2}{3} T_{R,i} \right)^n \right] + \sigma_{a,i}^{n+1} (\langle \phi \rangle_{R,i}^+ + \langle \phi \rangle_{R,i}^-)^{n+1} \\
= \sigma_{a,i}^{n+1} ac \left(\frac{1}{3} T_{L,i}^4 + \frac{2}{3} T_{R,i}^4 \right)^{n+1}. \quad (3.23)
\end{aligned}$$

Cross sections have been assumed constant over each element, evaluated at the average temperature within the element, i.e., $\sigma_{a,i}^{n+1} = \sigma_{a,i}([T_{L,i}^{n+1} + T_{R,i}^{n+1}]/2)$. Because the material energy balance equation only contains angularly integrated quantities, there is no need to take angular moments of the above equations.

3.2 Closing the LO Equations in Space and Angle

At this point, the LO equations have too many unknowns: the relation between the volume and face averaged quantities and the angular consistency parameters are not known a priori. The HO solution is used to eliminate the consistency parameters and other approximations are used to eliminate the extra spatial unknowns from the equations. The six degrees of freedom (DOF) over each cell i are the four moments $\langle \phi \rangle_{L,i}^+$, $\langle \phi \rangle_{R,i}^+$, $\langle \phi \rangle_{L,i}^-$, and $\langle \phi \rangle_{R,i}^-$ and the two spatial edge values $T_{L,i}$ and $T_{R,i}$. After closure, the four radiation and two material energy equations define a system of equations for the six DOF, coupled spatially through the streaming term.

Before introducing the additional closures, we emphasize that at this point the only spatial or angular approximations to the radiation moment equations are an LDFF representation for $T^4(x)$ and cell-averaged cross sections; these moment equa-

tions are exact with respect to the chosen time discretization and these approximations. The material energy equations, as well as the emission source, required an approximation of LDFE in space for $T(x)$ and $T^4(x)$. Some approximation is always necessary to relate T and T^4 .

3.2.1 Angular Closure

The angular consistency parameters (e.g., Eq. (3.24) and (3.15)) are not known a priori. A lagged estimate of I^{n+1} from the previous HO solve is used to estimate the angular consistency parameters. In the HOLO algorithm, the equations for LO unknowns at iteration $k + 1$ use consistency parameters computed using the latest HO solution $\tilde{I}^{n+1,k+1/2}$ as an approximation for $I^{n+1}(x, \mu)$, e.g.,

$$\{\mu\}_{L,i}^{n+1,+} \simeq \frac{\langle \mu \tilde{I}_{HO}^{n+1,k+1/2} \rangle_{L,i}^+}{\langle \tilde{I}_{HO}^{n+1,k+1/2} \rangle_{L,i}^+} = \frac{\frac{2}{h_i} \int_0^1 \int_{x_{i-1/2}}^{x_{i+1/2}} \mu b_{L,i}(x) \tilde{I}_{HO}^{n+1,k+1/2}(x, \mu) dx d\mu}{\frac{2}{h_i} \int_0^1 \int_{x_{i-1/2}}^{x_{i+1/2}} b_{L,i}(x) \tilde{I}_{HO}^{n+1,k+1/2}(x, \mu) dx d\mu}. \quad (3.24)$$

We evaluate these terms using quadrature based on the LDFE functional representation $\tilde{I}_{HO}(x, \mu)$ provided by the HO solution.

3.2.2 LDFE Spatial Closure

After approximating the angular consistency terms in the time-discretized LO moment equations, a equation relating the spatial moments and outflow face values is needed to eliminate the final auxiliary unknowns, i.e., a spatial closure. We will eliminate the face terms to produce equations exclusively the desired moment unknowns. Several closures were investigated. The simplest closure is a linear-discontinuous (LD) spatial closure with the usual upwinding approximation [26]. A closure based on the HO solution is discussed in Sec. 3.6. Because there are no derivatives of T in Eq. (2.2), there is no need to define T on the faces in Eq. (3.22) and Eq. (3.23); only

moments of ϕ appear in the material energy equations, thus they are fully defined at this point and require no additional spatial closure.

Now, the LDFE closure is applied to the radiation moment equations for the case of positive flow (i.e., Eq. (3.18) and (3.19)). The LD closure over for the i -th cell and positive μ is illustrated in Fig. 3.2. The face terms $\mu_{i-1/2}$ and $\phi_{i-1/2}$ are upwinded from the previous cell $i-1$ or from a boundary condition; the terms at $x_{i+1/2}$ are linearly extrapolated, computed using the L and R basis moments. The linear approximation $\phi^+(x) = b_{L,i}(x)\phi_{L,i}^+ + b_{R,i}(x)\phi_{R,i}^+$, for $x \in (x_{i-1/2}, x_{i+1/2}]$, is substituted into the definition for the moments (i.e., Eq. (3.3) and (3.4)) and solved for the LD edge value $\phi_{i,R}^+$; The resulting outflow relation for positive flow is $\phi_{i+1/2}^+ \equiv \phi_{i,R}^+ = 2\langle\phi\rangle_{R,i}^+ - \langle\phi\rangle_{L,i}^+$; the LD closure for the negative half range produces $\phi_{i-1/2}^- = 2\langle\phi\rangle_{L,i}^- - \langle\phi\rangle_{R,i}^+$. The L moment and positive half-range equation with the LD closure and upwinding is

$$\begin{aligned}
& -2\mu_{i-1/2}^{n+1,+} (2\langle\phi\rangle_{R,i-1}^{n+1,+} - \langle\phi\rangle_{L,i-1}^{n+1,+}) + \{\mu\}_{L,i}^{n+1,+} \langle\phi\rangle_{L,i}^{n+1,+} + \{\mu\}_{R,i}^{n+1,+} \langle\phi\rangle_{R,i}^{n+1,+} \\
& + \left(\sigma_{t,i}^{n+1} + \frac{1}{c\Delta t} \right) h_i \langle\phi\rangle_{L,i}^{n+1,+} - \frac{\sigma_{s,i} h_i}{2} (\langle\phi\rangle_{L,i}^{n+1,+} + \langle\phi\rangle_{L,i}^{n+1,-}) \\
& = \frac{h_i}{2} \langle\sigma_a^{n+1} acT^{n+1,4}\rangle_{L,i} + \frac{h_i}{c\Delta t} \langle\phi\rangle_{L,i}^{n,+}. \quad (3.25)
\end{aligned}$$

Similar equations can be derived for the other directions and moments, fully defining the radiation equations. The closed equations are equivalent in numerical complexity to an LDFE discretization of the S_2 equations [26, 22], but with different quadrature points on the face and interior.

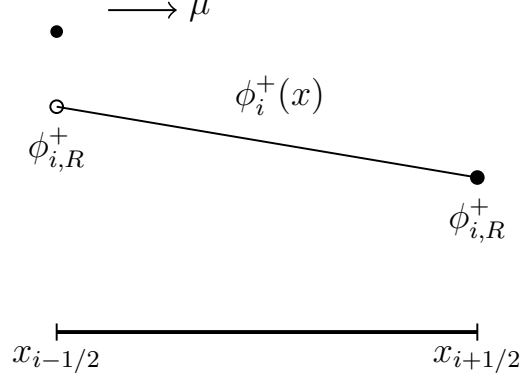


Figure 3.2: Linear discontinuous trial space for half-range mean intensity and $\mu > 0$, in LO equations.

Note that we have chosen to leave $\mu_{i-1/2}^{n+1,+}$ as a value to be estimated from the HO solver, which is more conducive to the HO spatial closures described in Sec. 3.6. Alternatively, the spatial closure could be introduced before performing the algebraic manipulation to form consistency terms (e.g., into Eq. (3.11)). This would produce only volume-weighted consistency terms in the equations.

3.2.3 Boundary Conditions

For all spatial closures, the specified incident angular intensity is incorporated into the upwinding term of the appropriate radiation moment equation. At the left boundary, the upwinded current is known, so for that L moment equation

$$\mu_{1/2}^+ \phi_{1/2}^+ = \int_0^1 \mu I^{inc,+}(\mu) d\mu, \quad (3.26)$$

where $I^{inc,+}(\mu)$ is the specified incident angular intensity at the left boundary. For all results in this work, only isotropic incident intensities were considered. A similar expression is derived for the right boundary. For S_2 -equivalent LO solves, i.e., all consistency terms are $\pm 1/\sqrt{3}$, the half-range flux in the above equation is renormal-

ized by multiplying the term in the moment equations by $2/\sqrt{3}$ to produce accurate solutions [27].

3.3 Newton's Method for LO Equations

Summation over all cells of the closed equations forms a global system of coupled equations. The equations are nonlinear due to the Planckian emission source. We have used a local Newton's method to solve the nonlinear system, based on a standard linearization of the Planckian source with cross sections evaluated at temperatures from the previous iteration, as described in [26]. A derivation of the LO Newton equations is given in A.2.

The equations for each half-range are coupled together via scattering. In one spatial dimension, the scattering terms can be included in the discrete system matrix and directly inverted. We consider an alternative iterative solution method that could be more easily extended to higher spatial dimensions in Sec. ???. For the direct solution method, isotropic scattering, including effective scattering terms from the linearization, are included in the system matrix. The system matrix is an asymmetric, banded matrix with a band width of seven and is inverted directly. Newton iterations are repeated until $\phi^{n+1}(x)$ and $T^{n+1}(x)$ are converged to a desired relative tolerance. Convergence in the Newton iterations is calculated using the spatial L_2 norm of the change in $\phi^{n+1}(x)$ and $T^{n+1}(x)$, relative to the norm of each solution.

In certain problems, the nonlinearities of the system can lead to divergence of the Newton iterations. This is often the result of taking relatively large time steps for problems with large values of σ_a and small values of ρc_v . To prevent divergence, a damped Newton method [17] can be used, at the cost of increased numbers of iterations. For a damped Newton's method, the estimated change in the solution between iterations is multiplied by a factor $\xi \in (0, 1)$, where ξ is referred to as the

damping factor. Sufficient reduction of the change in solutions between iterations will allow iterations to continue converging, by ensuring the solution remains within the domain of convergence. The details of modifying the Newton iterations in this work to include a damping factor are given in App. A.2.1. For simplicity, a fixed value of ξ was used for all iterations in problems where damping was found to be necessary.

3.4 Fix-ups for Negative Solutions with LDFE Closure

The linear-discontinuous (LD) closure with upwinding is not strictly positive. In particular, for optically thick cells with a steep intensity gradient, the linear representations for $\phi(x)$ and $T(x)$ can go below the floor temperature or negative. The floor temperature T_{\min} is defined as the initial temperature of the material and radiation in problems where boundary sources are applied at each of the boundaries. In such problems the radiation and material should continue to heat on the interior of the domain, and should physically not fall below the initial temperature. Negative values of intensity can propagate to adjacent cells. In thick regions of TRT problems, reasonably fine spatial cells can still be on the order of millions of mean free paths; negative values with an LD representation are unavoidable in practice for such cells and mesh refinement is of minimal use.

Typically, for a standard LDFE Galerkin spatial discretization, the equations are lumped to produce a discretization that is strongly resistant to negative values (for 1D) [26]. However, standard FE lumping procedures would introduce difficulties in computing the consistency terms from the HO solution. Alternatively, we have derived a modified spatial closure that produces unknowns equivalent to those from a lumped LD method in 1D. The L and R moments are defined the same as before, preserving the average within a cell, but the relation between the moments and the

outflow is modified. In the lumping-equivalent closure, the outflows are defined as

$$\phi_{i+1/2}^+ = \langle \phi \rangle_{i,R}^+ \quad (3.27)$$

$$\phi_{i-1/2}^- = \langle \phi \rangle_{i,L}^-. \quad (3.28)$$

The system is then fully defined with upwinding and the assumption of a linear relationship on interior of the element. This modified closure produces a linear representation that preserves zeroth moment, but the relation between the slope of the line and the first spatial moment has been modified. Because the basis functions $b_{R,i}(x)$ and $b_{L,i}(x)$ are strictly positive, the outflows tends to be positive. Strong sources and gradients can still lead to negativities at the edges of the LD representation. Details on the derivation of this relation are in Appendix A.1. The lumping closure was optionally applied in all cells or only in cells where negative intensities occur.

For simplicity, we also lump the emission source and temperature terms in the equations following the standard procedure [26]. For example, the lumped version of Eq. (3.22) is

$$\frac{\rho_i c_{v,i}}{\Delta t} (T_{L,i}^{n+1} - T_{L,i}^n) + \sigma_{a,i}^{n+1} (\langle \phi \rangle_{L,i}^+ + \langle \phi \rangle_{L,i}^-)^{n+1} = \sigma_{a,i}^{n+1} a c (T_{L,i}^{n+1})^4 \quad (3.29)$$

noting that no modification was made to the radiation moment term in this equation. It was found that lumping the temperature equations generally produced more robustness than exclusively modifying the spatial closure, but is not necessary for all problems.

We also investigated an alternative closure of the equations based on energy conservation and forcing the appropriate edge value to be the floor value. The

equations within cells that produce a negativity are modified to ensure the edge intensities are not below the floor temperature, and energy balance is conserved. This fixup is only applied in cells where a intensity has occurred during inversion of the LO streaming plus removal operator. For example, if $\phi_{R,i}^+$ is found to be negative, the modified equations (for the positive half range) in that cell are the balance equation, i.e.,

$$\begin{aligned}
& -\mu_{i-1/2}^{n+1,+} (2\langle\phi\rangle_{R,i-1}^{n+1,+} - \langle\phi\rangle_{L,i-1}^{n+1,+}) + \mu_{i+1/2}^{n+1,+} (2\langle\phi\rangle_{R,i}^{n+1,+} - \langle\phi\rangle_{L,i}^{n+1,+}) \\
& + \left(\sigma_{t,i}^{n+1} + \frac{1}{c\Delta t} \right) \frac{h_i}{2} (\langle\phi\rangle_{L,i}^{n+1,+} + \langle\phi\rangle_{R,i}^{n+1,+}) - \frac{\sigma_{s,i} h_i}{4} (\langle\phi\rangle_{L,i}^{n+1} + \langle\phi\rangle_{R,i}^{n+1}) \\
& = \frac{h_i}{4} \sigma_{a,i}^{n+1} ac (\langle T^{n+1,4} \rangle_{L,i} + \langle T^{n+1,4} \rangle_{R,i}) + \frac{h_i}{2c\Delta t} (\langle\phi\rangle_{L,i}^{n,+} + \langle\phi\rangle_{R,i}^{n,+}) \quad (3.30)
\end{aligned}$$

and the closure equation, i.e.,

$$2\langle\phi\rangle_{i,R}^+ - \langle\phi\rangle_{i,L}^+ = T_{\min}. \quad (3.31)$$

Because our solution method directly inverts the LO system, negative edge intensities must be detected, the fix-up applied locally to all elements and half-ranges where necessary, and then that Newton solve repeated. In practice, this flooring procedure was observed to produce positive answers, but was not as robust as performing lumping in all cells. In general, as the time step size is increased, this fixup led to the Newton solve diverging (i.e., damping is required to converge the iterations), more rapidly than if lumping was used for all cells. A similar effect was observed in some problems when attempting to only lump the equations in cells where negativities were observed and resolving that Newton step.

3.5 Accuracy in the Equilibrium Diffusion Limit

In our standard LO scheme, the LO equations use an LDFE representation for the temperature and the uhd preserve the equilibrium diffusion limit. In this limit, the MC HO solution will estimate angular consistency terms associated with an isotropic intensity, based on a spatially LD emission source. This produces equations that are equivalent to the S_2 equations, but with quadrature points defined by $\pm 1/2$. Because the spatial closure produces equations that are equivalent to an LDFE solution to the S_2 equations, we expect the equations to preserve the equilibrium diffusion limit, which is known to preserve the EDL based on discrete asymptotic analysis [26].

3.6 Spatial Closure based on the HO Solution

This section describes an alternative spatial closure to the LO equations based on a parametric relation from the HO solution. In addition to estimating the angular consistency terms, the HO intensity estimates a relation between volume and face-averaged intensities to eliminate the remaining unknowns from the equations. In the remainder of this section, we will motivate the HO spatial closure by manipulating a half-range balance equations to form a single unknown for each cell and half range. We will then discuss the forms of HO spatial closures investigated, based on modifications to standard spatial closures.

3.6.1 Motivation

A half-range balance equation for $\mu > 0$ is formed by adding the exact L and R radiation moment equations given by Eq. (3.18) and (3.19), i.e.,

$$\mu_{i+1/2}^+ \phi_{i+1/2}^+ - \mu_{i-1/2}^+ \phi_{i-1/2}^+ + \sigma_{a,i} h_i \phi_i^+ = \frac{h_i}{2} q_i, \quad (3.32)$$

where q_i represents the cell-averaged emission source. In the HOLO algorithm, after estimating the consistency terms $\mu_{i\pm 1/2}^+$ unwinding the inflow term $\phi_{i-1/2}^+$, an additional equation is needed to eliminate the outflow $\phi_{i+1/2}^+$ to produce an equation for a single unknown ϕ_i^+ . Standard spatial discretizations techniques use a fixed approximation for all cells to eliminate the outflow in terms of other unknowns. Alternatively, the HO solution can be used to estimate a parametric relation between the other unknowns and the outflow, i.e.,

$$\phi_{i+1/2}^+ = f(\gamma_i^{+,HO}, \phi_i^+, \phi_{x,i}^+, \phi_{i-1/2}^+), \quad (3.33)$$

where $\gamma_i^{HO,+}$ is a local constant to be estimated with the HO solution and f is some function of some number of the input variables. The ECMC solution can provide all of the unknowns in the above equation, so the value of γ_i^{HO} can be determined directly.

If the problem were linear, or the nonlinear problem was fully converged, then application of this closure can ensure that the HO and LO equations produce the same moments, preserving the HO accuracy. To produce the same moments, the HO solution must also satisfy the local balance equation, e.g., Eq. (3.32). Then the LO equations and HO equations must have the same moments to satisfy both Eq. (3.33) and Eq. (3.32), upon nonlinear convergence of the outer HOLO iterations. If any higher moments are introduced through the spatial closure, then the HO solution must also satisfy the corresponding balance equations that the LO equations do. For example, both the LO and HO equation must satisfy the first moment equation in space if the closure is a function of the first moment.

As TRT problems are non-linear (i.e., scattering or thermal emission are included in q), the moments will only be preserved upon non-linear convergence of the source. The nonlinearity introduces the possibility for stability issues, particularly with MC noise. However, we have already consistently formed angular consistency terms, so the the spatial closure should be more stable than introducing other terms, such as in NDA methods [41, 40].

3.6.2 Choice of Spatial Closure

We will explore two different closure relations based on modifications to the standard LD closure: a scaled slope, i.e.,

$$\phi_{i\pm 1/2}^{\pm} = \phi_i^+ \pm \gamma_i^{\pm} \phi_{x,i}^+ \quad (3.34)$$

and a scaled average

$$\phi_{i\pm 1/2}^{\pm} = \gamma_i^{\pm} \phi_i^{\pm} \pm \phi_{x,i}^{\pm}, \quad (3.35)$$

where a value of $\gamma_i = 1$ produces the standard linear discontinuous expressions for the extrapolated outflows. Our LO system is formulated in terms of L and R moments, rather than the average and slope. Thus, Eq. (3.34) and (3.35) are expressed in terms of the L and R unknowns, using the relations given in App. A.1. In terms of these moments, the scaled-slope closure is

$$\phi_{i+1/2}^+ = \left(\frac{1 - 3\gamma_i^+}{2} \right) \langle \phi \rangle_{L,i}^+ + \left(\frac{1 + 3\gamma_i^+}{2} \right) \langle \phi \rangle_{R,i}^+ \quad (3.36)$$

$$\phi_{i-1/2}^- = \left(\frac{1 + 3\gamma_i^-}{2} \right) \langle \phi \rangle_{L,i}^- + \left(\frac{1 - 3\gamma_i^-}{2} \right) \langle \phi \rangle_{R,i}^- \quad (3.37)$$

and the scaled-average relation is

$$\phi_{i+1/2}^+ = \left(\frac{\gamma_i^+ - 3}{2} \right) \langle \phi \rangle_{L,i}^+ + \left(\frac{\gamma_i^+ + 3}{2} \right) \langle \phi \rangle_{R,i}^+ \quad (3.38)$$

$$\phi_{i-1/2}^- = \left(\frac{\gamma_i^- + 3}{2} \right) \langle \phi \rangle_{L,i}^- + \left(\frac{\gamma_i^- - 3}{2} \right) \langle \phi \rangle_{R,i}^-. \quad (3.39)$$

REWRITE: It is tempting to use a closure that is only a function of the average. This Although this can produce accuracy in smooth problems, it leads to a problem where the slope of the source is accounted for almost entirely in the slope of the radiation and the outflow is not forced to do anything intelligent. If you had scattering, this would become very inaccurate. This can be seen by looking at marshak wave and the slope equation, as you come to equilibrium it causes problems.

The HO solution is used to estimate γ_i . The MC solution must be modified to tally the MC estimated intensity on faces. For example, for $\mu > 0$, the LO equations

for moments at $k + 1$ use closure parameters evaluated at $k + 1/2$ as

$$\gamma_i^{+,HO,k+1/2} = \frac{\phi_{i+1/2}^{+,HO,k+1/2} - \phi_i^{+,HO,k+1/2}}{\phi_{x,i}^{+,HO,k+1/2}}, \quad (3.40)$$

for the scaled-slope closure. For this closure, as the slope goes to zero this expression becomes undefined. In cells where the slope is $O(10^{-13}\psi_i)$, we use $\gamma_i = 1$. For the problems tested, no issues have occurred with this closure, even γ can become very large for common, small values of $|\psi^x/\psi_i|$. This is because in such regions the solution is changing minimally anyways. The main benefit of the scaled-slope closure is it allows for values of γ that are equivalent to other closures, as discussed in App. A.1: $\gamma_i = 0$ produces a step closure [21], which has a zero slope over the cell, and $\gamma_i = 1/3$ produces a lumping-equivalent closure.

3.6.3 The Doubly-Discontinuous Trial Space

Because of the temperature unknowns and the HO scattering source representation, a representation on the interior of the cell for the temperature and intensity is needed. Thus, we introduce a linear doubly discontinuous (LDD) trial space for the half-range intensities, which is depicted in Fig. 3.3. The linear relation on the interior of the cell preserves the L and R moments of the solution, and the outflow from the cell is some parametric (i.e., non linear) extrapolation of those moments. The temperature is still represented with a linear interpolant of T^4 and T . This trial space has an extra unknown in the radiation equations for each cell and direction, which is eliminated from the system with the HO spatial closure. The ECMC algorithm is modified to also include a LDD trial space which allows for estimate of the solution at faces, as discussed later in Sec 4.5.

To solve the LO equations, Eq. (3.36) or (3.38) is substituted locally for the

appropriate outflow face term in each LO moment equation. There is a spatial closure parameter for each half-range, for each cell. The γ_i^\pm are estimated from the previous HO solution. For the initial LO solve within each time step, the outflow is assumed continuous, using the standard upwinding and LD closure. As an example, the positive half-range and L moment equation (i.e., Eq. (3.18)), for the scaled-slope closure, becomes

$$\begin{aligned}
& -2\mu_{i-1/2}^{n+1,+} \left[\left(\frac{1-3\gamma_{i-1}^{HO,+}}{2} \right) \langle \phi \rangle_{L,i-1}^+ + \left(\frac{1+3\gamma_{i-1}^{HO,+}}{2} \right) \langle \phi \rangle_{R,i-1}^+ \right] \\
& \quad + \{\mu\}_{L,i}^{n+1,+} \langle \phi \rangle_{L,i}^{n+1,+} + \{\mu\}_{R,i}^{n+1,+} \langle \phi \rangle_{R,i}^{n+1,+} \\
& \quad + \left(\sigma_{t,i}^{n+1} + \frac{1}{c\Delta t} \right) h_i \langle \phi \rangle_{L,i}^{n+1,+} - \frac{\sigma_{s,i} h_i}{2} (\langle \phi \rangle_{L,i}^{n+1,+} + \langle \phi \rangle_{L,i}^{n+1,-}) \\
& \quad = \frac{h_i}{2} \langle \sigma_a^{n+1} acT^{n+1,4} \rangle_{L,i} + \frac{h_i}{c\Delta t} \langle \phi \rangle_{L,i}^{n,+}, \quad (3.41)
\end{aligned}$$

and the R moment equation becomes

$$\begin{aligned}
& 2\mu_{i+1/2}^{n+1,+} \left[\left(\frac{1-3\gamma_i^{HO,+}}{2} \right) \langle \phi \rangle_{L,i}^+ + \left(\frac{1+3\gamma_i^{HO,+}}{2} \right) \langle \phi \rangle_{R,i}^+ \right] \\
& \quad - \{\mu\}_{L,i}^{n+1,+} \langle \phi \rangle_{L,i}^{n+1,+} - \{\mu\}_{R,i}^{n+1,+} \langle \phi \rangle_{R,i}^{n+1,+} + \left(\sigma_{t,i}^{n+1} + \frac{1}{c\Delta t} \right) h_i \langle \phi \rangle_{R,i}^{n+1,+} \\
& \quad - \frac{\sigma_{s,i} h_i}{2} (\langle \phi \rangle_{R,i}^{n+1,+} + \langle \phi \rangle_{R,i}^{n+1,-}) = \frac{h_i}{2} \langle \sigma_a^{n+1} acT^{n+1,4} \rangle_{R,i} + \frac{h_i}{c\Delta t} \langle \phi \rangle_{R,i}^{n,+}. \quad (3.42)
\end{aligned}$$

These equations contain only the original desired radiation moment and LD temperature unknowns. During the Newton solve, once new half-range intensities are determined, the temperatures are updated using the same material energy equations as for the LD closure, i.e., Eq. (3.22) and Eq. (3.23).

Because the outflow from one cell is upwinded into the next cell, energy conservation by the LO equations is preserved. The closed equations have the same numerical

complexity as the LDFE LO equations, but with an increased storage on the coarse mesh for the $\{\gamma_i\}$. Also, the linear representation for the interior solutions and emission source should approach the LD closure in the equilibrium diffusion limit, as long as the HO spatial closure is estimated with sufficient statistical accuracy.

3.6.4 *Fixup for the Linear Doubly-Discontinuous Trial Space*

REWRITE: Combine next two paragraphs The doubly discontinuous trial space presents an additional difficulty in that the outflow is now unhinged from the linear relationship. For this case, we use the lumped representation on the interior of the solution for all cells. The outflow can still be driven negative due to non-linearities, which leads to negative values in down-stream cells. This is a result of the HO estimation of the spatial closure using and the moments was based on lagged source terms. When negativities occur, we force the outflow to be continuous, using the lumping-equivalent LD closure in those cells. That Newton iteration must then be repeated.

In the case of strong gradients, the interior representation could be driven negative. In such cases, we can use the lumping-equivalent relation from App. A.1 to define the linear representation. For example, the lumped emission source is

$$T = \langle T \rangle_{L,i}^4 b_{L,i}(x) + \langle T \rangle_{R,i}^4 b_{R,i}(x), \quad x \in (x_{i-1/2}, x_{i+1/2}) \quad (3.43)$$

There are analogous relations for $T(x)$ and $\phi^\pm(x)$ over each cell. These expressions are positive as long as the moments are positive, which is true for physical solutions. If the lagged, MC spatial closure produces an outflow from a cell that is negative, then these moments could become negative. In such cases, we force that cell to use a standard lumped relation for the moment equations, with no discontinuity at the outflow, and restart that Newton solve. It is important to note that the spatial

closure will still have the same relation between the moments and the outflow; the lumping relation only affects the linear representation that the moments correspond to. For example in Eq. (3.22), the lumped representation changes $2/3T_{L,i} + 1/3T_{R,i}$ to $T_{L,i}$, but no modification are made to the absorption term $\sigma_{a,i}\langle\phi\rangle_{L,i}$.

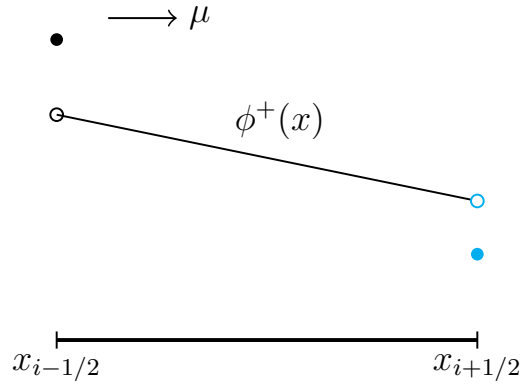


Figure 3.3: Linear doubly-discontinuous representation for mean intensity in LO equations.

3.6.5 Issues with ECMC for Spatial Closure

There are several issues with ECMC that cause the LO moments to not exactly preserve the HO moments, even for a linear problem. With ECMC, global and, particularly, local energy balance are generally not preserved. For standard MC, there are source biasing techniques (e.g., systematic sampling) that exactly preserve the local zeroth moment of the source and thus satisfy the local balance equations [31, 43]). However, for our HOLO method, even with standard MC we have to reconstruct the bilinear moment of x and μ , so the consistency terms lead to LO equations that do not exactly preserve the first moment of the HO solution². One final reason is

²It was verified that with standard MC, systematic sampling, no analog sampling, and a closure that is only a function of the zeroth moment, the LO solution exactly reproduces the HO moments,

that the analog treatment of absorption for particles below the weight cutoff (e.g., see Sec. 4.4) results in $\sigma_a \phi_i^{HO}$ and the amount of energy removed from a cell during MC transport to not be equal; this is due to statistical noise in the path-length estimators for ϕ_i^{HO} . However, ECMC will preserve balance to the order of the iterative error and statistical noise, so the closure parameters will reproduce the HO moments to the accuracy of the LO solution.

for a linear problem

4. THE EXPONENTIALLY-CONVERGENT MONTE CARLO HIGH-ORDER SOLVER

The time-discretized transport equation to be solved by the HO solver is

$$\mu \frac{\partial I^{n+1,k+1/2}}{\partial x} + \left(\sigma_t^k + \frac{1}{c\Delta t} \right) I^{n+1,k+1/2} = \frac{\sigma_s}{2} \phi^{n+1,k} + \frac{1}{2} (\sigma_a^k acT^4)^{n+1,k} + \frac{\tilde{I}^n}{c\Delta t} \quad (4.1)$$

where the superscript k represents the outer HOLO iteration index. Here, $k + 1/2$ denotes the HO solve within outer HOLO iteration k , whereas k and $k + 1$ represent successive LO solves. The sources at k in Eq. (4.1) are estimated by the previous LO solution. Temperature-dependent cross sections are evaluated at $T^{n+1,k}$. As all sources on the right side of the equation are known, this defines a fixed-source, pure absorber transport problem. The above transport equation has the same form as a steady-state neutronics problem. We will solve this transport problem using the ECMC method.

In the remainder of this chapter, an overview of the ECMC solution method applied in this work is given. First, the LDFE trial space used by the ECMC algorithm is detailed. Then, the ECMC algorithm is developed, followed by more specific sampling and tracking details.

4.1 Implementation of LDFE x - μ Trial Space

To form the algorithm, a trial-space representation for the intensity is necessary. The ECMC solver uses a finite element representation in space and angle. On the interior of the cell with the i -th spatial index and j -th angular index, the linear

representation is defined as

$$\tilde{I}(x, \mu) = I_{a,ij} + \frac{2}{h_i} I_{x,ij} (x - x_i) + \frac{2}{h_j} I_{\mu,ij} (\mu - \mu_j), \quad (x, \mu) \in \mathcal{D}_{ij}, \quad (4.2)$$

where $\mathcal{D}_{ij} : x_{i-1/2} \leq x \leq x_{i+1/2} \times \mu_{j-1/2} \leq \mu \leq \mu_{j+1/2}$ is a rectangular cell in space and angle. The spatial cell width is h_i , the angular width is h_j , the center of the cell is (x_i, μ_j) , and

$$I_{a,ij} = \frac{1}{h_i h_j} \iint_{\mathcal{D}_{ij}} I(x, \mu) dx d\mu \quad (4.3)$$

$$I_{x,ij} = \frac{6}{h_i h_j} \iint_{\mathcal{D}_{ij}} \left(\frac{x - x_i}{h_i} \right) I(x, \mu) dx d\mu \quad (4.4)$$

$$I_{\mu,ij} = \frac{6}{h_i h_j} \iint_{\mathcal{D}_{ij}} \left(\frac{\mu - \mu_j}{h_j} \right) I(x, \mu) dx d\mu, \quad (4.5)$$

where I_a is the cell-averaged intensity, and I_μ and I_x define the first moment in μ and x of the intensity, respectively. The streaming term requires definition of $I(x, \mu)$ on faces. Standard upwinding in space is used to define $I(\mu)$ on incoming faces, e.g., for an unrefined mesh,

$$\tilde{I}_{ij}(x_{i-1/2}, \mu) = \begin{cases} I_{a,i-1,j} + I_{x,i-1,j} + \frac{2}{h_j} I_{\mu,i-1,j} (\mu - \mu_j) & 0 \leq \mu_{j-1/2} \leq \mu \leq \mu_{j+1/2} \\ I_{a,ij} - I_{x,ij} + \frac{2}{h_j} I_{\mu,ij} (\mu - \mu_j) & \mu_{j-1/2} \leq \mu \leq \mu_{j+1/2} \leq 0 \end{cases} \quad (4.6)$$

and

$$\tilde{I}_{ij}(x_{i+1/2}, \mu) = \begin{cases} I_{a,ij} + I_{x,ij} + \frac{2}{h_j} I_{\mu,ij} (\mu - \mu_j) & 0 \leq \mu_{j-1/2} \leq \mu \leq \mu_{j+1/2} \\ I_{a,i+1,j} - I_{x,i+1,j} + \frac{2}{h_j} I_{\mu,i+1,j} (\mu - \mu_j) & \mu_{j-1/2} \leq \mu \leq \mu_{j+1/2} \leq 0 \end{cases}, \quad (4.7)$$

for all i and j on the interior of the domain. For all simulations in this work, boundary conditions are provided as a specified isotropic intensity. Thus, the value of $I_{1j}(x_1/2, \mu)$ is a constant, for all j .

4.2 The ECMC Algorithm

The ECMC method is an iterative residual MC method. In operator notation, Eq. (4.1) can be written as

$$\mathbf{L}^k I^{n+1,k+1/2} = q^k \quad (4.8)$$

where $I^{n+1,k+1/2}$ is the transport solution of the angular intensity based on the k -th LO estimate of q^k . The linear operator \mathbf{L}^k is the *continuous* streaming plus removal operator, given by the left-hand side of Eq. (4.1), i.e.,

$$\mathbf{L}^k(\cdot) = \left[\mu \frac{\partial}{\partial x} + \left(\sigma_t^k + \frac{1}{c\Delta t} \right) \right] (\cdot) \quad (4.9)$$

We will use superscript (m) to indicated the m -th inner HO iteration. The LDFE representation of the m -th approximate solution to Eq. (4.8) is denoted $\tilde{I}^{n+1,(m)}(x, \mu)$. The associated residual is defined as $r^{(m)} = q - \mathbf{L}^k \tilde{I}^{n+1,(m)}$. Explicitly, the residual at iteration m is

$$\begin{aligned} r^{(m),k+1/2} = & \frac{\sigma_s}{2} \phi^{n+1,k} + \frac{1}{2} (\sigma_a a c T^4)^{n+1,k} + \frac{\tilde{I}^n}{c\Delta t} \\ & - \left(\mu \frac{\partial \tilde{I}^{n+1,k+1/2}}{\partial x} + \left(\sigma_t^k + \frac{1}{c\Delta t} \right) \tilde{I}^{n+1,k+1/2} \right)^{(m)} \end{aligned} \quad (4.10)$$

where the k terms have a LDFE representation in space on the coarsest mesh and are not recalculated at any point during the HO solve. The LDFE functional form of \tilde{I}^n is defined from the final HO solution of the previous time step. The HOLO iteration indices are suppressed for the remainder of this chapter because the LO-estimated

q^k and \mathbf{L}^k remain constant for the entire HO solve.

Addition of $\mathbf{L}I^{n+1} - q = 0$ to the Eq. (4.10), i.e., the residual equation, and manipulation of the result yields the error equation

$$\mathbf{L}(I^{n+1} - \tilde{I}^{n+1,(m)}) = \mathbf{L}\epsilon^{(m)} = r^{(m)} \quad (4.11)$$

where I^{n+1} is the exact solution¹ to the problem defined by Eq. (4.1) and $\epsilon^{(m)}$ is the true error in the approximate solution $\tilde{I}^{n+1,(m)}$. In the above equation, the incoming error is treated with a vacuum boundary condition. The residual source incorporates the incident intensity at boundaries through the face source. The \mathbf{L} operator in the above equation is inverted with the MC method, which statistically estimates an LDFE projection of the error in $\tilde{I}^{n+1,(m)}$, i.e.,

$$\tilde{\epsilon}^{(m)} = \mathbf{L}^{-1}r^{(m)} \quad (4.12)$$

where \mathbf{L}^{-1} is the Monte Carlo inversion of the streaming and removal operator. This inversion is strictly a standard Monte Carlo simulation; particle histories are tracked and the mean behavior estimated as in standard solutions to a Boltzmann transport equation [31, 35], although the source is complicated and produces both positive and negative statistical weights; sampling of the source is detailed in Sec. 4.3. It is noted that the exact error in $\tilde{I}^{n+1,(m)}$ (with respect to Eq. (4.1)) is being estimated with MC; tallies produce an integral projection of the error onto a LDFE space-angle trial space. Volumetric flux tallies over each space-angle element are required to estimate $\tilde{\epsilon}^{(m)}$, as detailed in Sec. 4.4. The space-angle moments of the error, preserved with the representation $\tilde{\epsilon}^{(m)}$, can be added to the moments of $\tilde{I}^{n+1,(m)}$ to produce a more

¹For clarity, in this chapter the exact solution is the exact solution to the transport problem defined by Eq. (4.1), not to the continuous equations that are trying to be solved.

accurate solution.

The ECMC algorithm iterates on this process as follows:

1. Initialize the guess for $\tilde{I}^{n+1,(0)}$ to \tilde{I}^n or the projection of \tilde{I}^{n+1} from the latest HO solve
2. Compute $r^{(m)}$.
3. Perform a MC simulation to obtain $\tilde{\epsilon}^{(m)} = \mathbf{L}^{-1}r^{(m)}$
4. Compute a new estimate of the intensity $\tilde{I}^{n+1,(m+1)} = \tilde{I}^{n+1,(m)} + \tilde{\epsilon}^{(m)}$
5. Repeat steps 2 – 4 until desired convergence criteria is achieved.

Exponential convergence is obtained if the error ϵ is reduced each batch. With each batch, a better estimate of the solution is being used to compute the new residual, decreasing the magnitude of the MC residual source at each iteration m , relative to the solution I^{n+1} . The initial guess for the angular intensity $I^{n+1,(0)}$ is computed based on the previous solution for \tilde{I}^n . This is a critical step in the algorithm; it significantly reduces the required number of particles per time step because the intensity does not change drastically between time steps in optically-thick regions.

4.2.1 Projection and Statistical Accuracy of ECMC

Here, we emphasize the solution $\tilde{I}^{n+1,(m)}$ represents the LDFE projection of the exact Monte Carlo solution to the transport problem defined by Eq. (4.1). The discretization error is in q , i.e., the LD spatial representation of the emission and scattering source and the LDFE space-angle projection $\tilde{I}^n(x, \mu)$. The projection of the intensity is in general far more accurate than a standard finite element solution, e.g., a S_N collocation method in angle. In typical IMC calculations, the average energy deposition within a cell is a projection that is computed with a standard

path-length volumetric flux tally; the zeroth moment of the LDFE projection of ϵ is computed using an equivalent tally, preserving the zeroth moment of the true error.

To see why the true error is being estimated, it is important to note that \mathbf{L} in Eq. (4.11) is the continuous operator. The MC inverse \mathbf{L}^{-1} is a statistical solution method for an integral equation. The solution to this integral equation can be shown to provide the analytic inverse of the operator \mathbf{L} [31, 32]. Applying L^{-1} to Eq (4.11) and adding the result to the previous solution yields the desired moments of the exact solution:

$$\tilde{I}^{n+1,(m+1)} = \tilde{I}^{n+1,(m)} + \tilde{\epsilon}^{(m)} \quad (4.13)$$

$$\simeq \tilde{I}^{n+1,(m)} + \mathbf{L}^{-1} \left(q - \mathbf{L} \tilde{I}^{n+1,(m)} \right) \quad (4.14)$$

$$\simeq \mathbf{L}^{-1} q \quad (4.15)$$

where the above expression is equal in the limit of an infinite number of histories, within a single batch.

A MC batch provide a standard MC transport estimate of moments of the error. Each batch estimate of the moments of ϵ has a statistical uncertainty that, with sufficient sampling, is governed by the standard $1/\sqrt{N}$ convergence rate [31], for a particular source $r^{(m)}$, where N is the number of histories performed. If the statistical estimate of the projection $\tilde{\epsilon}$ is not sufficiently accurate, then the iterations would diverge. It is noted that there is statistical correlation across batches because $I^{n+1,(m+1)}$ and $\epsilon^{(m)}$ are correlated through $I^{n+1,(m)}$ and the MC source $r^{(m)}$. A general proof of exponential convergence for related adaptive MC transport methods is depicted in [18].

Because the intensity is saved between time steps, there is correlation that can not be easily measured. However, within a batch, the statistical uncertainty in

moments of $\epsilon^{(m)}$ can be estimated with the sample variance of histories, using the standard sample-variance of MC mean estimators [31]. This provides a statistical estimate of moments of the solution estimated in that batch that asymptotically obey the central limit theorem [31], conditioned on the previous solution $I^{n+1,(m)}$. However, care must be taken with these statistical estimates, as they do not have the usual MC interpretation of confidence intervals because of correlations. Explicitly, if a particular simulation is repeated with independent sets of random numbers, the sample means will not (on average) correctly reproduce the confidence interval that the sample variance from the original simulation estimated. Additionally, the number of histories within each batch are likely too low for the central limit theorem to truly apply, as they do not sample the full solution space sufficiently [35].

4.2.2 Adaptive Mesh Refinement

Because the exact angular intensity does not in general lie within the LDFFE trial space, the iterative estimate of the error will eventually stagnate once the error cannot be sufficiently represented by a given FE mesh. An adaptive h -refinement algorithm has been implemented that can be used to allow the system to continue converging towards the exact solution [29, 3]. For TRT problems where absorption-reemission physics dominate, the diffusive and slowly varying regions of the problem require a less refined angular mesh to capture the solution than typical neutronics problems. However, greater spatial resolution is needed due to steep spatial gradients. Once error stagnation has occurred (and mesh refinement has reached a maximum level), additional histories can be performed with a fixed residual source to estimate the remaining error in the current solution. Although the remaining error will converge statistically at a standard $1/\sqrt{N}$ convergence rate, the remaining error will be much smaller than for a standard MC simulation, producing a much more efficient solution

method overall.

Detailed equations for performing projections between meshes and computing the residual source on the refined meshes can be found in [29]. At the end of the ECMC batch, refinement is performed in space-angle cells based on a jump indicator. The jump indicator is the magnitude of the different between $I(x, \mu)$ in adjacent cells, averaged over each edge. The value of the largest jump, out of the four edges within a cell, is used as the indicator for that cell; alternatively, the error could directly be used as an indicator. Based on this indicator, a preset fraction of cells are refined based on the indicator. The refinement of a cell is chosen to be symmetric, with each space-angle cell divided into four equal-sized cells and only one refinement level difference between adjacent cells is allowed, except for cells that share an edge across $\mu = 0$. The solution for $\tilde{I}^{n+1}(x, \mu)$ of the batch is projected onto the finer mesh for the next batch. Because the dimensionality of the sample space has increased, we increase the number of histories per batch such that the ratio of the number of histories to total cells is approximately constant for all meshes. At the end of the last HO solve in a time step, \tilde{I}^{n+1} is projected back onto the original, coarsest mesh and stored as \tilde{I}^n for the next time step.

4.2.3 *Negative Values for the Radiation Intensity*

For the HO solver, in cells with a steep gradient, the LDFE trial space can result in negative values of $\tilde{I}^{n+1}(x, \mu)$, similar to in the LO equations. In general, in such cells where the trial space cannot accurately represent the solution, error stagnation will rapidly occur. More sophisticated methods for resolving negative values are investigated in Chapter 7. However, because the residual formulation in ECMC allows for negative weight particles to occur, it is not strictly necessary to treat these cells specially during each MC batch. Instead, two simple fixups can be applied:

unphysical angular consistency terms can be modified, or the LDFE projection of the intensity can be modified to be strictly positive at the end of the MC batch. To modify angular consistency terms, we determine if consistency terms lie in the appropriate half space at the end of the HO solve, an indication that the intensity was negative within that spatial cell. If any terms are non-physical, then they are replaced with the corresponding S_2 -equivalent value, i.e., $\mu^\pm = \pm 1/\sqrt{3}$. For the second fixup, we scale the slopes of the solution to produce a positive representation, as detailed in Sec. 7.1.1.

4.3 Systematic Sampling Algorithm for Residual Source

The LDFE representation given by Eqs. (4.2), (4.6), and (4.7) is substituted into Eq. (4.10) and evaluated to produce the residual source for each ECMC batch. The MC source $r^{(m)}(x, \mu)$ in Eq. (4.12) consists of volumetric sources and face sources that are sampled. The face sources result from the spatial derivative applied to the discontinuities in the trial space, including a discontinuity at the boundaries for incoming directions [29]. The source can also produce positive and negative weight particles. The probability distribution function (PDF) for sampling particle coordinates is formed by dividing $r^{(m)}(x, \mu)$ by $\|r^{(m)}(x, \mu)\|_1$, i.e., the L_1 norm over space and angle of the residual. Particle coordinates (in x and μ) are sampled from the strictly positive PDF; then, if the residual is negative at the sampled coordinates, the weight of the particle history is negative. With the statistical weights of each particles normalized to unity, then the tallies must be multiplied by $\|r^{(m)}\|_1$ to produce the correct magnitude for moments of error. More details on specific equations for evaluating integrals of the residual for steady-state neutronics problems can be found in [29].

As a method to improve statistical efficiency within a batch, a modified version

of the systematic sampling method [31] (a form of stratified sampling) was implemented for determining the number of histories sampled from each space-angle cell. In the systematic sampling algorithm, the number of particle histories sampled in each space-angle cell is predetermined and proportional to the integral of the PDF over that cell. The goal is to effectively distribute particle histories to regions of importance, but to sample a preset, minimum number of histories N_{\min} in less probable regions; this is to limit bad statistics in low probability cells (this is primarily important for adaptively refined meshes). However, there is no need to sample histories from regions in thermal equilibrium, where the probability of a particle being born is on the order of roundoff. In most of the simulations performed for this work $N_{\min} = 1$; this choice is made to keep the total number of histories per time step constant throughout the simulation for comparison to IMC.

The unmodified probability of a particle being born in cell ij is

$$p_{ij} = \frac{\|r^{(m)}\|_{1,ij}}{\|r^{(m)}\|_1} \quad (4.16)$$

where $\|r\|_{1,ij}$ is the L_1 norm over cell ij , including the upwind face and interior volumetric source. Thus, the number of particles in cell ij is

$$N_{ij} = \begin{cases} \lfloor (N_b p_{ij}) \rfloor & N_b p_{ij} > N_{\min} \\ 0 & p_{ij} < O(\epsilon_{prec}) \\ N_{\min} & \text{else} \end{cases} \quad (4.17)$$

where N_{\min} is the minimum number of histories in significant cells, N_b is the total number of histories sampled that batch, and ϵ_{prec} is on the order of double precision. Particle weights must be adjusted to account for the difference between the number sampled from a particular cell and the original probability of that element being

sampled. This rounding requires some additional histories needing to be sampled, or removed, to reach a specific number of histories. These modifications are made to the most probable cell

The algorithm for sampling each of the N_{ij} starting histories, from each ij element, is

1. Sample random number $\eta \sim U(0, 1)$

(a) If $\eta < \|r_{\text{face}}^{(m)}\|_{1,ij} / \|r^{(m)}\|_{1,ij}$:

- Sample (x, μ) from $\bar{r}_{ij,\text{face}}$ face source with rejection sampling

(b) Else:

- Sample (x, μ) from $\bar{r}_{ij,\text{int}}$ volumetric source using rejection sampling

2. Set particle weight to $p_{ij}N_b/N_{ij}$

where $\bar{r}_{i,\text{face}}$ and $\bar{r}_{i,\text{int}}$ are the upwind face and interior residual in cell ij .

The residual gives a good indication of where histories are most likely to contribute to the error, particularly in optically thick cells where particles do not transport long distances. Systematic sampling is a variance reduction technique that reduces the variance of the function, i.e., the residual, being sampled [31]. Thus, we expect variance to be reduced by more efficiently sampling the residual in optically thick cells. In thin cells, where particles transport farther, this sampling procedure does not guarantee less variance overall.

4.4 Continuous Weight Deposition Tallies

During a MC batch, moments of the error are tallied. The necessary moments of the error are defined analogously to Eq.'s (4.3)–(4.5). The tallies are evaluated by weighting the particle density with the appropriate basis function and integrating along the history path through the cell. The LDFF representation results in

local tallies where only particles entering a particular cell contribute to that cell's estimators. For the cell average, the n -th particle that enters the cell ij makes the contribution, or *score*,

$$\epsilon_{a,ij}^n = \frac{1}{h_i h_j} \int_{s_o^n}^{s_f^n} w^n(x, \mu) ds, \quad (4.18)$$

where s_o^n and s_f^n are the beginning and end of the n -th particle track in the cell and $w(x, \mu)$ is the weight of the error particle in the MC simulation.

As in [28], because we are solving a pure absorber problem with Monte Carlo, we will allow particles to stream without absorption to reduce statistical variance in the tallies. The weight of particles is reduced deterministically along the path as they stream, with no need to sample a path length. Histories are allowed to stream in this manner for 6 mean free paths (mfp) before switching to analog path length sampling; this limits the tracking of very small weight histories. The choice of 6 mfp allows particles to continuously deposit weight until they reach 0.25% of their original weight. Path lengths are tracked in terms of mfp, so there is no need to resample at material interfaces.

Weight is attenuated exponentially, i.e., $w(x, \mu) \propto \exp(-\sigma_t^{\text{eff}}|x/\mu|)$, where for the time-discretized equations $\sigma_t^{\text{eff}} = \sigma_t + 1/(c\Delta t)$. Substitution of the weight representation into Eq. (4.18) produces the result

$$\epsilon_{a,ij}^n = \frac{w(x_0, \mu)}{\sigma_t^{\text{eff}} h_i h_j} \left(1 - e^{-\sigma_t^{\text{eff}} s^n}\right). \quad (4.19)$$

Here, $w(x_0, \mu)$ is statistical weight of the particle at the start of the path and s^n is the length of the track. The contribution of a particle track to ϵ_x is given by

$$\epsilon_{x,ij}^n = \frac{w(x_0, \mu)}{h_i^2 h_j \sigma_t^{\text{eff}}} \left[x_0 - x_f e^{-\sigma_t^{\text{eff}} s^n} + \left(\frac{\mu}{\sigma_t^{\text{eff}}} - x_i \right) \left(1 - e^{-\sigma_t^{\text{eff}} s^n}\right) \right], \quad (4.20)$$

where x_0 and x_f are the beginning and ending x coordinates of the n -th path. The contribution to the first moment in μ is

$$\epsilon_{\mu,ij}^n = \frac{w(x_0, \mu)}{h_j^2 h_i \sigma_t^{\text{eff}}} (\mu - \mu_j) \left(1 - e^{-\sigma_t^{\text{eff}} s^n}\right), \quad (4.21)$$

where the particle x -direction cosine μ does not change, because it is a pure-absorber simulation. The unbiased estimators for the moments of the error, e.g., $\hat{\epsilon}_{a,ij}$, are simply the average score from all histories:

$$\hat{\epsilon}_{a,ij}^{(m)} = \frac{1}{N_b} \sum_{n=1}^{N_b} \epsilon_{a,ij}^n \quad (4.22)$$

where N_b is the number of particle histories performed within that batch.

4.4.1 Face Tallies and correction near $\mu = 0$

Face-averaged estimators of $\epsilon(x, \mu)$ are required to compute the outflow for estimating the spatial closure discussed in Sec. 3.6. The standard face-based tallies [31, 9] are used. Tallies are weighted by the appropriate basis functions to compute a linear FE projection in μ at each face. The tally score, for the angular-averaged error $\epsilon_{a,i}$ is defined as

$$\hat{\epsilon}_{a,i\pm 1/2,j} = \frac{1}{N} \sum_{m=1}^{N_{i\pm 1/2,j}} \frac{w_m(x_{i\pm 1/2}, \mu)}{h_\mu |\mu|}, \quad (4.23)$$

where N is the number of histories performed and $N_{i\pm 1/2,j}$ is the number of histories that crossed the surface $i \pm 1/2$, in the j angular element. For the first moment, the tally is

$$\hat{\epsilon}_{\mu,i\pm 1/2,j} = \frac{1}{N} \sum_{m=1}^{N_{i\pm 1/2,j}} 6 \left(\frac{\mu - \mu_j}{h_\mu} \right) \frac{w_m(x_{i\pm 1/2}, \mu)}{|\mu| h_\mu}. \quad (4.24)$$

For positive and negative directions, solutions are only tallied on the $x_{i+1/2}$ and $x_{i-1/2}$ faces, respectively. Particles are only tallied after leaving a cell, and, as discussed in

Section 4.5, particles born on a surface do not contribute to the tally of that surface.

Near $\mu = 0$, particles can contribute large scores to the zeroth angular moment that lead to large and unbounded variances [9]. To avoid large variances, we have applied the standard fixup [35, 9]. For $|\mu|$ below some small value μ_{cut} , particles contribute the expected score over the range $(0, |\mu_{cut}|)$ for an approximate isotropic particle density. Thus, scores in this range have no variance, but are biased for non-isotropic intensities. For all results in this work $\mu_{cut} = 0.01$. Assuming an isotropic particle density I_0 , the average of $1/\mu$, for positive μ , is

$$\overline{1/\mu} = \frac{\int_0^{\mu_{cut}} \frac{1}{\mu} I_0 d\mu}{\int_0^{\mu_{cut}} I_0 d\mu} = \frac{2}{\mu_{cut}}. \quad (4.25)$$

For negative μ , $\overline{1/\mu} = -2/\mu_{cut}$. All particles in the range $(0, |\mu_{cut}|)$ contribute the expected score by evaluating the appropriate estimator at $\pm\mu = \pm\mu_{cut}$. It is noted that the first angular moment would be well behaved, but it is inconsistent to only modify the zeroth moment in the I_μ estimators. Additionally, assuming an isotropic intensity near $\mu = 0$ helps to limit the first μ moment, where the LD trial space often cannot resolve the solution anyways.

4.5 ECMC Solution with Linear Doubly-Discontinuous FE Trial Space

In this section, the ECMC method is extended to a spatially linear, doubly-discontinuous (LDD) trial space. This extension is necessary for computing the HO spatial closure for the LO equations discussed in Sec. 3.6. To incorporate a projection of the MC solution at faces, a second discontinuity is introduced into the trial space.

The LDD trial space is demonstrated for the x variable in Fig. 3.3. For the HO solver, the LDD trial space is the same as the LDFE space-angle trial space, except

for an extra discontinuity in space at the outflow face. The solution at faces is linear in angle over the angular width of each x - μ cell. The LDD representation for cell ij is

$$\tilde{I}_{ij}(x, \mu) = \begin{cases} I_{a,i-1/2,j} + \frac{2}{h_j} I_{\mu,i-1/2,j} (\mu - \mu_j) & x = x_{i-1/2} \\ I_{a,ij} + \frac{2}{h_i} I_{x,ij} (x - x_i) + \frac{2}{h_j} I_{\mu,ij} (\mu - \mu_j) & x_{i-1/2} < x < x_{i+1/2} \\ I_{a,i+1/2,j} + \frac{2}{h_j} I_{\mu,i+1/2,j} (\mu - \mu_j) & x = x_{i+1/2} \end{cases} \quad (4.26)$$

for $\mu_{j-1/2} \leq \mu \leq \mu_{j+1/2}$. The face-tallied quantities $I_{a,i\pm 1/2}$ and $I_{\mu,i\pm 1/2}$ are shared between adjacent cells, so the expression is the same for positive and negative μ . The linear representation at faces preserves all angular moments of the intensity needed for the spatial closure and face-averaged consistency terms.

The residual source and process of estimating moments of the error on the interior of space-angle cells is unchanged. The process of estimating the solution on the outgoing face requires tallying the error when particles leave a cell, using the face-averaged tallies discussed in Section 4.4.1. Face-averaged consistency terms are directly evaluated using $\tilde{I}(x_{i+1/2}, \mu)$ evaluated at the face of each coarse mesh cell.

The inclusion of the outflow discontinuity in space has a minimal effect on the treatment of the residual source. Applying L to the LDD intensity given by Eq. (4.26), results in two δ functions at each interior face. For *positive flow*, at a face $x_{i+1/2}$, the face portion of the residual is defined as

$$r_{\text{face}}(x_{i+1/2}) = -\mu \frac{\partial \tilde{I}^{(m)}}{\partial x} \Big|_{x=x_{i+1/2}} \quad (4.27)$$

$$= r_{\text{face}}(x_{i+1/2}^-) \delta^-(x - x_{i+1/2}) + r_{\text{face}}(x_{i+1/2}^+) \delta^+(x - x_{i+1/2}) \quad (4.28)$$

where

$$r_{\text{face}}(x_{i+1/2}^-) = -\mu \left(\tilde{I}^{(m)}(x_{i+1/2}, \mu) - \tilde{I}^{(m)}(x_{i+1/2}^-, \mu) \right) \quad (4.29)$$

$$r_{\text{face}}(x_{i+1/2}^+) = -\mu \left(\tilde{I}^{(m)}(x_{i+1/2}^+, \mu) - \tilde{I}^{(m)}(x_{i+1/2}, \mu) \right). \quad (4.30)$$

Here, $I^{(m)}(x_{i+1/2}, \mu)$ is the face-estimated solution at $x_{i+1/2}$ and $I^{(m)}(x_{i+1/2}^+)$ and $I^{(m)}(x_{i+1/2}^-)$ are the LDFE solution *extrapolated* to $x_{i+1/2}$ from the x cell $i+1$ and cell i , respectively; all three terms are linear in μ over $\mu_{j-1/2} \leq \mu \leq \mu_{j+1/2}$. Particles sampled from the two δ -functions have the same starting location. The only difference is, for positive μ , only the particles sampled from $r_{\text{face}}(x_{i+1/2}^-)$ will contribute to the face tally at $x_{i+1/2}$; the opposite is true for negative μ .

To reduce variance, we do not sample the two δ functions independently. Instead, the two δ -functions are combined into a single face source in each element², and particles do *not* score at the face from which they are sampled. To account for the untallied error, we add the analytic contribution to $\epsilon_{i+1/2}$ from $r_{\text{face}}(x_{i+1/2}^-)$, at the end of each batch. This analytic contribution to the error at faces is derived in Sec. A.3. The update for $I(x_{i+1/2}, \mu)$ becomes

$$\tilde{I}^{(m+1)}(x_{i+1/2}, \mu) = \tilde{I}^{(m)}(x_{i+1/2}^-, \mu) + \epsilon^{(m)}(x_{i+1/2}, \mu) \quad \mu > 0 \quad (4.31)$$

$$\tilde{I}^{(m+1)}(x_{i+1/2}, \mu) = \tilde{I}^{(m)}(x_{i+1/2}^+, \mu) + \epsilon^{(m)}(x_{i+1/2}, \mu) \quad \mu < 0 \quad (4.32)$$

This result has the serendipitous effect that the estimation of the solution on a face depends only on the previous interior solutions $\tilde{I}^{(m)}(x_{i+1/2}^-, \mu)$ and $\tilde{I}^{(m)}(x_{i+1/2}^+, \mu)$ and not the previous face value $\tilde{I}^{(m)}(x_{i+1/2}, \mu)$. This has an additional benefit that the face values can be estimated at any chosen batch, in particular cells. For this work,

²The combination of the two δ -functions produces the same residual source as the original LD trial-space residual.

the solution is estimated in all cells in the LDD trial space.

5. COMPUTATIONAL RESULTS

In this chapter, we compare results of the time-discretized HOLO method to IMC with a source tilting algorithm for two test problems [37]. Also, we briefly compare performance in Section 5.3. For all IMC results, no local, discrete diffusion acceleration methods for effective scattering (e.g., those in [13, 6]) are applied. Additionally, we demonstrate the efficiency advantage of ECMC in our HOLO algorithm by comparing the results to the same HOLO algorithm if the ECMC algorithm is replaced with a standard Monte Carlo (SMC) simulation. Finally, we present results that demonstrate preservation of the equilibrium diffusion limit and the discrete maximum principle by the HOLO algorithm. Some of the results in this section were published previously in [2]. The results in this chapter use the simplified fix-ups discussed in Sec. 3.4 and Sec. 4.2.3 when negative values of the intensity occur; more sophisticated solution methods are investigated in Chapter 7.

A measure of variance in cell-averaged scalar intensities was calculated to provide a quantitative measure of the statistical accuracy of different solution methods. To form sample standard deviations, twenty independent simulations for each particular result were performed using unique random number generator seeds. The variance of a particular cell-averaged $\phi(x)$ is

$$S_i^2 = \frac{20}{20-1} \sum_{l=1}^{20} (\overline{\phi}_i - \phi_i^l)^2, \quad (5.1)$$

where ϕ_i^l is the cell-averaged scalar intensity for cell i from the l -th of 20 independent simulations and $\overline{\phi}_i$ is the corresponding sample mean from the 20 simulations. To

provide a normalized, spatially-integrated result, we form a norm over cells as

$$\|s\| = \left(\frac{\sum_{i=1}^{N_c} S_i^2}{\sum_{i=1}^{N_c} \phi_i^{-2}} \right)^{1/2}, \quad (5.2)$$

where N_c is the number of spatial cells.

We will also form a figure of merit (FOM) to demonstrate how statistical accuracy scales with the number of histories performed. Our FOM is defined as

$$\text{FOM} = \frac{1}{N_{\text{tot}} \|s\|^2} \quad (5.3)$$

where N_{tot} is the total number of histories performed over the simulation. A larger value of the FOM indicates that the method produced less variance in the solution per history performed, for a given problem. This form of the FOM is typically chosen because the variance is expected to reduce inversely proportional to N_{tot} , so for standard MC simulations the FOM becomes, on average, independent of N_{tot} [31]. The FOM is not necessarily expected to be independent of N_{tot} for IMC or our HOLO method due to correlation of the solution between time steps; additionally, ECMC has correlations between batches.

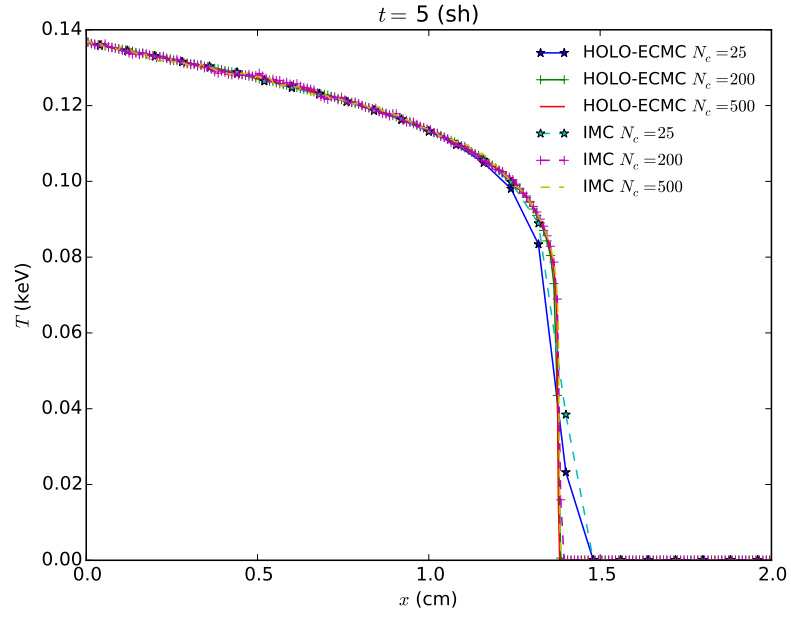
5.1 Marshak Wave

For the first problem, the radiation and material energies are initially in equilibrium at 2.5×10^{-5} keV. An isotropic incident intensity of 0.150 keV is applied at $x = 0$; the incident intensity on the right boundary is 2.5×10^{-5} keV. The material properties are $\rho = 1$ g cm $^{-3}$ and $c_v = 0.013784$ jks/keV-g. The absorption cross section varies as $\sigma(T) = 0.001 \rho T^{-3}$ (cm $^{-1}$), for T in keV. The simulation was advanced until $t = 5$ sh (1 sh $\equiv 10^{-8}$ s) with a fixed time step size of 0.001 sh. For comparison

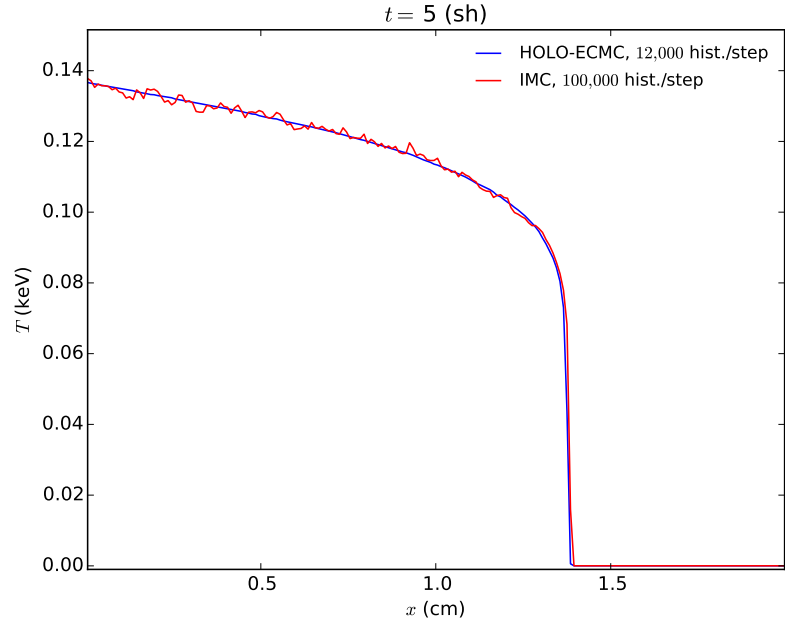
purposes, we have not used adaptive mesh refinement, only performed one HOLO iteration per time step, and use a fixed 3 HO batches with equal number of histories per batch. A relative tolerance of 10^{-6} for the change in $\phi(x)$ and $T(x)$ was used for the LO newton solver for all results. Radiation energy distributions are plotted as an effective temperature given by $T_r = (\phi/(ac))^{0.25}$. The effective temperature represents the temperature of the material, if the material and temperature were in equilibrium. Cell-averaged quantities are plotted. For this problem, when negative values for $\phi^{n+1,\pm}(x)$ were detected, the lumping-equivalent discretization was used within those cells and that Newton step was repeated. Non-physical angular consistency terms were replaced with S_2 -equivalent terms.

Figure 5.1a on page 64 compares the cell-averaged radiation temperatures for the IMC and HOLO method with ECMC, for various number of spatial mesh cells N_c ; we have used HOLO-ECMC to denote our algorithm because later results will use different HO solvers. For all IMC calculations, $n = 10^5$ histories per time step were used. For the HOLO method, we have used 4 equal-sized cells in μ for the finite-element angular mesh used by the ECMC solver. The spatial grid is the same for the HO and LO solvers. For the cases of $N_c = 25$ and $N_c = 200$, 4,000 histories per batch ($n = 12,000$ per time step) were used. For $N_c = 500$, 16,000 histories per time step were used due to increased number of space-angle cells that need to be sampled. The IMC and HOLO solutions agree as the mesh is converged. There is similar agreement in the location of the wavefront due to the linear shape of the emission source over a cell. The cells nearest the wavefront required use of the lumping-equivalent discretization of the radiation and S_2 equivalent terms during the LO solve, resulting in strictly positive cell-averaged quantities.

Figure 5.1b compares solutions for the case of 200 cells. For the IMC solution 10^5 histories per time step were simulated; for the HOLO method only 4,000 histories



(a) Convergence of IMC and HOLO-ECMC solutions.



(b) Comparison of solutions for 200 spatial cells.

Figure 5.1: Comparison of radiation temperatures for Marshak wave problem at $t = 5$ sh.

per batch (12,000 per time step) were simulated. There is significant statistical noise in the IMC solution compared to the HOLO solution. The HOLO solution visually demonstrates no statistical noise. Because the ECMC solve is only determining the change over the time step, the statistical noise in the result is small relative to the magnitude of I^{n+1} . Also, the source sampling only places particles in cells where the residual is large. No particles are sampled in the equilibrium region out front of the wave. Only a few angular cells are necessary to accurately reproduce the mean intensity for this problem.

Table 5.1 compares $\|s\|$ and the FOM for IMC and the HOLO method, for different numbers of histories per time step. The FOM results are normalized to the value for IMC with $n = 12,000$. The HOLO method demonstrates less variance for the same numbers of histories, producing FOM values that are two orders of magnitude greater than for IMC. Where as the FOM remains relatively constant for IMC, as n is increased the FOM improves for the HOLO method. This is a result of each batch producing more statistically accurate estimates of the error ϵ , which results in an increased convergence rate of ϵ overall.

Table 5.1: **Comparison of sample statistics for the Marshak Wave problem. Simulation end time is $t = 5$ sh.**

hist./step	$\ s\ $		FOM	
	IMC	HOLO-ECMC	IMC	HOLO-ECMC
12,000	3.40%	0.28%	1	145
100,000	1.22%	0.057%	0.93	422

5.2 Two Material Problem

This problem consists of an optically thin (left) and an optically thick (right) material region, with temperature-independent cross sections. The material properties are given in Table 5.2. Initially the radiation and material energies are in equilibrium at a temperature of 0.05 keV. An isotropic incident intensity of 0.500 keV is applied at $x = 0$ at $t = 0$; the isotropic incident intensity on the right boundary is 0.05 keV. The simulation end time is 5 sh. For all HOLO simulations, we have used 8 equal-sized mesh cells in μ . In cells nearest the wavefront we use the fix-up detailed in Sec. 3.4 that strictly enforces the floor temperature and preserves half-range balance. The fix-up was applied, along with S_2 equivalent terms during the LO solve.

Table 5.2: Material properties for two material problem

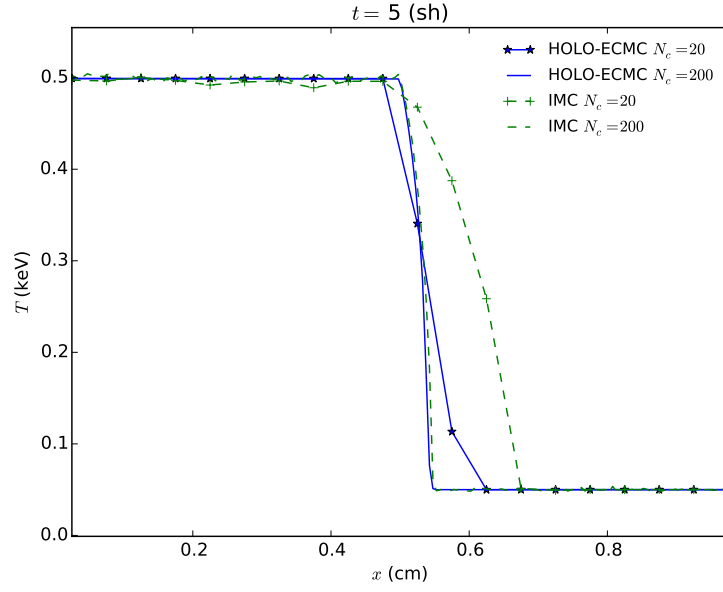
	$x \in [0, 0.5)$ cm	$x \in [0.5, 1.0]$ cm
σ_a (cm ⁻¹)	0.2	2000
ρ (g cm ⁻³)	0.01	10.0
c_v (jks/keV-g)	0.1	0.1

Fig. 5.2a compares the HOLO and IMC radiation temperatures at the end of the simulation. The IMC and HOLO results show good agreement over the finer mesh. On the coarse mesh ($N_c = 20$), the LDFE representation of T^4 in the HOLO method predicts the location of the wavefront more accurately than the IMC method with source tilting.

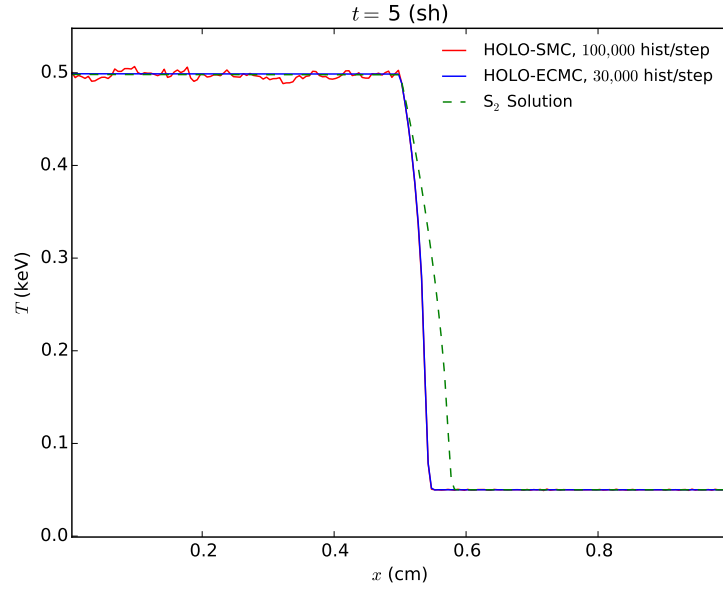
Fig. 5.2b demonstrates the benefit of ECMC as a HO solver compared to standard MC. The HOLO algorithm with the ECMC HO solver (HOLO-ECMC) results

are for running 3 batches of 10,000 histories, per time step. The solution for the HOLO method with a standard MC solver as the HO solver (HOLO-SMC) with standard source sampling uses 10^5 histories per time step. The HOLO-SMC solution demonstrates significant statistical noise. This noise is introduced into the LO solver by bad statistics in computing the consistency terms. Also plotted is an S_2 solution obtained with consistency terms that are equivalent to S_2 and no HO correction. The S_2 solution results in an artificially fast wavefront, as expected, demonstrating the necessity of HO correction in this problem.

Table 5.3 compares the FOM and $\|s\|$ for IMC and the HOLO-ECMC method. The FOM values are normalized to the value for IMC with $n = 30,000$. The end time was reduced to 2 sh for these results to reduce computational times. The reduction in variance by the HOLO method over IMC is substantial. The improvement of the FOM for the HOLO method compared to IMC is greater than for the Marshak wave problem. This improvement is because the wave moves much slower in right region of this problem, due to the large, constant cross section. Also, in the optically thin region of the problem the solution quickly comes to equilibrium. Thus, the ECMC algorithm has to estimate a very small change in the intensity over a time step.



(a) Comparison of IMC and HOLO-ECMC.



(b) Comparison of SMC and ECMC HO solvers.

Figure 5.2: Comparison of radiation temperatures for two material problem.

Table 5.3: **Comparison of sample statistics for the two material problem for 200 x cells. Simulation end time is $t = 2$ sh.**

	$\ s\ $		s_{\max}	
hists./step	IMC	HOLO-ECMC	IMC	HOLO-ECMC
30,000	3.63%	0.01%	1	104,000
100,000	1.96%	0.003%	1.03	360,000

5.3 Performance comparison of IMC and HOLO-ECMC

We have measured the total CPU time for simulations to provide a simplified measure of the computational cost. These results compare how computational times change for the two different problems and how the methods scale with time step size and particle histories. Absolute comparisons in the computational cost of the two methods cannot be made, because the methods are implemented in different code infrastructures. Additionally, the HOLO method fully resolves non-linearities at each time step, whereas IMC is using a single linearized step with lagged cross sections. Simulations were performed on the same processor, using a single CPU core. Reported times are the average of 10 runs and all results used 200 x cells, $\Delta t = 0.001$ sh, and an end time of $t = 2$ sh.

Table 5.4 compares the average simulation time per history performed for the Marshak wave problem. The average time per history is computed by dividing the total simulation time by the total number of histories performed (e.g., the time of the LO solves is included for the HOLO method). Results are given for different numbers of histories per time step, as well as a case with an increased time step size. The table also includes the number of LO iterations performed per LO solve for the HOLO method, averaged over all time steps; there are two LO solves per time step.

The same results are reported for the two material problem in Table 5.5.

The HOLO method does not scale with the number of histories due to the fixed cost of the LO solver. The cost of the LO solver is more significant at the lower history counts compared to the case of 10^5 histories, for both problems. There is a slight increase in the number of newton iterations as the time step is increased, but the average cost per history is not significantly increased. Similar to the results in [28], as the time step size is increased to 0.005 sh, the IMC method increases in cost per time step, due to an increase in effective scattering events, particularly for the two material problem. Because the cross sections in the two material problem do not have a T^{-3} behavior, the cost of the effective scattering cross section in IMC is more apparent, resulting in longer simulation times.

Table 5.4: **Comparison of average CPU times per history and LO iteration counts for the Marshak Wave problem.**

hists./step	$\Delta t(sh)$	IMC ($\mu s/hist.$)	HOLO-ECMC ($\mu s/hist$)	Newton iters./LO solve
100,000	0.001	10	5.3	3.8
12,000	0.001	9.7	8.1	4.1
12,000	0.005	19	9.4	6.2

Table 5.5: **Average CPU times per history and LO iteration counts required for the two material problem.**

hists./step	$\Delta t(sh)$	IMC ($\mu s/hist.$)	HOLO-ECMC ($\mu s/hist$)	Newton iters./LO Solve
100,000	0.001	17	3.5	4.9
30,000	0.001	18	6.9	5.0
30,000	0.005	59	7.4	7.6

5.4 Comparison of different HO Solvers

In this section we compare the results of our HOLO algorithm with different HO solvers for the test problems in Section 5.1 and 5.2. We compare standard MC (SMC) as a HO solver to the HOLO algorithm with ECMC using both three batches and a single batch, per time step. The use of a single batch is similar to the approach in [41]. Results are tabulated for 200 x cells, using the same total number of histories per time step, divided evenly among the batches.

Tables 5.6 and 5.7 compare the results for the Marshak wave and two material problems. The number of batches for each ECMC case is indicated in parenthesis. The FOM values are normalized to the reference IMC result for the corresponding problem. For HOLO-SMC there is minimal reduction in variance compared to IMC in the Marshak wave problem, and the two material problem actually demonstrates worse variance. Sufficient histories are not performed to accurately estimate consistency terms throughout the problem. For ECMC, a single batch produces less variance than the case of three equal batches. This indicates that if the solution cannot be resolved with the trial space (i.e., the intensity is driven negative), a single large batch may be more accurate. It is noted that these results only estimate statistical variance and do not strictly account for accuracy.

Table 5.6: **Comparison of sample statistics for the Marshak Wave problem. Number of ECMC batches is indicated in parenthesis.**

hists./step	$\ s\ $			FOM		
	SMC	ECMC (1)	ECMC (3)	SMC	ECMC (1)	ECMC (3)
12,000	2.77%	0.10%	0.28%	1.50	1280	145
100,000	0.98%	0.03%	0.06%	1.43	1270	422

Table 5.7: **Comparison of sample standard deviations for the two material problem. Number of ECMC batches is indicated in parenthesis.**

	$\ s\ $			FOM		
hists./step	SMC	ECMC (1)	ECMC (3)	SMC	ECMC (1)	ECMC (3)
30,000	5.35%	0.002953%	0.011%	0.46	1.51×10^6	1.04×10^4
100,000	2.85%	0.001474%	0.0033%	0.49	1.80×10^6	3.59×10^4

5.5 Pre-heated Marshak Wave Problem and Adaptive Mesh Refinement

Finally, to demonstrate the potential of ECMC with adaptive space-angle mesh refinement, we perform results for a modified Marshak wave problem. The problem is modified so that the LDFE trial space can accurately represent the solution (i.e., the intensity is strictly positive). Mesh refinement is of minimal use in the previous problems due to most of the error existing at the wavefronts, caused by the large cross sections. The modified problem has the same material properties and left boundary source as the Marshak wave problem in Section 5.1. However, the initial equilibrium temperature and right boundary condition are raised to 0.03 keV. The higher initial temperature reduces the initial cross section and increases the strength of the emission source within cells. The LDFE mesh can now sufficiently resolve the solution and lumping is not required by the LO solution. The simulation end time is 0.5 sh with a constant time step of $\Delta t = 0.001$ sh.

Fig. 5.3 compares the result from HOLO-ECMC with three batches and IMC. It was found that 100 x cells was sufficient to resolve the solution spatially. There is slightly more noise in IMC past the wavefront due to the increased emission source. Additionally, the cross section is thin enough that some photon energy is able to reach the right boundary, in front of the wavefront.

Table 5.8 compares the variances for this problem for the various HO solvers. The FOM values are normalized to the case of HOLO-SMC with 12,000 histories per time step. The final row of the table is for an ECMC simulation with adaptive mesh refinement (AMR). The strategy for refinement is described in Appendix ??.

The adaptive mesh refinement case used a total of nine batches, with a refinement occurring at the end of the third and sixth batches, for every time step. The initial number of histories was adjusted so that the average number of histories per time step is near 100,000; on average 99,881 histories per time step were used. All ECMC meshes used 4 equally-spaced μ cells initially. The improvement in variance by ECMC compared to SMC is not as significant as for the other problems. This is a result of the reduced cross section leading to intensity changing throughout the spatial and angular domains. The FOM is highest for the case of ECMC with adaptive refinement. When the solution can be resolved, the adaptive algorithm allows for a higher convergence rate of statistical variance. It is noted that the consistency terms and LO solution are still computed over the fixed, coarser mesh. However, in general, the refined mesh can produce higher accuracy in consistency terms that is not being measured by the FOM.

Table 5.8: Comparison of sample statistics for the pre-heated marshak wave problem for 100 x cells. Number of ECMC batches is indicated in parenthesis.

hist./step	$\ s\ $			FOM		
	SMC	ECMC (1)	ECMC (3)	SMC	ECMC (1)	ECMC (3)
12,000	0.86%	0.13%	0.24%	1	41	13
100,000	0.16%	0.042%	0.08%	3.32	52	15
99,881 (AMR, 9 batches)	—	0.038%		—	61	

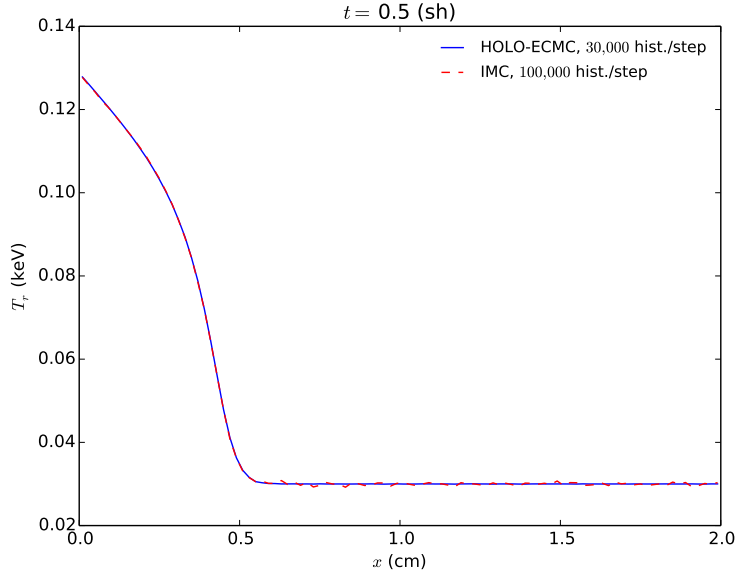


Figure 5.3: Comparison of radiation temperatures for the pre-heated Marshak wave problem for 100 x cells at $t = 0.5$ sh.

5.6 Accuracy in the Equilibrium Diffusion Limit

As discussed in Sec. 3.5, we must ensure our method preserves the equilibrium diffusion limit (EDL). We have produced an EDL test problem by adjusting material properties to produce a strongly diffusive domain. This EDL problem has constant cross sections with $\sigma_a = 1000 \text{ cm}^{-1}$, $\sigma_s = 10 \text{ cm}^{-1}$, $\rho c_v = 6.8784 \times 10^{-3} \text{ jk keV}^{-1} \text{ cm}^{-3}$. The initial temperature is 0.01 keV and the domain width is 0.1 cm. The simulation end time is 5 sh, and the step-size increases 5% per time step from $\Delta t = 0.001$ sh to a maximum $\Delta t = 0.01$. In all simulations, 4 μ cells and 3 batches of 4,000 histories were used for the single HO solve, for each time step. We compare HOLO results with a LDFE discretization and a step discretization of the LO equations. The step discretization, with a flat representation over each cell, is known to be inaccurate in the EDL for S_N equations. The step discretization is implemented with the step closure discussed in Sec. 3.6.2 for all cells.

The accuracy in the equilibrium diffusion limit is compared for the two spatial discretizations, for different mesh sizes, in Fig. 5.4. Visually, the LD FE spatial discretization has converged spatially, where both 20 and 200 cells produce the same location of the wave front. However, the step discretization artificially propagates the energy forward, even for the 200 cells case; the inaccuracy is greater than what would be expected from truncation error. The step discretization will only be accurate if the mesh cells are on the order of a mean free path, which is very large for this problem. Although not plotted, the material temperature overlays the radiation temperature for the LD FE solution, in equilibrium with the radiation, as expected.

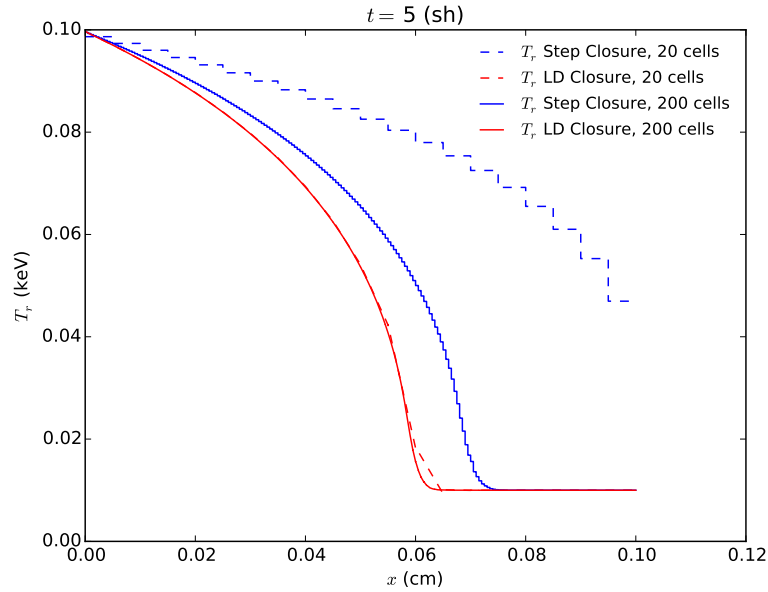


Figure 5.4: Comparison of T_r for a problem in the equilibrium diffusion limit, with step and LD FE discretizations of the LO equations.

5.7 The HO Spatial Closure

To investigate the utility of the face closures we compare to the LD spatial closure for two test problems. We are interested in the accuracy of the solution and consistency between the HO and LO solutions, particularly for coarser meshes. The consistency for the (l) -th particular simulation is measured with the relative L_2 norm of the difference between the projected HO and LO solutions, i.e.,

$$\|\phi_{HO} - \phi_{LO}\|_{2,rel}^{(l)} = \frac{\sqrt{\int_0^X \left(\phi_{HO}^{n+1,(l)}(x) - \phi_{LO}^{n+1,(l)}(x) \right)^2 dx}}{\sqrt{\int_0^X \left(\phi_{LO}^{n+1,(l)}(x) \right)^2 dx}} \quad (5.4)$$

where $\phi_{LO}(x)$ and $\phi_{HO}(x)$ are the LDFF representations in space of the intensity from the HO and LO solvers, from the end of the last time step. The error between a reference solution and a fine solution for the (l) -th simulation is computed as

$$\|e\|_{2,rel}^{(l)} = \frac{\|\phi_{LO}^{n+1,(l)}(x) - \phi_{LO}^{n+1,ref}(x)\|_2}{\|\phi_{LO}^{n+1,ref}(x)\|_2} \quad (5.5)$$

All L_2 norms are computed using quadrature over the finest spatial mesh. An integrated measure of the error in cell-averaged mean intensities on the mesh of the l -th simulation, with $N_c^{(l)}$ spatial cells, is computed as

$$\|e\|_{a,rel}^{(l)} = \left(\frac{\sum_{i=1}^{N_c^{(l)}} \left(\phi_i^{n+1,(l)} - \phi_i^{n+1,ref} \right)^2}{\sum_{i=1}^{N_c^{(l)}} \left(\phi_i^{n+1,ref} \right)^2} \right)^{1/2}, \quad (5.6)$$

where $\phi_i^{n+1,ref}$ is computed by spatially averaging the fine mesh solution over the i -th coarse spatial cell.

The sample mean of each of the above metrics is estimated based on 20 independent simulations; the sample standard deviation for each *mean* is also reported, e.g.,

$$s(\|e\|_{2,rel}) = \left[\frac{1}{20-1} \sum_{l=1}^{20} \left(\|e\|_{2,rel}^{(l)} - \|e\|_{2,rel} \right)^2 \right]^{1/2}, \quad (5.7)$$

where $\|e\|_{2,rel} = \sum_{l=1}^{20} \|e\|_{2,rel}^{(l)} / 20$ is the mean.

5.7.1 Smooth Problem

For this problem, the radiation and material energies are initially in equilibrium at 0.01 keV. An isotropic incident intensity of 0.05 keV is applied at $x = 0$; the incident intensity on the right boundary is 0.05 keV. The material properties are $\rho = 1 \text{ g cm}^{-3}$, $c_v = 0.2 \text{ jks/keV-g}$, and $\sigma_a = 10 \text{ cm}^{-1}$. The simulation end time is 0.5 sh. The time step size increases by 10% each time step until the maximum step size of 0.01 sh is reached, beginning from $\Delta t = 0.001 \text{ sh}$. This problem is intended to have less steep gradients in the intensity by having constant cross sections, a smaller boundary source, and diffusive problem parameters. The problem has a smaller optical thickness than other problems tested so that the face-based solutions can be efficiently estimated, but the small c_v value makes the solution relatively diffusive. This problem did not require the lumped relation to produce positive solutions. However, when projecting from a refined mesh back to the coarse mesh, it was necessary to rotate the solution to be positive.

All simulations of this problem used 585,900 histories divided over 9 ECMC batches; beginning from 30,000 histories and 10μ cells, 30% of cells were adaptively refined every third batch, and the number of histories is increased to keep the average

number of histories per cell constant. We have have performed two outer HOLO iterations over each time step for all cases; it was found that additional iterations did not increase consistency, because of the magnitude of statistical noise. Relative convergence of HOLO iterations was below 10^{-3} for two iterations for all cases. Fig. 5.5 compares cell-averaged radiation temperatures for various spatial closures at coarse mesh sizes and a fine-mesh solution. The HO spatial closures curve is for the scaled-slope closure given by Eq. (3.36). There was visually no difference in the results between the scaled-averaged, scaled-slope, or LD closure. A step closure in all cells was inaccurate for this problem.

Table 5.9 compares the different error metrics for different spatial closures and numbers of cells. The reference solution for all calculations was the average of 10 simulations with $N_c = 500$ spatial cells. In all cases, the HO spatial closure produces higher accuracy in the L_2 norms and greater consistency between the solvers. However, there is not an improvement in accuracy of the cell-averaged intensities. Neglecting noise, the LDFE representation can be third order accurate for the $\|e\|_a$ norm and second-order accurate in the L_2 norm [26]. The statistical noise induced in face tallies makes the additional accuracy that the MC transport can use not greater than the benefit of higher spatial integration by the MC transport. It is noted that, overall, there is very low statistical noise in each of these solutions due to the ECMC method and relatively high number of histories; at lower history counts, the small gains of the HO spatial closure will degrade and stability becomes an issue.

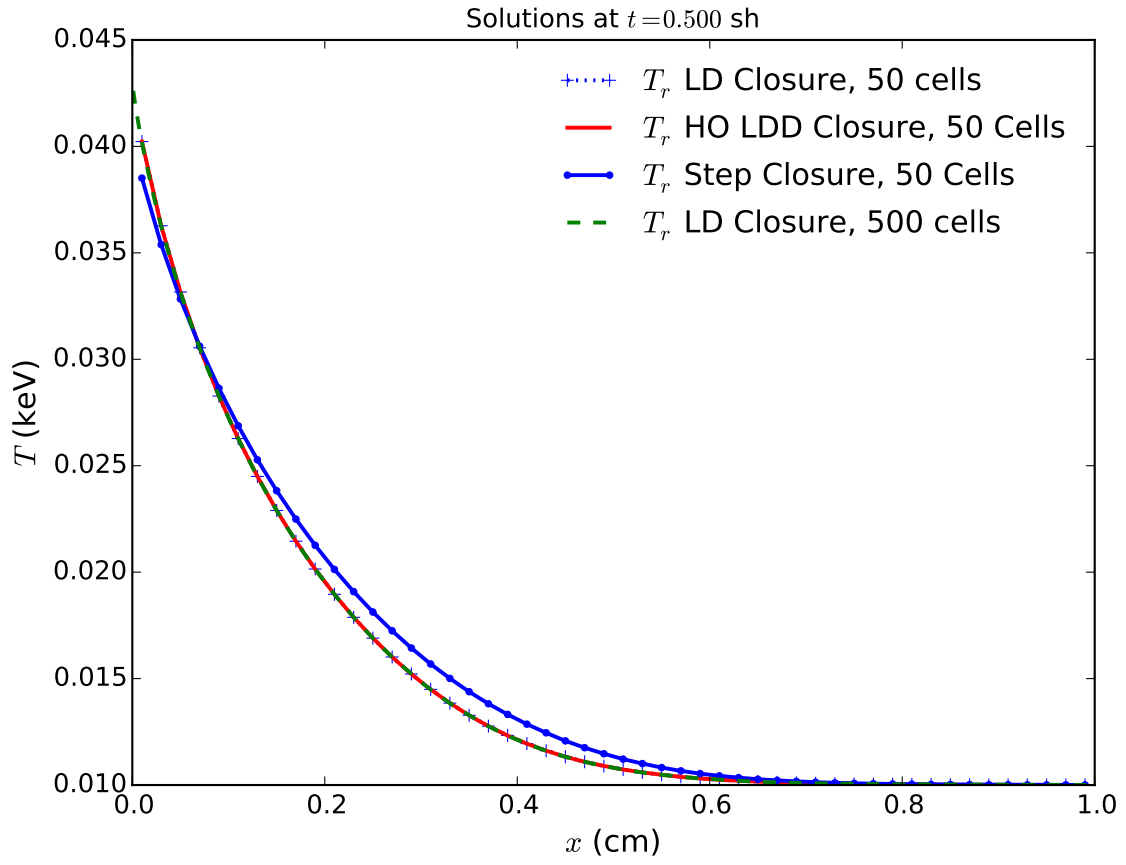


Figure 5.5: Comparison of solutions for smooth problem with different spatial closures.

Table 5.9: Comparison of error metrics, reported as percentages, averaged over 20 simulations of smooth problem. The absolute standard deviation for each value is reported in parenthesis. Reference solution uses 500 cells.

Spatial Closure	$\ e\ _2$	$\ e\ _a$	$\ \phi^{HO} - \phi^{LO}\ _2$
$N_c = 20$ cells			
LDFE	6.60% (0.17%)	2.80% (5.7e-03%)	2.90% (8.1e-03%)
HO: Scaled Slope	6.10% (2.9e-03%)	3.50% (5.8e-03%)	0.021% (8.6e-03%)
HO: Scaled Average	6.10% (2.7e-03%)	3.50% (5.0e-03%)	0.023% (1.1e-02%)
$N_c = 50$ cells			
LDFE	1.60% (7.9e-04%)	0.59% (3.8e-03%)	0.76% (4.8e-03%)
HO: Scaled Slope	1.40% (1.5e-03%)	0.67% (3.2e-03%)	0.012% (4.0e-03%)
HO: Scaled Average	1.40% (1.5e-3%)	0.67% (3.1e-03%)	0.013% (3.9e-03%)
$N_c = 100$ cells			
LDFE	0.53% (2.1e-03%)	0.15% (2.5e-03%)	0.30% (9.7e-03%) %
HO: Scaled Slope	0.45% (1.5e-03%)	0.16% (4.6e-03%)	0.012% (4.8e-03%)
HO: Scaled Average	0.45% (1.4e-03%)	0.16% (4.7e-03%)	0.012% (3.6e-03%)

5.7.2 Two Material Problem

The HO spatial closures were applied to solution of the two material problem detailed in Sec. 5.2. For these results, a small time step size of 0.001 sh was used, with a simulation end time of 2 sh. The scaled-slope closure was found to not stably converge, even for 2 batches of 10^6 histories. The scale-average closure allowed for convergence, with the lumped closure, but temperatures were driven below the floor, and at times negative, leading to inaccurate solution. The inaccuracies result from the outflow being driving negative in cells near the wave front with steep gradients.

The cause is that, although the HO solution was forced positive by scaling moments, and the face solution is positive the closure does not necessarily agree with the true moments. The first moment of the HO solution had to be modified to produce a positive solution, and by trying to use the moment relation in the LO solution, there can be negative solutions. In general, in such difficult to resolve regions, the spatial closure does not gain improvement. Fig. 5.6 depicts cell-averaged results at the end of the simulation. The inaccuracy in ghtly overshoots, the slope changes signs between cells. Additionally, there is great inconsistency as the depressed temperature leads to an inaccurate HO solution. A fundamental problem with the lumping relation is that the first moment equation for the HO solution has a lumped temperature equation

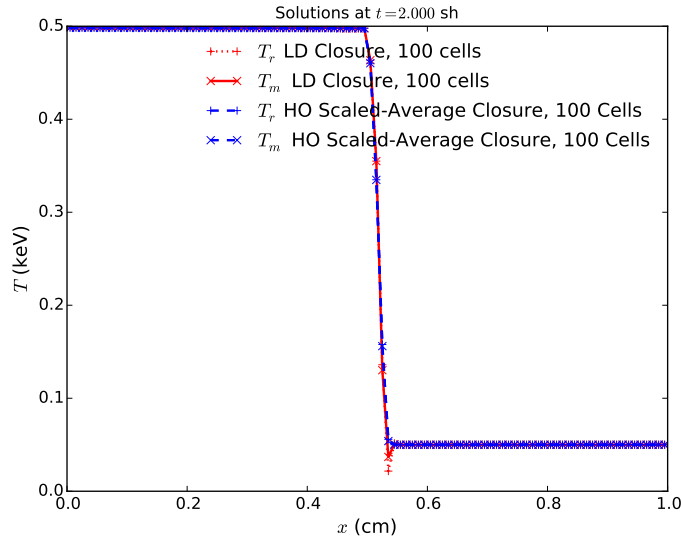


Figure 5.6: Inacurracies for HO spatial closure applied to solution of the two material problem.

5.8 Preservation of the Discrete Maximum Principle

To numerically demonstrate that our method preserves the discrete MP, as discussed in Sec. 1.2.1, we have simulated problems similar to those in [44]. We produce a problem with tightly coupled equations, by decreasing c_v and increasing σ_a , which results in MP violations for IMC at various fixed time step sizes. The spatial and temporal discretization determine the occurrence of MP violations for IMC. In particular, if time steps are too large or spatial mesh cells are too small, IMC will demonstrate MP violations [44]. Here, we have kept the spatial mesh size fixed and increased the time step size to produce MP violations. The material specifications are $\sigma_a = \sigma_{a,0} T^{-3} \text{ cm}^{-1}$, $\sigma_{a,0} = 4 \text{ cm}^{-1} \text{ keV}^3$, $\sigma_s = 0 \text{ cm}^{-1}$, $\rho c_v = 0.0081181 \text{ jks keV}^{-1} \text{ cm}^{-3}$. The domain width is 2.0 cm with $N_c = 150$ uniform spatial mesh cells. The radiation and material energies are initially in equilibrium at 0.01 keV, before an isotropic boundary source of 1 keV is applied at the left boundary at $t = 0$. The simulation end time is $t = 0.1 \text{ sh}$.

The material and radiation temperature are plotted for an IMC simulation with $\Delta t = 0.025 \text{ sh}$ in Figure 5.7. Figure 5.8 depicts the material temperature for various time step sizes and the fixed mesh size of 150 cells. All IMC simulations used 100,000 histories per time step. As demonstrated in Fig. 5.7, the material temperature exceeds the specified boundary temperature and is artificially hotter than the radiation temperature. This artificial “temperature spike” also leads to a slower propagation of the wave [44]. As shown in Fig. 5.8, as larger time-step sizes are taken the nonphysical results worsen with the material temperature exceeding the radiation boundary temperature. It is noted that although the final solution for $\Delta t = 0.0001 \text{ sh}$ obeys the MP, during the first few time steps the temperature spikes are present.

The simulations are repeated with the same specifications for the HOLO method.

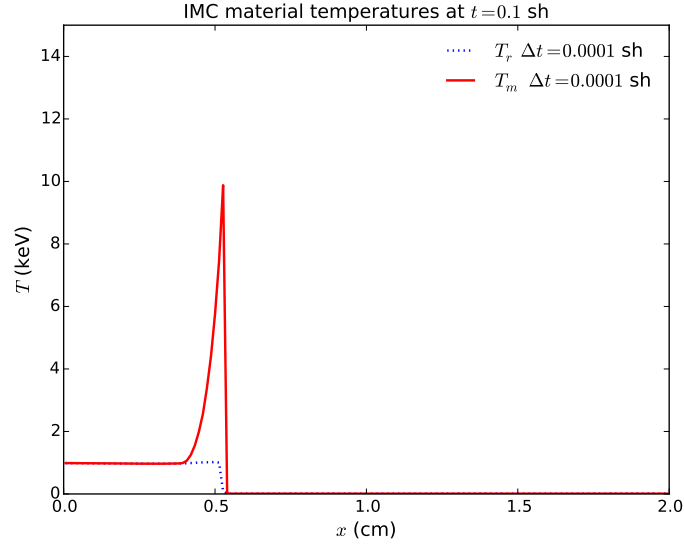


Figure 5.7: T_r and T for MP violation problem with IMC and $\Delta t = 0.001$ sh.

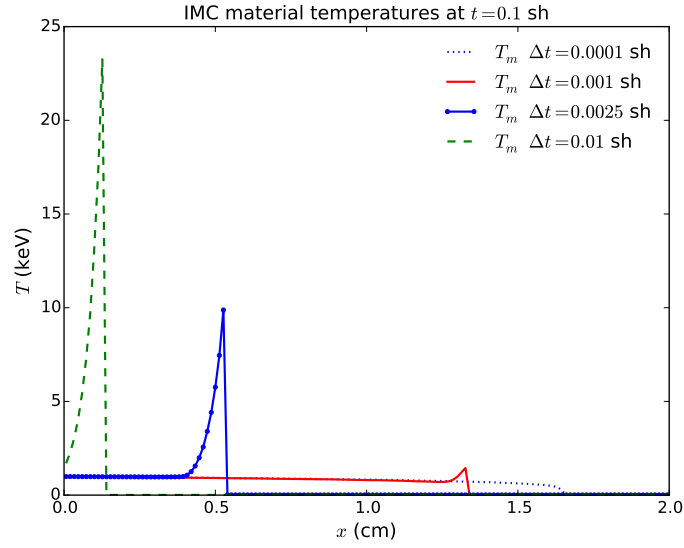


Figure 5.8: T_m for MP violation problem with IMC for various time step sizes.

All HOLO simulations used a fixed mesh of 8 μ cells by 150 x cells, 3 batches per time step, and 6,000 histories per batch. A single HO solve is performed per time step, and the LO relative convergence tolerance is 10^{-6} . The lumping closure is used for the radiation terms in all spatial cells and any negativities in the HO solution are scaled to the floor value as discussed in Sec. 4.2.3. For these simulations, it was necessary to use the damped Newton’s method discussed in Sec. 3.3 to converge the solutions [17]. A fixed damping parameter with a factor of 0.5 was found to stably converge for all time-step sizes that were simulated.

As seen in Fig. 5.9, the HOLO solution does not violate the maximum principle; the temperature is bounded from above by the radiation boundary condition. Table 5.10 demonstrates the LO Newton iteration counts for the HOLO method. For reference, a solution with $\Delta t = 10^{-5}$ sh is given, which required no damping to converge. The damped iterations require more iterations to converge. However, it is necessary to converge the nonlinear iterations to produce physically meaningful solutions to this problem. The advantage of the HOLO method is that there is no additional cost for the HO solution when the damped method is used.

Table 5.10: Comparison of LO Newton iterations for HOLO solution to MP problem and different time step sizes. For $\Delta t = 10^{-5}$ sh, no damping was used; for all other cases a damping factor of 0.5 was used.

Δt (sh)	Newton Iters. / LO Solve
10^{-5}	3.5
10^{-4}	21.0
10^{-3}	28.5
2.5×10^{-3}	29.7
10^{-2}	46.3

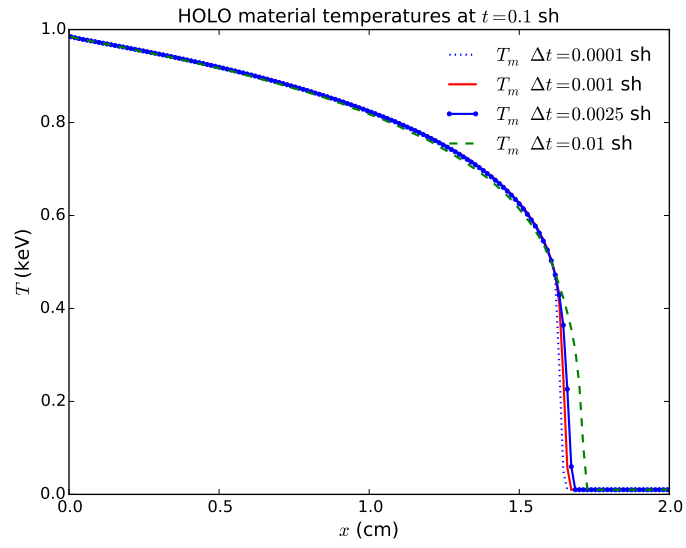


Figure 5.9: T_m for MP violation problem with HOLO method for various time step sizes.

6. ACCELERATED ITERATIVE SOLUTION TO THE LO EQUATIONS

The fully-discrete, S_2 -like LO equations cannot be directly inverted easily in higher spatial dimensions. To demonstrate a possible path forward in higher dimensions, we have investigated the use of a standard source iteration scheme [22] to invert the scattering terms in the linearized LO equations during each Newton iteration. As material properties become more diffusive (e.g., c_v is small and σ_a is large), the effective scattering cross sections becomes large. This results in a spectral radius of source iterations that approaches unity [26]. These regimes are typical in TRT simulations, so an acceleration method for iterative solutions is critical. We have accelerated the source iterations with a nearly-consistent diffusion synthetic acceleration (DSA) method known as WLA [39, 38]. We have also recast the DSA method as a preconditioner to an iterative Krylov solution [8] of the LO equations. Generally, Krylov methods mitigate acceleration losses due to inconsistencies in the acceleration method. In higher dimensions, the use of a Krylov method is necessary for effective acceleration for nearly-consistent acceleration methods in problems with mixed optical thicknesses [8], e.g., typical radiative transfer problems. Also, applying the preconditioned-Krylov approach allows for the use of spatially lumped DSA equations as a preconditioner, with the LO equations using an LD spatial closure.

The remainder of this chapter is structured as follows: The source iteration solution to the LO equations is detailed. Then, the equations for the WLA DSA method are derived and the acceleration algorithm is given. The DSA method is then recast as a preconditioner to a GMRES solution of the scattering iteration equations. Finally, convergence results are compared for several test problems.

6.1 Source Iteration Solution to the Linearized LO Equations

The linearized LO equations can be solved with a source iteration method [22, 20, 23]. In the source iteration process the scattering source is lagged, which uncouples unknowns between the two half-ranges. This produces a lower-triangular system where the spatial unknowns can be solved for sequentially along the two directions of flow via a standard sweeping procedure [22, 26]. Beginning at the left boundary, the positive unknowns can be determined for each cell from $i = 1, \dots, N_c$; because the inflow to the i -th cell is defined from the previous cell or boundary condition, a local system of equations can be solved for the $\langle \phi \rangle_{L,i}^+$ and $\langle \phi \rangle_{R,i}^+$ unknowns. The negative direction unknowns are determined similarly, starting from the right boundary towards the left. The newly computed half-range intensities can then be used to estimate the scattering source for the next iteration. This process is repeated until convergence.

The source iteration process can be written in operator notation as

$$\mathbf{M}\underline{\psi}^{l+1} = \frac{1}{2}\mathbf{S}\underline{\psi}^l + \underline{Q}, \quad (6.1)$$

where \mathbf{M} is the LO streaming and removal operator (i.e., the left-hand side of Eqs. (3.18)–(3.21) without the scattering terms included), $\underline{\psi}$ is a vector of the half-range FE moment unknowns, and the vector \underline{Q} contains the fixed source terms resulting from the linearized emission source and previous time step moments, for each equation. The source terms for the i -th element and the L equation, for both half-ranges, are

$$(\underline{Q})_{i,L}^{\pm} = \frac{\langle \phi \rangle_L^{\pm}}{c\Delta t} + \frac{1}{2}f_i\sigma_{a,i}ac\langle (T^n)^4 \rangle_{L,i} \quad (6.2)$$

The scattering operator terms for the i -th element and the L equations are

$$(\mathbf{S}\underline{\psi}^l)_{i,L}^{\pm} = (\sigma_{a,i}(1 - f_i) + \sigma_{s,i}) (\langle \phi^l \rangle_{i,L}^+ + \langle \phi^l \rangle_{i,L}^-). \quad (6.3)$$

Equivalent expressions are defined for the R moment equations and boundary conditions, forming a fully defined set of equations. The process of sweeping is denoted as \mathbf{M}^{-1} .

The scattering inversion must be performed within each Newton iteration. Thus, for the m -th Newton step, the source iteration process is defined as

1. Evaluate effective scattering and absorption cross sections with $\{T_i^m : i = 1, 2, \dots, N_c\}$.
2. Compute new scattering source $\frac{1}{2}\mathbf{S}\underline{\psi}^l$.
3. Perform sweeps to calculate $\underline{\psi}^{l+1} = \mathbf{M}^{-1}\mathbf{S}\underline{\psi}^l + \mathbf{M}^{-1}\underline{Q}$
4. If $\|\underline{\psi}^{l+1} - \underline{\psi}^l\|_2 < \text{tolerance } \|\underline{\psi}^{l+1}\|$, move to next Newton step.
5. Else: repeat steps 2–4.

6.2 Linear Diffusion Synthetic Acceleration

A form of DSA referred to as the WLA method is used to accelerate the source iterations [39, 38]. Between each sweep, an error equation for the scattering iterations is solved with an approximate angular discretization of the transport equation. The estimated error is used to correct the zeroth moment of the intensity unknowns. In operator notation, the DSA equations for a single iteration are

$$\mathbf{L}\psi^{l+1/2} = \frac{1}{2}\mathbf{S}\psi^l + Q \quad (6.4)$$

$$\mathbf{D}\delta\phi^{l+1/2} = \mathbf{S}(\underline{\psi}^{l+1/2} - \underline{\psi}^l) \quad (6.5)$$

$$\underline{\psi}^{l+1} = \underline{\psi}^{l+1/2} + \delta\phi^{l+1/2}, \quad (6.6)$$

where $\delta\phi$ represents the error in the mean intensity unknowns. The operator \mathbf{D} represents a diffusion-like approximation to the transport equation. The DSA equations contain a standard finite-difference diffusion discretization that can be more efficiently inverted than the S_2 -like equations that are being accelerated (particularly in higher spatial dimensions), but will accurately resolve the slowly-converging, diffusive error modes.

It is important for the spatial discretization of Eq. (6.5) to be closely related to the discretization of the LO equations for the acceleration to be effective and stable [1]. The WLA method first solves a spatially-continuous discretization of the diffusion equation for the error at faces $\{x_{i+1/2}\}$. The error on the faces is then mapped onto the volumetric moment unknowns via a LD discretization of the P_1 equations [39]. The LD mapping resolves issues that would occur in optically-thick cells, while the continuous diffusion equation is accurate in the EDL where acceleration is important [1].

The continuous diffusion equation and mapping equations for the WLA method are derived in Appendix B. To allow for the use of lumped or standard LD in the DSA equations, we introduce the factor θ , with $\theta = 1/3$ for standard LD, and $\theta = 1$ for lumped LD. The diffusion equation for the face at $x_{i+1/2}$ is

$$\begin{aligned} & \left(\frac{\sigma_{a,i+1}h_{i+1}}{4} (1 - \theta) - \frac{D_{i+1}}{h_{i+1}} \right) \delta\phi_{i+3/2} + \left(\frac{D_{i+1}}{h_{i+1}} + \frac{D_i}{h_i} + \left(\frac{1 + \theta}{2} \right) \left[\frac{\sigma_{a,i+1}h_{i+1}}{2} + \frac{\sigma_{a,i}h_i}{2} \right] \right) \delta\phi_{i+1/2} \\ & + \left(\frac{\sigma_{a,i}h_i}{4} (1 - \theta) - \frac{D_i}{h_i} \right) \delta\phi_{i-1/2} = \frac{h_{i+1}}{2} \langle q \rangle_{L,i+1} + \frac{h_i}{2} \langle q \rangle_{R,i} . \quad (6.7) \end{aligned}$$

The source in Eq. (B.9) is the residual for a given scattering iteration [20, 22]

$$\langle q \rangle_{L/R,i} = \sigma_{s,i} (\langle \phi^{l+1/2} \rangle_{L/R,i} - \langle \phi^l \rangle_{L/R,i}). \quad (6.8)$$

It is noted that there is no need to define the source differently for the lumped or standard LD DSA equations, because the source is in terms of moments.

The upwinding in the LO system exactly satisfies the inflow boundary conditions, therefore a vacuum boundary condition is applied to the diffusion error equations. Application of Eq. (B.10) gives the left boundary condition:

$$\left(\frac{1}{2} + \sigma_{a,1} h_1 \frac{1+\theta}{4} - \frac{D_1}{h_1} \right) \delta \phi_{1/2} + \left(\sigma_{a,1} h_1 \frac{1-\theta}{4} - \frac{D_1}{h_1} \right) \delta \phi_{3/2} = \frac{h_1}{2} \langle q \rangle_{L,1} \quad (6.9)$$

The boundary condition for the right-most face is

$$\left(\frac{1}{2} + \sigma_{a,I} h_I \frac{1+\theta}{4} - \frac{D_I}{h_I} \right) \delta \phi_{I+1/2} + \left(\sigma_{a,I} h_I \frac{1-\theta}{4} - \frac{D_I}{h_I} \right) \delta \phi_{I-1/2} = \frac{h_I}{2} \langle q \rangle_{R,I} \quad (6.10)$$

where I is the index of the last cell.

The system of equations formed from Eqs. (B.12), (6.10), and (B.9) can be solved directly with a banded matrix solver. Then, Eq. (B.23)–(B.26) are solved in each cell to map the face errors onto an LD representation over the interior. It is noted that unlike fully consistent DSA equations, the WLA-DSE algorithm does not preserve particle balance to round off. This is because the mapping procedure uses an approximate inflow to each cell, which is inconsistent with the partial outflows from adjacent cells. Thus, overall, our algorithm will only conserve energy to the order of scattering iteration convergence.

Because we are interested in the time-dependent solution, we need to accelerate the solution for the half-range intensities, rather than just the zeroth moment. We

do not accelerate the first moment of the angular intensity, as the solution for ΔJ is inaccurate due to the approximations introduced. The error in the half-range moments, using the lumping notation, are

$$\langle \delta\phi \rangle_L^\pm = \frac{1+\theta}{4}\delta\phi_L^\pm + \frac{1-\theta}{4}\delta\phi_R^\pm \quad (6.11)$$

$$\langle \delta\phi \rangle_R^\pm = \frac{1-\theta}{4}\delta\phi_L^\pm + \frac{1+\theta}{4}\delta\phi_R^\pm, \quad (6.12)$$

6.2.1 The WLA-DSA Accelerated Source Iteration Algorithm

We define the process of solving the diffusion like equations and mapping the error unknowns back onto the moment equations as the operator \mathbf{D}^{-1} . The source iteration with linear DSA procedure, for the m -th Newton iteration, is then defined as

1. Evaluate effective scattering and absorption cross sections with $\{T_i^m : i = 1, 2, \dots, N_c\}$.
2. Compute new scattering source $\mathbf{S}\psi^l$.
3. Perform sweeps to calculate $\psi^{l+1/2} = \mathbf{M}^{-1}\mathbf{S}\psi^l + \mathbf{M}^{-1}Q$
4. Perform DSA iteration to solve $\phi^{l+1} = \mathbf{D}^{-1}\sigma_s(\phi^{l+1/2} - \phi^l)$
 - Solve continuous DSA equations, i.e., Eq. (B.9) and Eq. (??), for $\{\delta\phi_{i+1/2}^{l+1/2} : i = 0, 1, \dots, N_c\}$.
 - Map the continuous error onto the moment unknowns, via Eq. (B.23)–(B.26).
5. Add correction to the moment unknowns, e.g., $\phi_L^{\pm, l+1} = \phi_L^{\pm, l+1/2} + \delta\phi^{l+1/2}/2$.
6. If $\|\psi^{l+1} - \psi^l\| < \text{tolerance}$, exit
7. Else: repeat steps 4–9.

6.3 GMRES Solution to the LO Equations

The source iteration procedure can be recast as an iterative solution to a matrix equation. Using operator notation, we manipulate the moment equations to form a matrix equation:

$$(\mathbf{I} - \mathbf{M}^{-1}\mathbf{S}) \psi = \mathbf{M}^{-1}Q, \quad (6.13)$$

where I is an identity matrix. The GMRES method is used to iteratively solve the above linear system. The GMRES is an iterative Krylov solution method for asymmetric, sparse matrix equations [30]. Krylov solutions to a linear system repeatedly apply the matrix operator to vectors, projecting the system onto a Krylov subspace [30]. Rather than forming the full matrix system, we apply the operation of \mathbf{S} and \mathbf{M}^{-1} as detailed in Sec. (6.1) to apply $(\mathbf{I} - \mathbf{M}^{-1}\mathbf{S})$ to the Krylov vectors.

The GMRES method will generally converge faster than the source iteration procedure [20]. However, as the system becomes scattering dominated, convergence will degrade. To improve the convergence rate, we precondition the GMRES system with the WLA-DSA method. The goal of preconditioning is to efficiently apply an operator to the equation that will approximate the inverse of the matrix operator. Left preconditioning [30] was applied to the above system. In matrix form, we write the preconditioned GMRES equations as

$$(\mathbf{I} + \mathbf{D}^{-1}\mathbf{S}) (\mathbf{I} - \mathbf{L}^{-1}\mathbf{S}) \psi = (\mathbf{I} + \mathbf{D}^{-1}\mathbf{S}) \mathbf{L}^{-1}Q. \quad (6.14)$$

The operation of $(\mathbf{I} + \mathbf{D}^{-1}\mathbf{S})^{-1}$ is equivalent to the DSA procedure, adding the correction to a Krylov vector.

The opensource library `mgmres` was modified to implement the matrix-free version of the GMRES procedure. The infrastructure from the source iteration with DSA

procedure is reused to provide the operation of $(\mathbf{I} + \mathbf{D}^{-1}\mathbf{S})(\mathbf{I} - \mathbf{M}^{-1}\mathbf{S})$ applied to the Krylov vectors returned from the GMRES solver. The preconditioned-GMRES algorithm is

1. Evaluate effective scattering and absorption cross sections with $\{T_i^m : i = 1, 2, \dots, N_c\}$.
2. Form initial source vector b by solving $b = \mathbf{M}^{-1}Q$
3. Apply left-preconditioner operator to b , so $b \leftarrow (\mathbf{I} + \mathbf{D}^{-1}\mathbf{S})\mathbf{M}^{-1}Q$
4. Compute new scattering source $\mathbf{S}\psi^l$.
5. Perform sweeps to calculate $\psi^{l+1/2} = \mathbf{M}^{-1}\mathbf{S}\psi^l + \mathbf{M}^{-1}Q$
6. Compute DSA residual source $\sigma_s(\phi^{l+1/2} - \phi^l)$
7. Solve continuous DSA equations (i.e., Eq. (B.9)) for $\{\delta\phi_{i+1/2}^{l+1/2} : i = 0, 1, \dots, N_c\}$
8. Map the continuous error onto the moment unknowns.
9. If $\|\psi^{l+1} - \psi^l\| < \text{tolerance}$, exit
10. Else: repeat steps 4-9.

The convergence tolerance is based on the residual. Without preconditioning, the diffusion solve is simply removed.

6.4 Computational Results

We have tested the iterative solution methods for three test problems and compare the average number of scattering iterations to converge. For each simulation, three batches of 10,000 particles are ran for each HO the single HO solve per time step, and 200 spatial cells were used. The average number of source iterations per Newton step is recorded, as well as the total number of Newton iterations per time step

(there are two LO solves per time step). The initial guess for the effective scattering source is set to zero at the beginning of each LO solve. All scattering iterations have a relative convergence of 10^{-10} . For all DSA simulations, we have used the lumped spatial representation for the DSA equations.

The first test problem is the two material problem in Sec 5.2. The time step is increased linearly by 15% each time step from $\Delta t = 0.001$ sh to reach a maximum time step size of 0.01 sh. The large time step sizes increases the magnitude of the effective scattering cross section. Table 6.1 compares iteration counts each method: unaccelerated source iteration (SI), source iteration with DSA (SI-DSA), unaccelerated GMRES (GMRES), and GMRES with DSA preconditioning (GMRES-DSA). As demonstrated, DSA improves the convergence of the source iteration method. The preconditioned GMRES was more efficient than standard GMRES.

The second test problem is a modification of the two material problem. The problem specifications are the same as before except for modifications to the cross sections for $x > 0.5$ cm; in the right half of the domain, the parameters are $\sigma_a = 20,000 \text{ cm}^{-1}$, $\sigma_s = 500 \text{ cm}^{-1}$. This problem is highly diffusive and nonlinear. The Newton method required damping with a damping factor of 0.6 to stably converge. Table 6.2 compares the iterations Overall, the damping increases the number of Newton steps, as expected. For this problem, acceleration is much more critical, reducing the number of scattering iterations by a factor of 100.

For the final test problem, we test the equilibrium diffusion limit problem from Sec. 5.6. The problem was tested with standard LD and lumping-equivalent LD spatial closures, with the DSA using the lumped representation in both cases. Table. 6.3 compares scattering iterations for the EDL problem. There was minimal degradation observed for the diffusion limit problem due to the difference in spatial discretizations. This is likely because both lumped LD and LD representations

produce accurate solutions in the EDL.

Table 6.1: Scattering source iterations for the two material problem. Simulation end time is 1 sh.

Method	Sweeps/Newton Iter.	Newton Iters./Time Step
SI	247.0	19.4
SI-DSA	10.1	19.3
GMRES	13.1	19.4
GMRES-DSA	7.7	19.3

Table 6.2: Scattering source iterations for the modified, diffusive two material problem. Simulation end time is 2 sh.

Method	Sweeps/Newton Step	Newton Iters./Time Step
SI	1037	25.2
SI-DSA	10.9	25.1
GMRES	11.6	25.1
GMRES-DSA	6.0	25.2

Table 6.3: Scattering source iterations for the equilibrium diffusion limit problem. Simulation end time is 3 sh.

LD LO Equations		
Method	Sweeps/Newton Step	Newton Steps/LO Solve
SI	357.4	8.4
SI-DSA	21.9	8.4
GMRES	36.5	8.4
GMRES-DSA	13.3	8.4
Lumped LO Equations		
SI	359.8	8.2
SI-DSA	14.6	8.2
GMRES	37.3	8.2
GMRES-DSA	9.8	8.2

7. Resolving Negative Intensities in Optically Thick Cells for ECMC

The linear-discontinuous (LD) spatial closure with upwinding is not strictly positive. In particular, for optically thick cells with a steep intensity gradient, the linear representation of the intensity can become negative at the edge of the cells. A common example in 1D is for the Marshak Wave problem where negative intensities in the representation occurs at the foot of the radiation wave front. These negativities are not physical and typically propagate to adjacent cells. In thick regions of TRT problems, reasonably fine spatial cells can still be on the order of millions of mean free paths; negativities with an LD representation are unavoidable in practice for such cells, and mesh refinement is of minimal use. The HO solver is prone to additional negativities near $\mu = 0$ where the intensity cannot be accurately represented by a linear projection in angle. These negativities near $\mu = 0$ can occur for modest optical thicknesses and in multiple adjacent cells. Because of the different solution methods for the HO and LO solvers, independent fixups have been developed for each. In the remainder of this chapter, we discuss the fixup method applied to the HO solver. Methods are then compared for statistical efficiency and accuracy for two test problems. We will explore several methods for resolving negativities. Ideally the solutions in such cells should be as consistent as possible for the HO and LO equations. However, the differences between the solution methods of the two equations, as well as the fact that the modifications made to one solver would be lagged in the next nonlinear LO solve, there is no guarantee of positivity, and thus independent fixups have been developed.

7.1 Artificial Source Method for Negativities in the HO Intensity

For the HO solver, in cells near the radiation wavefront, the LDFE trial space results in negative values in $\tilde{I}^{n+1}(x, \mu)$, similar to the LO solver. Because the residual formulation in ECMC allows for negative weight particles to occur, currently we do not treat these cells specially. We detect if the consistency terms lie in the appropriate half space at the end of the HO solve, an indication that the intensity was negative within that cell. If the terms are non-physical, then they are replaced with the corresponding S₂-equivalent value. In general, in such cells where the trial space cannot accurately represent the solution, error stagnation will rapidly occur.

The HO solver requires a different fixup approach for negative values of the intensity. At the end of any particular batch, a LDFE projection of the intensity $\tilde{I}(x, \mu)$ has been determined. This projection is based on a statistical estimate of the moments of the intensity, based on the truncated representation of sources. Although the statistically estimated moments are physically accurate, when these moments are projected onto a linear space the representation becomes negative, over some portion of certain elements' domains. The first moments can easily be modified to produce a positive representation \tilde{I}_{pos} . However, this modified solution will not satisfy the residual equation as accurately as the original solution, which leads to rapid error stagnation. Additionally, the next MC batch based on the residual source from \tilde{I}_{pos} will tend to produce negative cell averages in down stream cells.

Thus, we have devised a method to modify the transport equation such that \tilde{I}_{pos} will satisfy the residual equation more accurately. We do this in such a manner that the modified source will lead to the solution converging towards a solution with the same zeroth moment, but with a first moment in x and μ that are modified. This does not guarantee exponential convergence of the solution, because convergence is

still limited by the overall accuracy of the trial space and statistics within a batch. However, now the error will not stagnate as rapidly and the solution will converge towards the positive representation \tilde{I}_{pos} .

7.1.1 Calculating a Positive LDFE Representation

First, we define the procedure for obtaining \tilde{I}_{pos} . We produce a positive representation \tilde{I}_{pos} over a cell by scaling the first moment in x and μ uniformly. The process of modifying the first moments to produce a positive solution is under defined, so there is not a unique way to enforce positivity. This choice is not an emphasis of this research, so we apply the simple and efficient approach of scaling the slopes such that the ratio I_x/I_μ , for each modified cell, is unchanged. After an ECMC batch, we detect cells where the linear representation produces a value below the floor. The modified representation for the ij -th cell in such cells is

$$\tilde{I}_{\text{pos}} = I_a + C \left[\frac{2}{h_x} I_x (x - x_i) + \frac{2}{h_\mu} I_\mu (\mu - \mu_j) \right], \quad (x, \mu) \in \mathcal{D}_{ij}, \quad (7.1)$$

noting that the average has not been modified. The constant C is calculated as

$$C = \frac{I_a - I_{\min}}{|I_x| + |I_\mu|} \quad (7.2)$$

for values where $I_a > I_{\min}$, where I_{\min} is the isotropic intensity corresponding to equilibrium with the floor temperature. When I_a is below the floor, it is set to the floor value and I_x and I_μ set to zero. It is been noted that in application the difference between I_a and I_{\min} can be on the order of numerical roundoff for double precision variables.

7.1.2 Adding an Artificial Source

To mitigate stagnation and improve accuracy, we must now add an artificial source $\tilde{\delta}^{m+1}(x, \mu)$ to the HO transport equation. This source is estimated iteratively as

$$\tilde{\delta}(x, \mu)^{(m+1)} = \mathbf{L}(\tilde{I}^{n+1, (m)} - \tilde{I}_{\text{pos}}^{n+1, (m)}),$$

where $\tilde{I}_{\text{pos}}^{n+1}$ is the modified positive solution. The source $\tilde{\delta}$ is added to all later batches. If necessary, we can estimate a new source again in later batches where negative values occur once more. The residual for the modified transport problem will have the same residual magnitude as the original \tilde{I} , which will have lower magnitude than the modified solution which does not have the MC estimated first moments (this is only true for the first application of the modified source). Care must be taken to modify the source on the interior and exterior of the solution, particularly when the solutions in adjacent cells has been modified. The source $\tilde{\delta}$ lies in the same functional space as the residual and can thus use the existing code infrastructure to compute the source. This will also make this approach straight forward to extend to higher dimensions.

To provide insight into this choice of source, consider the modified transport problem that will be solved with ECMC, where the fixup has been applied at batch m :

$$\mathbf{L}I^{n+1} = q + \mathbf{L}(\tilde{I}^{n+1, (m)} - \tilde{I}_{\text{pos}}^{n+1, (m)}) \quad (7.3)$$

Application of \mathbf{L}^{-1} to both sides of the equation produces

$$I^{n+1} = \mathbf{L}^{-1}q + (\tilde{I}^{n+1, (m)} - \tilde{I}_{\text{pos}}^{n+1, (m)}). \quad (7.4)$$

Because \tilde{I} and \tilde{I}_{pos} have the same zeroth moment, we have not modified the zeroth

moment of the solution overall. Monte Carlo transport is used to estimate L^{-1} , thus we are estimating the solution to a transport problem that has a positive LDFE projection but preserves the zeroth moment of the original solution. The estimate of the modification to the first moments of the solution has statistical noise, and thus may under- or over-predict the necessary change in the solution. We make the conservative choice of preserving δ across batches, and modifying the source only when negative values occur again.

8. RESIDUAL MONTE CARLO TREATMENT OF THE TIME VARIABLE

Another extension and improvement for the HOLO method described in Sec. ?? is the time discretization of the transport equation. We have incorporated the time variable into the ECMC method to improve efficiency over IMC, while still preserving the accuracy of MC integration. The main area of interest is in producing more accurate resolution of radiation wave-fronts in optically thin regions, where particles transport a long distance over a time step. In such regions, the MC integration of the time variable by IMC can produce greater accuracy than an implicit Euler discretization, which can produce artificially fast propagation of radiation in space. A potential application where this accuracy is important is stellar atmosphere calculations. It is noted that no adaptive refinement in time is performed, so maintaining exponential convergence may not be possible. However, we still expect the residual MC formulation of the ECMC method to show improvement in efficiency over standard MC.

In the remainder of this chapter, the inclusion of the time variable into the ECMC trial space is detailed, along with modifications to particle tracking and the ECMC algorithm. The process of sampling, tracking, and tallies particle histories in time is detailed in literature[43, 11, 42, 32], but sufficient details are provided in this chapter. Finally, a new temporal closure for the LO equations is given, and results are compared to IMC for accuracy and efficiency.

8.1 Modifications to the HO equations

Inclusion of the time variable t in the trial space used by ECMC allows for no discretization of the transport operator \mathbf{L} . The transport operator, applied to the

continuous intensity I , becomes

$$\mathbf{L}I(x, \mu, t) = \frac{1}{c} \frac{\partial I}{\partial t} + \mu \frac{\partial I}{\partial x} + \sigma_t I \quad (8.1)$$

The emission source is still treated with an implicit Euler discretization, which is similar to the approximation made in IMC. The ECMC algorithm specified in Sec. ?? does not need to be modified. However, the residual source and trial-space representation are modified to include t . Each batch is still estimating the error in the current projection estimate $\tilde{I}(x, \mu, t)$, but the time variable must be included in the inversion of the \mathbf{L} operator.

8.1.1 The Doubly-Discontinuous Trial Space in Time

It is necessary to define a new trial space that includes the time variable so that we can explicitly evaluate the residual. The time variable has a similar representation to the LDD trial space used for the spatial variable in Sec. ??, but the solution is a constant value over the interior of the time step. This step, doubly-discontinuous (SDD) trial space is defined as

$$\tilde{I}(x, \mu, t) = \begin{cases} \tilde{I}^n(x, \mu) & t = t^n \\ \bar{I}(x, \mu) & t \in (t^n, t^{n+1}) \\ \tilde{I}^{n+1}(x, \mu) & t = t^{n+1} \end{cases} \quad (8.2)$$

where we have used \bar{I} to denote the time-averaged LDFE *projection* in x and μ of the intensity over the interior of the time step; the beginning and end of time step projections are denoted \tilde{I}^n and \tilde{I}^{n+1} , respectively. An illustration of t for the SDD trial space, over the n -th time step, is depicted in Fig. 8.1. There is a projection error in using the LDFE projection to represent the intensity between time steps. However,

with sufficient noise reduction and mesh resolution, this should be an acceptable error compared to the large statistical noise of standard MC.

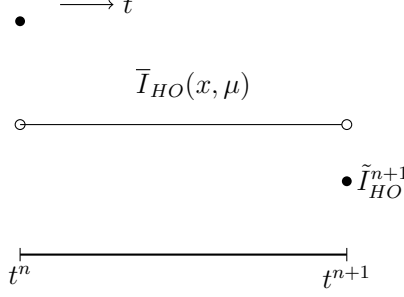


Figure 8.1: Step doubly-discontinuous representation of t for the HO solution.

The SDD trial space provides a projection for all the desired unknowns to exactly produce the moment equations, i.e., the time-averaged, end of time step, and previous time step intensities; temporally, these are the only unknowns that appear in equations that have been integrated over a time step to produce a balance statement. Another benefit of this trial space is it allows for infrastructure for computing the residual from the time-discrete case to be used directly. This trial space has one major drawback: only particle histories that reach t^{n+1} contribute to the estimation of $\tilde{\epsilon}^{n+1}$, and thus I^{n+1} . This is undesirable in optically thick problems.

REWRITE: Possibly move this to the future work section Alternatively, an LDFE representation could be used in the time variable. The linear representation should produce less noise because all particle tracks contribute to the slope, rather than just those that reach the end of the time step, although it would produce an approximate projection error for the end of time step intensity that is not produced with a discontinuity at the end of the time step. The linear representation in time would also

produce a more accurate reconstruction of the scattering source in time. However, a linear representation requires the sampling algorithm to be significantly modified because the L_1 integral for computing the residual magnitude is now significantly complicated by the tri-linear function. A possible way to sample this source is discussed in Appendix??? for completeness, but it has not been rigorously investigated.

8.1.2 Residual Source Definition and Sampling

The residual is defined as $r = q - \mathbf{L}\tilde{I}(x, \mu, t)$, where

$$q = (\sigma_{ac}(T_{LO}^{n+1})^4(x) + \sigma_s \bar{\phi}_{LO}) \quad (8.3)$$

is a constant in time and provided by the LO solver. We have assumed a constant reconstruction for the scattering source in time. Evaluation of the residual with Eq. (8.2) for I produces a uniform source in time, as well as a δ -function source at the beginning and end of the time step. We write the residual source in terms of three components:

$$r(x, \mu, t) = \bar{r}(x, \mu) + r^n(x, \mu)\delta^+(t - t^n) + r^{n+1}(x, \mu)\delta^-(t - t^{n+1}), \quad t \in [t^n, t^{n+1}] \quad (8.4)$$

We will look at each component individually. The first residual term is a constant in time with representation

$$\bar{r}(x, \mu) = q - \mu \frac{\partial \bar{I}(x, \mu)}{\partial x} - \sigma_t \bar{I}(x, \mu) \quad (8.5)$$

Evaluation of the above function produces both face and interior volumetric components (as in the time discrete case), respectively labeled \bar{r}_{face} and \bar{r}_{int} . To sample x and μ from the face and volume distributions, the same rejection procedure can be

used as for Eq. (??) and detailed in [29]. The time variable can then be sampled uniformly over the time step, i.e., $t = t^n + \eta \Delta t$, where η is a uniform random variable with support $(0, 1)$.

The second source has definition

$$r^n(x, \mu) = -\frac{1}{c} \frac{\partial \bar{I}(x, \mu)}{\partial t} \Big|_{t=t^n} = -\frac{1}{c} \left(\bar{I}(x, \mu) - \tilde{I}^n(x, \mu) \right) \quad (8.6)$$

This source is a LDFE space and angle volumetric source. The rejection sampling procedure is used to sample x and μ . All particles sampled from this source begin tracking with $t = t^n$.

The final source term is

$$r^{n+1}(x, \mu) = -\frac{1}{c} \frac{\partial \bar{I}(x, \mu)}{\partial t} \Big|_{t=t^{n+1}} = -\frac{1}{c} \left(\tilde{I}^{n+1}(x, \mu) - \bar{I}(x, \mu) \right). \quad (8.7)$$

The source r^{n+1} can be treated using the same analytic treatment as the outflow face source in the LDD trial space, as discussed in Sec. 4.5 and derived in App. A.3. The source at the end of the time step is never sampled, because its contribution to I^{n+1} can be analytically computed. To treat the sources this way, the solution for $\tilde{I}^{n+1}(x, \mu)$ is initialized to the value of $\bar{I}(x, \mu)$ before a batch of particles begins. Then, error particles that reach the end of the time step, referred to as “census” particles, contribute a standard score to the projection $\tilde{I}^{n+1}(x, \mu)$.

With these definitions, it is thus only necessary to sample from two sources. We apply the systematic-sampling algorithm described in Sec. 4.3. The number of histories sampled from each space-angle element is proportional to the magnitude of the residual within that cell, and a minimum number of histories is sampled from cells with a non-zero residual. Then, composite-rejection sampling is used to sampled

from the appropriate source. The algorithm for each sample, from $x - \mu$ element i , is

1. Sample two random numbers $\eta_1, \eta_2 \sim U(0, 1)$
2. If $\eta_1 < \|r_i^n\|_1 / (\|r_i^n\|_1 + \|\bar{r}_i\|_1)$:
 - Sample (x, μ) from r_i^n volumetric source using rejection sampling
 - Set $t = t^n$
3. Else, sample from \bar{r} source:
 - (a) Sample t uniformly over (t^n, t^{n+1}) .
 - (b) If $\eta_2 < \|\bar{r}_{i,\text{face}}\|_1 / \|\bar{r}_i\|_1$:
 - Sample (x, μ) from $\bar{r}_{i,\text{face}}$ face source using rejection
 - (c) Else:
 - Sample (x, μ) from $\bar{r}_{i,\text{int}}$ volumetric source using rejection

where all L_1 norms are over element i . All L_1 integrals can be analytically evaluated using the same numerics as in the time-discrete case because each residual component is either a volumetric or face component.

8.1.3 Importance Sampling on Interior of Time Step

As an attempt to reduce variance in the estimate of $\tilde{\epsilon}^{n+1}(x, \mu)$, we use important sampling in the time variable. Systematic sampling is still used for determining the cell of interest, and sampling as described above is used to determine which source is sampled, based on the appropriate probabilities described in the previous section. However, when the interior source $\bar{r}(x, \mu)$ is sampled, we use importance sampling for the conditional sampling of the uniform time step. The goal is to ensure that

some histories reach the end of the time step. In order to do this, we sample from a modified PDF such that a fraction p_{surv} of particles sampled from $\bar{r}(x, \mu)$ are born with $t \in (t^{surv}, t^{n+1})$. We define $t^{surv} = t^{n+1} - M/(c\sigma_t)$, where M is the desired number of MFP of travel the particle will undergo from the end of the time step (e.g., 2 or 3). The weights of particles sampled from this distribution must be modified to prevent biasing of the solution. This only affects Step 3a.

The new PDF to be sampled from is

$$f^*(t) = \begin{cases} \frac{1 - p_{surv}}{t^{surv} - t^n} & 0 < t < t^{surv} \\ \frac{p_{surv}}{t^{n+1} - t^{surv}} & t^{surv} \leq t < t^{n+1} \\ 0 & \text{elsewhere} \end{cases} \quad (8.8)$$

The original PDF is $f(t) = 1/\Delta t$, for $t \in (t^n, t^{n+1})$. Thus, using the standard procedure for importance sampling[31], the starting time t_{start} is sampled from $f^*(t)$, and then weights are multiplied by the factor $f(t_{\text{start}})/f^*(t_{\text{start}})$. This procedure is not perfect in that if a particle is moving from an optically thin to an optically thick region, it is not guaranteed to reach census. However, this case does not introduce bias.

8.1.4 Tracking and Tallying in Time

Because our LO equations will be integrated over the time step, we only need to perform MC tracking for $t \in [t^n, t^{n+1}]$. The initial time for the particle is sampled as described in the previous section. In inverting the \mathbf{L} operator, particles are tracked until they reach the end of the time step. Path lengths are sampled or the weight is exponentially attenuated as before (e.g., Sec. ??). As a particle travels from position

x_o to x_f , with direction μ , the time is updated as

$$t^f = t^0 + \frac{|x_f - x_o|}{c\mu} \quad (8.9)$$

where c is the speed of light. For analog path-length sampling, if $t^f > t^{n+1}$ then t^f is adjusted to t^{n+1} and the path length is adjusted accordingly. For continuous weight deposition, particles are only tracked until they reach t^{n+1} . A proof that this process of tracking particles is a MC solution to an integral equation that is exactly inverse to the \mathbf{L} operator is detailed in [32, ?].

Tallies must be adjusted to account for the averaging over the time step, and to compute the intensity at the end of time step. To produced the time-averaged representation $\bar{I}(x, \mu)$, requires estimators for the average, x , and μ moments of the error, e.g.,

$$\bar{\epsilon}_{x,ij} = \frac{1}{\Delta t} \frac{6}{h_j} \int_{t^n}^{t^{n+1}} dt \int_{x_{i-1/2}}^{x_{i+1/2}} dx \int_{\mu_{j-1/2}}^{\mu_{j+1/2}} d\mu \left(\frac{x - x_j}{h_i} \right) \epsilon(x, \mu, t) \quad (8.10)$$

with a similar definition for the average and μ moments. The estimators are defined as

$$\hat{\epsilon}_{x,ij} = \frac{1}{N_{hist}} \frac{6}{\Delta t h_i} \sum_{n=1}^{N_{hist}} \frac{s_n}{h_i h_j} w_j (x_c - x_i), \quad (8.11)$$

where the magnitude of the weights produce the L_1 integral over all phase space, i.e.,

$$\sum_{n=1}^N w_n = \|r(x, \mu, t)\|_1 \equiv \int_{t^n}^{t^{n+1}} dt \int_{x_{i-1/2}}^{x_{i+1/2}} dx \int_{\mu_{j-1/2}}^{\mu_{j+1/2}} d\mu |r(x, \mu, t)|. \quad (8.12)$$

Here, x_c is the center of the n -th path length, and s_n is the path length for the n -th path length in the $x - \mu$ cell.

Moments of $I^{n+1}(x, \mu)$ must be estimated to represent the end of time step in-

tensity. For example, the x moment for the ij -th cell of the error at the end of time step is

$$\epsilon_{x,ij}^{n+1} = \frac{6}{h_i} \iint_{\mathcal{D}_{ij}} \left(\frac{x - x_i}{h_i} \right) \epsilon(x, \mu, t^{n+1}) dx d\mu \quad (8.13)$$

The estimators for these moments are a generalization of the census tallies used in IMC [43, 42]. The tallies are based on the definition of the intensity as $I(x, \mu, t) = ch\nu N(x, \mu, t)$ given in Eq. (??), similar to collision estimators [31, 35]. The census estimator for the x moment is

$$\epsilon_{x,ij}^{n+1} = \frac{1}{N_{hist}} \frac{6}{h_j h_i} \sum_{n=1}^{N_{hist}} cw_j (x_c - x_i) \quad (8.14)$$

Similar tallies are defined for the other space-angle moments. These tallies can be exceptionally noisy because only particles that reach the end of the time step contribute.

8.2 Closing the LO Equations in Time

The LO equations must be closed in time consistently with the HO equations. Previous work has enforced consistency in time by adding a local artificial source to the time-discretized LO equations in each cell [45]. This source was approximated based on the difference between the exact HO integral of the time derivative and the approximate representation in the LO equations. The advantage of this form is that the LO solver exclusively deals in time-averaged unknowns for the radiation terms in the equations. However, if the problem is strongly non-linear or the time-averaged and time-edge values differ greatly, this may become unstable.

We will alternatively use a parametric closure in the time variable, similar to the spatial closures discussed in the Sec. ???. The time-integrated LO equations can be written exclusively in terms of time-averaged unknowns. This closure produces LO

equations that have the same numerical difficulty to solve as the BE, fully-discrete LO equations, but have the potential to preserve the accuracy of the MC integration in time, upon non-linear convergence of the system. A closure relation is used to eliminate the end of time step moments present from the time derivative term. We will investigate different parametric forms of the closure for robustness. Once the time-averaged unknowns have been calculated, the time closures can be used to convert the time-averaged unknowns to end-of-time-step values.

REWRITE THIS SENTENCE One potential benefit of the time closure parameters is that \bar{I}^{HO} will be most different from $I^{HO,n+1}$ in problems that are optically thin. In such problems, σ_a is small, leading to an optically thin problem. However, there may be difficulties in the MPV problems where the problems are tightly coupled and nonlinear, but can lead to a large change over a time step.

REWRITE: I think most of these paragraphs can be moved to intro

8.2.1 Derivation of Time-Averaged Moment Equations

The time-continuous radiation equations are integrated in space and angle the same as before. For example, the L and $+$ moment equation is

$$\begin{aligned} \frac{1}{c} \frac{\partial}{\partial t} \langle \phi \rangle_L^+ - 2 (\mu_{i-1/2} I_{i-1/2})^+ + \langle \mu I \rangle_{L,i}^+ + \langle \mu I \rangle_{R,i}^+ + \sigma_{t,i} h_i \langle \phi \rangle_{L,i}^+ - \frac{\sigma_{s,i} h_i}{2} (\langle \phi \rangle_{L,i}^+ + \langle \phi \rangle_{L,i}^-) \\ = \frac{h_i}{2} \langle \sigma_a a c T^4 \rangle_{L,i} \quad (8.15) \end{aligned}$$

This equation is then integrated over the time step, and the emission source is assumed implicit. The same manipulations can be performed on the streaming term to form angular consistency terms, but the weighting fluxes are now time-averaged values. Thus, the angular consistency terms are computed with $\bar{I}(x, \mu)$. The equations

with time-averaged consistency terms are

$$\begin{aligned} \frac{\langle \phi \rangle_{L,i}^{+,n+1} - \langle \phi \rangle_{L,i}^{+,n}}{c\Delta t} - 2\bar{\mu}_{i-1/2}^+ \bar{\phi}_{i-1/2}^+ + \overline{\{\mu\}}_{L,i}^+ \langle \bar{\phi} \rangle_{L,i}^+ + \overline{\{\mu\}}_{R,i}^+ \langle \bar{\phi} \rangle_{R,i}^+ + \sigma_{t,i}^{n+1} h_i \langle \bar{\phi} \rangle_{L,i}^{n+1,+} \\ - \frac{\sigma_{s,i} h_i}{2} (\langle \bar{\phi} \rangle_{L,i}^+ + \langle \bar{\phi} \rangle_{L,i}^-) = \frac{h_i}{2} \langle \sigma_a^{n+1} ac T^{n+1,4} \rangle_{L,i}, \quad (8.16) \end{aligned}$$

These equations are exact at this point. The BE approximation is used for the temperature terms in the material energy equations, but the radiation energy deposition is a time-averaged valued. REWRITE: Maybe add material energy equation

8.2.2 Parametric Time Closure

The closure relations in time are different than the closure relations for the spatial variable because we do not have a slope in time. The following closure is a modified diamond relation:

$$I^{n+1} = 2\gamma \bar{I} - I^n \quad (8.17)$$

where γ is the closure factor and \bar{I} is the time-averaged intensity. A modified BE discretization can also be used:

$$I^{n+1} = \gamma \bar{I} \quad (8.18)$$

The chosen closure relation must be used to eliminate the unknowns at t^{n+1} from each of the LO moment equations, with the values from the previous time step taken as a known quantity. Thus, it is necessary to have a closure relation for each moment and half range, producing four closure parameters per spatial cell. The closure relations for the L moment and the modified diamond relation are

$$\langle \phi \rangle_{L,i}^{\pm,n+1} = 2\gamma_{L,i}^{\pm} \langle \bar{\phi} \rangle_{L,i}^{\pm} - \langle \phi \rangle_{L,i}^{\pm,n} \quad (8.19)$$

with equivalent definitions for the R moment. Substitution of the above equation

into Eq. (8.16)

$$\begin{aligned} \frac{2}{c\Delta t} [\gamma_{L,i}^+ \langle \phi \rangle_L^{+,n+1} - \langle \phi \rangle_L^{+,n}] - 2\bar{\mu}_{i-1/2}^+ \bar{\phi}_{i-1/2}^+ + \{\bar{\mu}\}_{L,i}^+ \langle \bar{\phi} \rangle_{L,i}^+ + \{\bar{\mu}\}_{R,i}^+ \langle \bar{\phi} \rangle_{R,i}^+ + \sigma_{t,i}^{n+1} h_i \langle \bar{\phi} \rangle_{L,i}^+ \\ - \frac{\sigma_{s,i} h_i}{2} (\langle \bar{\phi} \rangle_{L,i}^+ + \langle \bar{\phi} \rangle_{L,i}^-) = \frac{h_i}{2} \langle \sigma_a^{n+1} acT^{n+1,4} \rangle_{L,i}, \quad (8.20) \end{aligned}$$

The other moment equations are analogously defined.

The value of $\gamma_{L,i}^+$, $\gamma_{R,i}^+$, $\gamma_{L,i}^-$, and $\gamma_{R,i}^-$ can be computed by substituting the trial-space representation of $I^{HO}(x, \mu, t)$ into Eq. (8.19) and its analogs.

8.3 Computational Results

We will test the HO time closure for several problems that characterize potential physics regime. Throughout this section, for the HOLO method, results that use the backward Euler discretization are indicated with HOLO-BE and the MC-based time closure are indicated with HOLO-TC, where applicable. For simplicity, all HOLO results have used the lumped-relation in the LO radiation moment equations to preserve positivity. We will compare sample statistics and accuracy against IMC simulations. The systematic sampling algorithms detailed in Sec. 4.3 and Sec. 8.1.2 were used for all HOLO results in this section. In the algorithm the average is set to the floor value and slopes to zero in such cells.

8.3.1 Near-Void Problem

For the first problem, the material properties are uniform throughout a 2.0 cm wide domain with $\rho c_v = 0.01374 \text{ Jks cm}^{-3} \text{ keV}^{-1}$, $\sigma_a = 10^{-6} \text{ cm}^{-1}$, and $\sigma_s = 0 \text{ cm}^{-1}$. The material and radiation are initially in equilibrium at a temperature of 0.01 keV. An isotropic incident intensity with $T_r = 0.150 \text{ keV}$ is applied at $x = 0$ for $t > 0$; the incident intensity on the right boundary is 0.01 keV. The simulation end time is 0.003 sh. Because the problem is optically thin, no importance sampling on the

interior of the time step is used. For this problem, we expect IMC to be accurate because the small cross section leads to the material energy equation being mostly uncoupled.

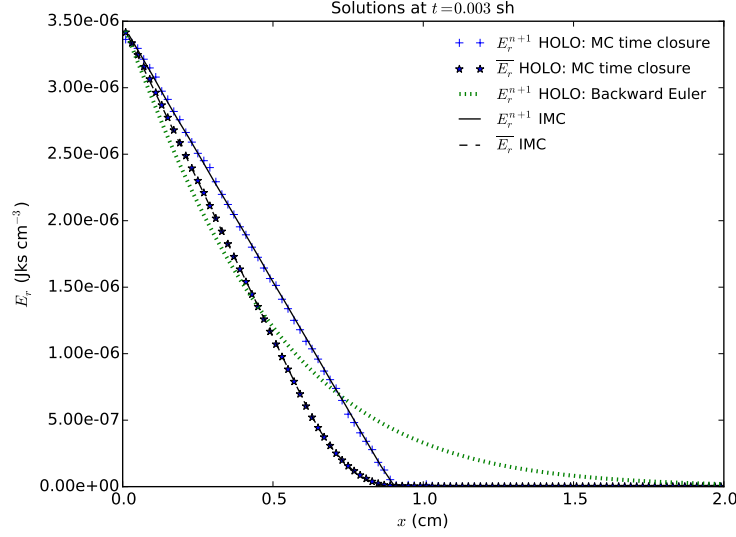


Figure 8.2: Comparison of radiation energy densities of IMC and HOLO method for the HO time closure and a BE discretization.

A comparison of the cell-averaged radiation energy densities E_r for IMC and the HOLO method with the diamond-like HO time closure are depicted in Fig. 8.2, both for the time-averaged solutions and end-of time step values, from the final time step. The end of time step value for the HOLO method with a BE discretization is also depicted. For the HOLO results, three ECMC batches were performed with a total of 3×10^6 histories per time step and the IMC results were generated with 12×10^6 histories per time step. The minimum number of histories for any sampled space-angle cell, N_{cut} in Eq. (??), is 20 for all HOLO simulations. The spatial meshes had 100 spatial cells and both HOLO results used 20 μ cells. The MC treatment of the

time variable and the closure of the LO equations allow the LO results to correctly reconstruct the wave-front location of IMC, whereas the BE discretization artificially propagates energy. Although not plotted, the results were visually equivalent for either the diamond-like or implicit-like closures in this problem. This is because the problem is nearly linear due to the small opacities, so the HO moments are reproduced accurately, independent of the chosen closure equation.

A comparison of similar results, but plotted as radiation temperatures, is plotted in Fig. ???. By plotting proportional to the fourth-root of the radiation energy density, the noise at low magnitudes past the wave-front are more apparent in the 3 batches and $\Delta t = 0.001$ case. This noise is small relative to the scale of E_r , but it demonstrates a deficiency of the trial space. The cause is from the step representation over the time step leading to particles sampled near the wave-front with a time near t^n that travel into the equilibrium region. It is noted this is not a bias, but rather an undersampling; if sufficient histories were performed there would be negative particles that canceled out this error. This effect is significantly reduced when a smaller time step is taken, although it increases the projection error between time steps.

For the case of a single batch, there is less noise past the wavefront because the choice of $I^n(x, \mu)$ and an initial guess for $I^{n+1}(x, \mu)$ prevents most particles from traveling past what the physical transport should allow. The discrepancy between the IMC and HOLO solution near the foot of the wave is a result of the spatial discrepancy between the LDFE HO projection and the lumped LD LO equations; this dispersion is not present in the HO solution. This discrepancy can also lead to some negativities in the LD representation of $\phi^{n+1}(x)$, which are set to the floor value for the next calculation.

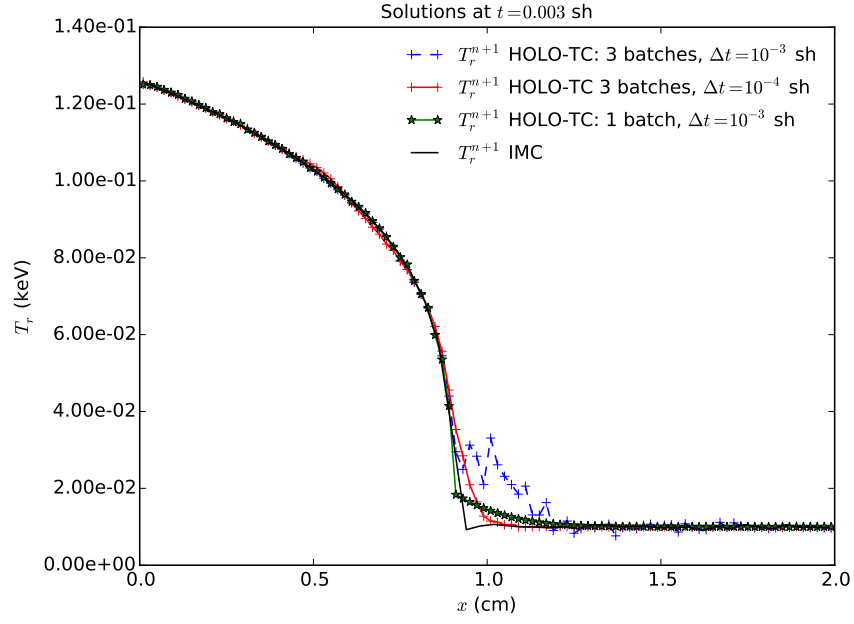


Figure 8.3: Comparison of radiation temperatures of IMC and the HOLO method for different time step sizes and numbers of batches, for the near-void problem.

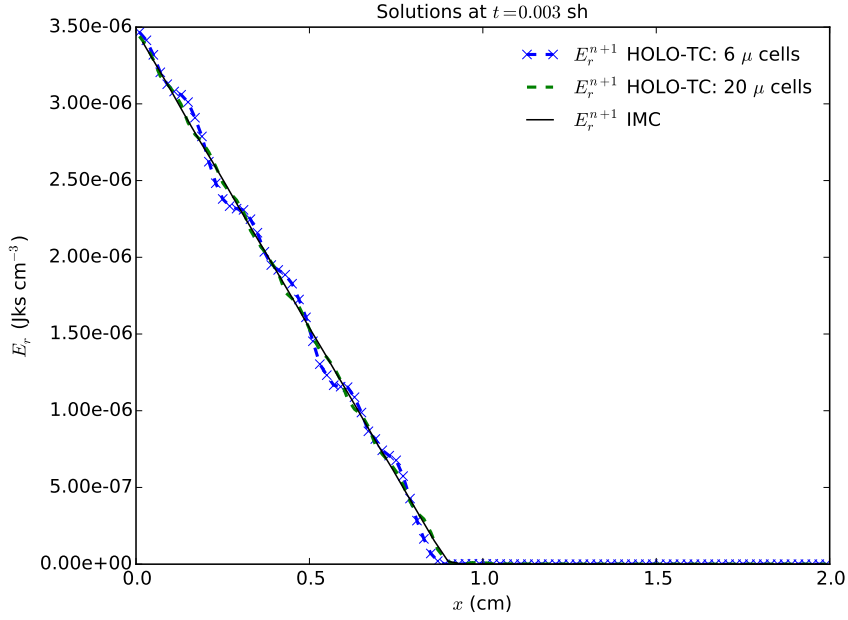


Figure 8.4: Comparison of radiation energy densities for the HOLO method with different numbers of μ cells. $\Delta t = 0.001$ sh, for near-void problem.

Figure. 8.4 compares radiation energy densities for various numbers of μ cells. At coarser mesh sizes, the imprinting of the mesh is visible in the location of the wave-front. This is a result of the projection onto the space-angle mesh between time steps. As the mesh is refined, the solution converges towards the IMC solution. Smaller time step sizes can increase the mesh imprinting because the projection onto the trial space happens more often. However, it is important to note that the mesh imprinting will be reduced as σ_a is increased and absorption-emission events smooth the angular intensity across each time step.

We have computed FOM statistics using Eq. (5.3) with 20 independent runs for each problem set up and parameters. The statistics are computed based on the time-averaged radiation energy densities. It is noted that the FOM results for each time step size are normalized to the IMC results within that table. The results

are compared for two different time step sizes in Tables 8.1 and 8.6. The different number of batches for the HOLO methods are indicated in parenthesis next to the method names. The results demonstrate that IMC can be more efficient than the ECMC method at longer time step sizes. This is a limiting case; because minimal absorptions are occurring in this problem, the IMC method is just advancing the initially sampled census particles between time steps, so there is negligible resampling of the phase space. Whereas, ECMC must resample the residual source and the step trial-space on the interior of the time step has a larger truncation error. At smaller time step sizes, the ECMC method, particularly for the single batch case, becomes more efficient than IMC.

Table 8.1: **Comparison of sample statistics for the time-averaged radiation energy densities, of the last time step, for the near-void problem and $\Delta t = 0.001$ sh. Simulation end time is $t = 0.003$ sh.**

	$\ s\ $			FOM		
hists./step	IMC	HOLO-TC (1)	HOLO-TC (3)	IMC	HOLO-TC(1)	HOLO-TC(3)
300,000	0.27%	0.27%	0.45%	1.00	0.96	0.35
3,000,000	0.09%	0.06%	0.15%	1.04	2.19	0.33

Table 8.2: **Comparison of sample statistics for the time-averaged radiation energy densities, of the last time step, for the near-void problem and $\Delta t = 10^{-4}$ sh. Simulation end time is $t = 0.003$ sh.**

	$\ s\ $			FOM		
hists./step	IMC	HOLO-TC (1)	HOLO-TC (3)	IMC	HOLO-TC(1)	HOLO-TC(3)
30,000	2.46%	0.44%	1.65%	1.00	31.07	2.22
300,000	0.80%	0.12%	0.37%	0.95	43.66	4.47

8.4 Optically Thin Problem

We modify the problem in the previous problem by increasing the absorption cross section to 0.2 cm^{-1} ; all other problem parameters are the same. Radiation temperatures at the end of the last time step are compared for IMC, HOLO-TC, and HOLO-BE in Fig. 8.5. The HOLO-TC and HOLO-BE results were generated with 30μ cells, and all spatial meshes used 200 cells. At smaller time step sizes, the effects of mesh imprinting are slightly apparent in the HOLO-TC results, leading to more dispersion near the wave-front. For $\Delta t = 0.005$ sh, there is good agreement between the HOLO-TC results and IMC. As in the previous problem, the HOLO-BE results do not accurately capture the wavefront location. IMC demonstrates substantial statistical noise in the equilibrium region.

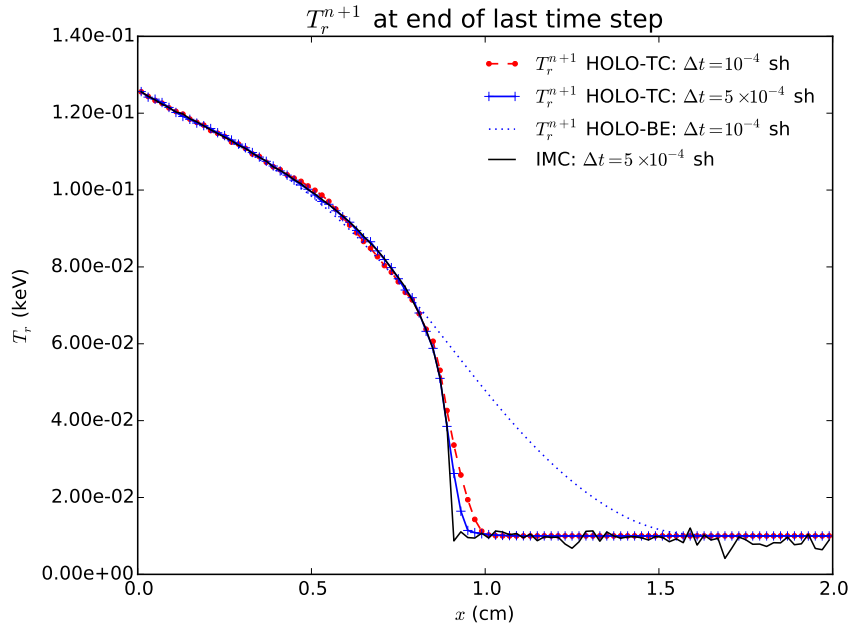


Figure 8.5: Comparison of radiation temperatures of IMC and the HOLO method for different time step sizes and numbers of batches, for optically thin problem.

Table. 8.3 compares computed FOM values for the census radiation energy densities, for the case of $\Delta t = 0.0005$ sh. HOLO results were generated for the case of 1 and 2 batches, with the same total number of histories per time step. At low particle counts for the larger time step size, the HOLO-TC method demonstrates substantial noise. This is due to the trial space representation of the census particles at the end of the time step being poorly estimated. For the 2 batch case, the estimate from the first batch leads to less error in the census estimate as the ECMC solves are simply solving for the deviation from the time-averaged quantity. The results for the case of 30,000 histories are plotted in Fig. ?? for the HO and LO solution. As demonstrated, there seems to have been some instabilities introduced into the LO equations through noise; sufficient sampling of the census must occur. At smaller time-steps there is an increase in statistical efficiency, however there has been a loss

in accuracy due to an increase in projection error. In general, this is a balance that much be considered.

The accuracy of the HOLO-ECMC method was compared to a reference solution from IMC. This problem is thin enough that we expect IMC to be accuracy with sufficient particle histories. The reference solution is the average of 20 IMC simulations of 20×10^6 histories, each with $\delta t = 10^{-4}$ sh. The estimated value of $\|s\|$ for the reference solution is 0.025%. The L_2 norm of the error in cell-averaged mean intensities is computed at the end of the last time step, was computed. The average over 20 simulations is then computed to provide the metric

$$\|e\|^l = \left(\frac{\sum_{i=1}^{N_c} \left(\phi_i^{n+1,l} - \phi_i^{n+1,ref} \right)^2}{\sum_{i=1}^{N_c} \left(\phi_i^{n+1,ref} \right)^2} \right)^{1/2}, \quad (8.21)$$

where $\phi_i^{n+1,l}$ is the cell-averaged scalar intensity at the end of the last time step from the l -th independent simulation. The sample mean of $\|e\|$ from 20 independent simulations provides a metric for the accuracy of a particular simulation:

$$\overline{\|e\|} = \frac{1}{20} \sum_{l=1}^{20} \|e\|^l \quad (8.22)$$

The accuracy results for

Table 8.3: Comparison of sample statistics for the end of time step radiation energy densities, of the last time step, for the optically thin problem and $\Delta t = 5 \times 10^{-4}$ sh. Simulation end time is $\mathbf{t} = \mathbf{0.003}$ sh.

	$\ s\ $			FOM		
hists./step	IMC	HOLO-TC (1)	HOLO-TC (3)	IMC	HOLO-TC(1)	HOLO-TC(3)
30,000	3.01%	18.29%	5.38%	1.00	0.03	0.31
300,000	0.99%	0.81%	0.74%	0.93	1.38	1.65
1,000,000	0.50%	0.30%	0.37%	1.10	3.42	2.0

Table 8.4: Comparison of sample statistics for the end of time step radiation energy densities, of the last time step, for the optically thin problem and $\Delta t = 1 \times 10^{-4}$ sh. Simulation end time is $\mathbf{t} = \mathbf{0.003}$ sh.

	$\ s\ $			FOM		
hists./step	IMC	HOLO-TC (1)	HOLO-TC (3)	IMC	HOLO-TC(1)	HOLO-TC(3)
30,000	3.00%	0.55%	1.28%	1.00	29.81	5.51
300,000	0.96%	0.11%	0.30%	0.98	71.82	9.88
1,000,000	0.49%	0.06%	0.17%	1.11	71.02	9.71

8.5 Marshak Wave Problem

It is important to demonstrate that the time closures are stable in a mix of optically thick and optically thin regions, and that the ECMC method is still efficient in such problems. Simulations were performed for the Marshak wave problem defined in Sec. ???. The time step size is linearly increased from 0.001 sh to a maximum step of 0.01 sh over the first 10 time steps; the last time step is adjusted to reach the desired

simulation end time. It was found for this problem that it was necessary to use more than one batch for the HOLO-TC algorithm to stably converge. This is because in the case of a single batch particles must reach census to accurately estimate the next time step value. These results were generated using the implicit-like time closure.

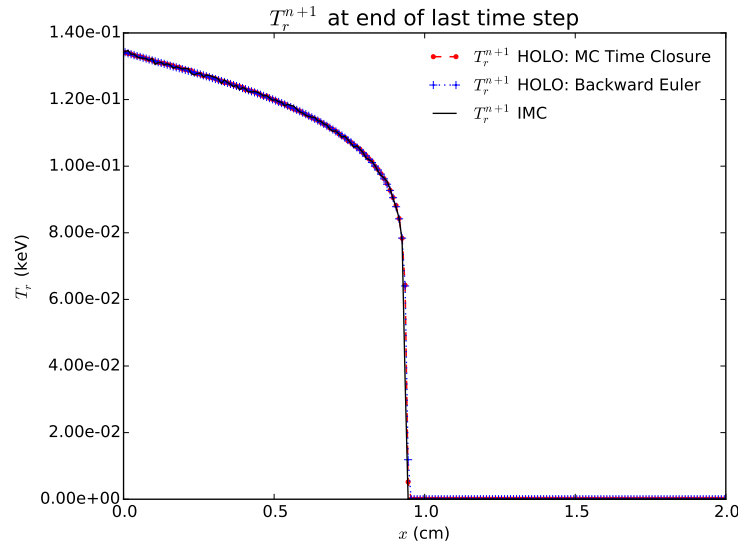


Figure 8.6: Comparison of HOLO-TC, HOLO-BE, and IMC methods for the Marshak Wave problem, with 10^6 histories per time step.

Figure 8.6 compares the accuracy of IMC, HOLO-TC, and HOLO-BE. The solutions are plotted at $t = 3$ sh, with 10^6 histories per time step for all simulations. As demonstrated, there is good agreement among the results. It is noted that this problem can be accurately modeled with the Backward Euler time discretization, but the MC time closure appears to be stable even in the mix of optically thick and thin regions. Table 8.5 compares sample statistics for IMC and the HOLO method with continuous time treatment and with a BE discretization. As demonstrated, at the lower history count (300,000), the HOLO-TC algorithm demonstrates a greater

variance. These results used the implicit like time closure.

Table 8.5: Comparison of sample statistics for the end of time step radiation energy densities, of the last time step, for the marshak wave problem and maximum time step of 0.01 sh. Simulation end time is $t = 3.0$ sh.

	$\ s\ $			FOM		
hists./step	IMC	HOLO-TC (2)	HOLO-BE (2)	IMC	HOLO-TC (2)	HOLO-BE (2)
300,000	2.25%	3.42%	0.30%	1.00	0.43	2050
1,000,000	1.27%	0.31%	0.17%	0.94	15.95	1806
Diamond Like Closure						
300,000	—	3.53%	—	—	0.41	—
1,000,000	—	0.37%	—	—	10.94	—

The importance sampling algorithm detailed in Sec. 8.1.3 was investigated for this problem set up. In particular, various values of p_{surv} with a fixed value of 2 mfp of survival distance were investigated. Sample statistics were measured for the HOLO-TC algorithm and the case of two batches of 100,000 histories per time step, with a max time step of 0.01 sh. The importance sampling algorithm was found to generally increase the variance, for this problem. This is likely caused by the fact that when no importance sampling is used, in the very thick cells essentially no particles reach the census. In such cells, because the ECMC algorithm is estimating the difference between the first batch's estimate of $\bar{I}(x, \mu)$ and $\tilde{I}^{n+1}(x, \mu)$, it just accepts $\bar{I}(x, \mu)$ as $I^{n+1}(x, \mu)$. The initialization of the solution to the first batches estimate of $\bar{I}(x, \mu)$ is sufficient to produce visually accurate results because the waves are moving so slowly. When importance sampling is used, There is likely a regime

of problems where it is necessary to sample the census more thoroughly and the importance sampling may reduce variance.

Table 8.6: Comparison of sample statistics using importance sampling on the interior of the time step, for the Marshak Wave problem. Simulation end time is $\mathbf{t} = \mathbf{1.0}$ sh. and max Δt is 0.01 sh

p_{surv}	FOM
No Bias	1
0.05	0.001
0.1	0.005
0.25	0.179
0.5	0.003

9. CONCLUSIONS AND FUTURE WORK

9.1 CONCLUSIONS

We have been able to produce solutions for Marshak wave test problems using a new HOLO method that are in agreement with IMC. Unlike IMC, our method requires no effective scattering events to be included in the MC simulation, which limits the run time of particle tracking, while adding the cost of a LO newton solver. Average LO iteration counts did not significantly increase as the time step size was increased. The LDFE spatial representation mitigates issues with teleportation error, producing results with spatial accuracy comparable to IMC with source tilting. The ECMC approach, with initial guesses based on the previous radiation intensity, results in efficient reduction of statistical error and allows for particles to be distributed to largely varying regions of the problem. The LO solver resolves the non-linearities in the equations resulting in a fully implicit time discretization. The LO solver can accurately and efficiently resolve the solution in diffusive regions, while the HO transport solver provides the accuracy of a full transport treatment where necessary.

The primary difficulty to overcome in the ECMC algorithm is when the solution cannot be accurately represented by the trial space, e.g., in optically thick cells where the solution is driven negative. We are currently developing an approach to allow the ECMC iterations to continue converging globally when there are such regions present. It is necessary to ensure the closure in the LO system is consistent with the HO representation for the solution in such regions. The ability to represent the solution accurately in rapidly varying regions of the problem will be key for generalization of this method to higher dimensions. A formulation of the ECMC method that

allows for time-continuous MC transport (similar to IMC) is also currently being investigated. This may reduce some of the loss of accuracy in optically thin regions due to the time discretization of the transport equation in the HO solver. However, greater time accuracy is not of primary concern as this method is intended for use in problems dominated by large absorption opacities, where the LO acceleration is critical. Inclusion of Compton scattering in this algorithm, which would introduce additional non-linear dependence through energy exchange with the material, is a topic for future research.

Future work will also explore the accuracy of the HOLO method, in particular, analyzing the optimal number of batches and the benefit of adaptive refinement. This will likely require the use of manufactured solutions. The sensitivity of the method to mesh sizes and time step sizes will be investigated more thoroughly. Ultimately, we plan to extend this method to multiple spatial dimensions for the case of multigroup TRT equations. For TRT problems, it is important that the LO spatial discretization satisfies the equilibrium diffusion limit. To extend to higher dimensions, our LDFF representation may require the use of a higher-degree spatial representation for the LO system to achieve the diffusion limit. Further asymptotic analysis on the method will be applied before implementation. It may be necessary to use a different LO system (e.g., the non-linear diffusion acceleration approach in [41]), if the S_2 -like equations become too inefficient or difficult to implement in higher dimensions. Alternatively, a variable Eddington Tensor approach may provide more stability in rapidly variable regions of the problem while still allowing for a consistent, LDFF solution that is efficiently solvable.

The advantage of the HOLO method is that there is no additional cost for the HO solution when the damped method is used.

Poor statistics for the face tallies may result in this trial space producing less

accurate results compared to the standard LDFE solution, at least for sufficiently fine meshes where LD can accurately represent the solution. Although the closure will be applied everywhere, we expect the greatest improvement in accuracy for cells where the LDFE trial space produces a negative solution.

ACKNOWLEDGEMENTS

This research was supported with funding received from the DOE Office of Nuclear Energy’s Nuclear Energy University Programs, the DOE National Nuclear Security Administration, under Award Number(s) DE-NA0002376, and under Los Alamos National Security, LLC, for the National Nuclear Security Administration of the U.S. Department of Energy under contract DE-AC52-06NA25396.

9.2 Future Work

SPATIAL CLOSURE: Additionally, because these closure parameters are modifications to standard spatial closures, it should be possible to filter bad values of γ_i^{HO} . Future studies will investigate the stability of this method more rigorously using a linear fourier stability analysis.

REFERENCES

- [1] Marvin Adams and William Martin. Diffusion synthetic acceleration of discontinuous finite element transport iterations. *Nuclear Science and Engineering*, 111(2):145–167, 1992.
- [2] S.R. Bolding, M. Cleveland, and J.E. Morel. A High-Order Low-Order Algorithm with Exponentially-Convergent Monte Carlo for Thermal Radiative Transfer. *Nuclear Science & Engineering: M&C 2015 Special Issue*, Jan. 2017. Forthcoming.
- [3] S.R. Bolding and J.E. Morel. A High-Order Low-Order Algorithm with Exponentially-Convergent Monte Carlo for k -Eigenvalue problems. ANS Winter Meeting. Anaheim, CA, 2014.
- [4] Subrahmanyam Chandrasekhar. *Radiative Transfer*. Courier Corporation, 2013.
- [5] Jeffery D. Densmore. Asymptotic analysis of the spatial discretization of radiation absorption and re-emission in implicit monte carlo. *Journal of Computational Physics*, 230(4):1116 – 1133, 2011.
- [6] Jeffery D Densmore, Kelly G Thompson, and Todd J Urbatsch. A hybrid transport-diffusion monte carlo method for frequency-dependent radiative-transfer simulations. *Journal of Computational Physics*, 231(20):6924–6934, 2012.
- [7] Paul Nelson Edward W. Larsen. Finite-difference approximations and super-convergence for the discrete-ordinate equations in slab geometry. *SIAM Journal on Numerical Analysis*, 19(2):334–348, 1982.

- [8] Edward W. Larsen and Jim E. Morel. Advances in discrete-ordinates methodology. *Nuclear Computational Science. Springer Netherlands*, pages 1–84, 2010.
- [9] Jeffrey A Favorite, Ashley D Thomas, and Thomas E Booth. On the accuracy of a common monte carlo surface flux grazing approximation. *Nuclear Science and Engineering*, 168(2):115–127, 2011.
- [10] Jim Michael Ferguson. *Asymptotic accuracy of the equilibrium diffusion approximation and semi-analytic solutions of radiating shocks*. PhD thesis, Texas A&M University, 2014.
- [11] J. A. Fleck, Jr. and J. D. Cummings, Jr. An implicit monte carlo scheme for calculating time and frequency dependent nonlinear radiation transport. *J. Comput. Phys.*, 8(3):313–342, December 1971.
- [12] N. A. Gentile and Ben C. Yee. Iterative implicit monte carlo. *Journal of Computational and Theoretical Transport*, 0(0):1–31, 0.
- [13] N.A. Gentile. Implicit monte carlo diffusion: An acceleration method for monte carlo time-dependent radiative transfer simulations. *Journal of Computational Physics*, 172(2):543–571, 2001.
- [14] Eugene D. Brooks III, Michael Scott McKinley, Frank Daffin, and Abraham Szke. Symbolic implicit monte carlo radiation transport in the difference formulation: a piecewise constant discretization. *Journal of Computational Physics*, 205(2):737 – 754, 2005.
- [15] Eugene D. Brooks III, Abraham Szke, and Jayson D.L. Peterson. “piecewise linear discretization of symbolic implicit monte carlo radiation transport in the difference formulation ”. *“Journal of Computational Physics ”*, ”220”(1):471 – 497, 2006.

- [16] Samet Y Kadioglu, Dana A Knoll, Robert B Lowrie, and Rick M Rauenzahn. A second order self-consistent imex method for radiation hydrodynamics. *Journal of Computational Physics*, 229(22):8313–8332, 2010.
- [17] CT Kelley. Iterative methods for linear and nonlinear equations. *SIAM*, 65002, 1995.
- [18] Rong Kong and Jerome Spanier. A new proof of geometric convergence for general transport problems based on sequential correlated sampling methods. *Journal of Computational Physics*, 227:9762 – 9777, 2008.
- [19] Edward W. Larsen, Akansha Kumar, and Jim E. Morel. Properties of the implicitly time-differenced equations of thermal radiation transport. *J. Comput. Phys.*, 238:82–96, April 2013.
- [20] Edward W Larsen and Jim E Morel. Advances in discrete-ordinates methodology. In *Nuclear Computational Science*, pages 1–84. Springer, 2010.
- [21] EW Larsen, GC Pomraning, and VC Badham. Asymptotic analysis of radiative transfer problems. *Journal of Quantitative Spectroscopy and Radiative Transfer*, 29(4):285–310, 1983.
- [22] Elmer Eugene Lewis and Warren F Miller. *Computational methods of neutron transport*. John Wiley and Sons, Inc., New York, NY, 1984.
- [23] Ryan McClarren. Numerical methods in reactor analysis. Class Lecture Notes, 2015.
- [24] Michael Scott McKinley, Eugene D Brooks III, and Abraham Szoke. Comparison of implicit and symbolic implicit monte carlo line transport with frequency weight vector extension. *Journal of Computational Physics*, 189(1):330–349, 2003.

- [25] Dimitri Mihalas and Barbara Weibel-Mihalas. *Foundations of radiation hydrodynamics*. Courier Corporation, 1999.
- [26] J.E. Morel, T.A. Wareing, and K. Smith. Linear-Discontinuous Spatial Differencing Scheme for S_n Radiative Transfer Calculations. *Journal of Computational Physics*, 128:445–462, 1996.
- [27] Jim Morel. Neutron transport theory. Class Lecture Notes, 2014.
- [28] H. Park, J.D. Densmore, A.B. Wollaber, D.A. Knoll, and R.M. Ramenzahn. Monte Carlo Solution Methods in a Moment-Based Scale-Bridging Algorithm For Thermal Radiative Transfer Problems. M&C. Sun Valley, ID, 2013.
- [29] J.R. Peterson. Exponentially Convergent Monte Carlo for the 1-d Transport Equation. Master’s thesis, Texas A&M, 2014.
- [30] Yousef Saad. *Iterative methods for sparse linear systems*. Siam, 2003.
- [31] J.K. Shultis and W.L. Dunn. *Exploring Monte Carlo Methods*. Academic Press, Burlington, MA 01803, 2012.
- [32] Clell J Solomon. *Discrete-ordinates cost optimization of weight-dependent variance reduction techniques for Monte Carlo neutral particle transport*. PhD thesis, Kansas State University, 2010.
- [33] Weston M. Stacey. *Nuclear Reactor Physics*. Wiley, 2007.
- [34] James M Stone and Michael L Norman. Zeus-2d: A radiation magnetohydrodynamics code for astrophysical flows in two space dimensions. i-the hydrodynamic algorithms and tests. *The Astrophysical Journal Supplement Series*, 80:753–790, 1992.
- [35] X-3 Monte Carlo Team. *MCNP - A General N-Particle Transport Code, Version 6: Volume I, Overview and Theory*, 2005. LA-UR-03-1987.

- [36] E.F. Toro. *Riemann Solvers and Numerical Methods for Fluid Dynamics: A Practical Introduction*. Springer, 1999.
- [37] T.J. Urbatsch and T.M. Evans. Milagro Version 2 An Implicit Monte Carlo Code for Thermal Radiative Transfer: Capabilities, Development, and Usage. Los Alamos National Laboratory Report LA-14195-MS, 2006.
- [38] T.A. Wareing. *Asymptotic diffusion accelerated discontinuous finite element methods for transport problems*. PhD thesis, Michigan, 1991.
- [39] T.A. Wareing, E.W. Larsen, and M.L. Adams. Asymptotic Diffusion Accelerated Discontinuous Finite Element Schemes for the S_N Equations in Slab and X-Y Geometries. In *International Topical Meeting on Advances in Mathematics, Computations, Reactor Physics*, volume 3, Pittsburgh, PA, 1991.
- [40] J. Willert, C.T. Kelly, D.A. Knoll, and H. Park. A Hybrid Approach to the Neutron Transport k-Eigenvalue Problem using NDA-based Algorithms. M&C. Sun Valley, ID, 2013.
- [41] Jeffrey Willert and H. Park. Residual monte carlo high-order solver for moment-based accelerated thermal radiative transfer equations. *Journal of Computational Physics*, 276:405 – 421, 2014.
- [42] Allan B Wollaber. *Advanced Monte Carlo methods for thermal radiation transport*. PhD thesis, The University of Michigan, 2008.
- [43] Allan B Wollaber. Four decades of implicit monte carlo. *Journal of Computational and Theoretical Transport*, 45(1-2):1–70, 2016.
- [44] Allan B Wollaber, Edward W Larsen, and Jeffery D Densmore. A discrete maximum principle for the implicit monte carlo equations. *Nuclear Science and Engineering*, 173(3):259–275, 2013.

- [45] Allan B. Wollaber, H. Park, R.B. Lowrie, R.M. Rauenzahn, and M.E. Cleveland. Radiation hydrodynamics with a high-order, low-order method. In *ANS Topical Meeting, International Topical Meeting on Mathematics and Computation*, Nashville Tennessee, 2015.
- [46] Ryan T Wollaeger, Allan B Wollaber, Todd J Urbatsch, and Jeffery D Densmore. Implicit monte carlo with a linear discontinuous finite element material solution and piecewise non-constant opacity. *Journal of Computational and Theoretical Transport*, pages 00–00, 2016.
- [47] E.R. Wolters. *Hybrid Monte Carlo - Deterministic Neutron Transport Methods Using Nonlinear Functionals*. PhD thesis, Michigan, 2011.

APPENDIX A

DERIVATIONS AND EQUATIONS FOR THE LO SYSTEM

A.1 Useful Moment Relations for LO Equations

There are several relations between various moment definitions that are useful in derivation and manipulation of the LO equations. The following are derived for $\phi(x)$, but can be applied to general moments of functions. The volumetric average terms can be eliminated in terms of the L and R moments from the relation $b_{L,i}(x) + b_{R,i}(x) = 1$.

$$\phi_i = \frac{1}{h_i} \int_{x_{i-1/2}}^{x_{i+1/2}} \phi(x) dx \quad (\text{A.1})$$

$$= \frac{1}{h_i} \left(\int_{x_{i-1/2}}^{x_{i+1/2}} b_{L,i}(x) \phi(x) dx + \int_{x_{i-1/2}}^{x_{i+1/2}} b_{R,i}(x) \phi(x) dx \right) \quad (\text{A.2})$$

$$= \frac{1}{2} (\langle \phi \rangle_{L,i} + \langle \phi \rangle_{R,i}) \quad (\text{A.3})$$

A similar relation can be derived for the first moment in space as

$$\phi_{x,i} = \frac{3}{2} (\langle \phi \rangle_{R,i} - \langle \phi \rangle_{L,i}) \quad (\text{A.4})$$

The above relations can be inverted to derived a relation for the L and R moments in terms of the slope and average moments. These moment expressions are defined purely in terms of integrals, and are independent of the chosen spatial representation

Once a linear relation on the interior has been assumed, there are other useful closures that can be derived. The standard linear interpolatory expansion, for the

positive half-range, is restated here:

$$\phi^+(x) = \phi_{L,i}^+ b_{L,i}(x) + \phi_{R,i}^+ b_{R,i}(x) \quad (\text{A.5})$$

Using this expansion, one can derive a relation between the outflow from a cell and the hat function moments that is equivalent to the standard LDFE Galerkin method:

$$\phi_{i,R}^+ = 2\langle\phi\rangle_{R,i}^+ - \langle\phi\rangle_{L,i}^+, \quad (\text{A.6})$$

where for standard LD $\phi_{i+1/2}^+ \equiv \phi_{i,R}^+$. The assumption of a linear relation on the interior of the cell defines the value for $\phi_{i,L}^+$:

$$\phi_{i,L}^+ = 2\langle\phi\rangle_{L,i}^+ - \langle\phi\rangle_{R,i}^+, \quad (\text{A.7})$$

To eliminate the LO unknowns in a manner that produces the same moments as the LDFE Galerkin method, the following expression can be used for the outflow from a cell

$$\phi_{i+1/2}^+ = \phi_i^+ + \frac{\phi_{x,i}^+}{3}, \quad (\text{A.8})$$

which in terms of the hat function moments is equivalent to $\phi_{i+1/2}^+ = \langle\phi\rangle_{R,i}^+$. Inserting this expression into Eq. (??), and using the same definition for the linear representation over the interior of $\phi_{i+1/2}^+(x) = \phi_{L,i}^+ b_{L,i}(x) + \phi_{R,i}^+ b_{R,i}(x)$, will produce an equivalent set of unknowns as a linear discontinuous method with a lumped representation for the radiation. The temperature equation must be independently lumped. This relation preserves the average within a cell but modifies the first moment.

A similar expression produces a lumped-equivalent representation on the interior

of the cell:

$$\phi_{i,R}^+ = \phi_i^+ + \frac{\phi_x^+}{3}, \quad (\text{A.9})$$

The moment equations are not modified by using this expression, however the interpretation of the moments as a linear representation over the cell has been altered. This allows for us to ensure a lumped representation on the interior while still using the HO solution to eliminate the outflow from the equations.

A.2 Newtons Method for the LO Equations

This section briefly derives the equations for the Newton's method solution to the nonlinear LO equations, with the LDFE representation of the temperatures, based on the approach in [26]. Because we have only considered problems with constant densities and heat capacities, the linearization described below is in terms of temperature T rather than material internal energy, for simplicity. However, the linearization can be formed in terms of internal energy to apply this method to a general equation of state.

To formulate the linear equations for each Newton step, the Planckian source is linearized in the material and radiation equations (Eq. (2.2) & Eq. (2.1)). Application of the first order Taylor expansion in time to the implicit emission source $\sigma_a ac(T^{n+1})^4$, about some temperature T^* at some time $t^* \in [t^n, t^{n+1}]$, yields

$$\sigma_a^{n+1} ac T^{4,n+1} \simeq \sigma_a^* ac [T^{*4} + (T^{n+1} - T^*) 4T^{*3}] \quad (\text{A.10})$$

where $\sigma_a^* \equiv \sigma_a(T^*)$. Substitution of this expression into Eq. (2.2) yields

$$\rho c_v \left(\frac{T^{n+1} - T^n}{\Delta t} \right) = \sigma_a^* \phi^{n+1} - \sigma_a^* ac [T^{*4} + (T^{n+1} - T^*) 4T^{*3}]. \quad (\text{A.11})$$

Algebraic manipulation of this equation yields an expression for $T^{n+1} - T^*$:

$$(T^{n+1} - T^*) = \frac{\frac{\sigma_a^* \Delta t}{\rho c_v} [\phi^{n+1} - acT^{*4}] + (T^n - T^*)}{1 + \sigma_a^* ac \Delta t \frac{4T^{*3}}{\rho c_v}}.$$

This expression is substituted back into Eq. (A.10) to form an explicit approximation for the emission source at t^{n+1} as

$$\sigma_a ac T^{4,n+1} \simeq \sigma_a^* (1 - f^*) \phi^{n+1} + f^* \sigma_a^* ac T^{4,n} + \rho c_v \frac{1 - f^*}{\Delta t} (T^n - T^*) \quad (\text{A.12})$$

where $f^* = [1 + \sigma_a^* c \Delta t 4a T^{*3} / (\rho c_v)]^{-1}$ is often referred to as the Fleck factor [11].

Next, the above equation is spatially discretized. Application of the L spatial moment yields

$$\begin{aligned} \langle \sigma_a^* ac T^{4,n+1} \rangle_{L,i} &= \sigma_{ai}^* (1 - f_i^*) \langle \phi^{n+1} \rangle_{L,i} + f_i^* \sigma_{ai}^* ac \left(\frac{2}{3} T_{L,i}^{4,n} + \frac{1}{3} T_{R,i}^{4,n} \right) \\ &\quad \rho_i c_{vi} \frac{1 - f_i^*}{\Delta t} \left[\frac{2}{3} (T_{L,i}^n - T_{L,i}^*) + \frac{1}{3} (T_{R,i}^n - T_{R,i}^*) \right], \quad (\text{A.13}) \end{aligned}$$

where $T^{4,n}$ and T^n have been assumed LD and f^* is assumed constant over a cell, i.e., $f_i^* \equiv f(T_i^*)$. The error introduced by a constant f^* approaches zero as the non-linearity is converged because T^* approaches T^{n+1} . Based on an estimate for T^* , Eq. (A.13) is an expression for the Planckian emission source in the radiation moment equations with an additional effective scattering source. A similar expression can be derived for $\langle \sigma_{a,i} ac T^4 \rangle_R$ and the right moment equations. The expressions for the emissions source is substituted into the discrete radiation moment equations, (Eq. (??)– (3.21)) to produce a linear system of equations for the new radiation intensity moments (upon closure of the moment equations).

Once the linear equations have been solved for new radiation moments, new temperature unknowns can be estimated. To conserve energy, the same linearization and discretizations used to solve the radiation equation must be used in the material energy equation. Substitution of Eq. (A.13) into the material energy L moment equation, i.e., Eq. (3.22), ultimately yields

$$\begin{aligned} \frac{2}{3}T_{L,i}^{n+1} + \frac{1}{3}T_{R,i}^{n+1} = \frac{f_i^* \sigma_{ai}^* \Delta t}{\rho c_v} \left[\langle \phi^{n+1} \rangle_{L,i} - ac \left(\frac{2}{3}T_{L,i}^{4,n} + \frac{1}{3}T_{R,i}^{4,n} \right) \right] + \\ (1 - f_i^*) \left(\frac{2}{3}T_{L,i}^* + \frac{1}{3}T_{R,i}^* \right) + f \left(\frac{2}{3}T_{L,i}^n + \frac{1}{3}T_{R,i}^n \right) \quad (\text{A.14}) \end{aligned}$$

A similar expression is produced for the R moment equation. This produces a local matrix equation to solve for new T unknowns.

Based on these equations, iterations on the value of T^* and unknowns ϕ^{n+1} and T^{n+1} can be performed to converge the nonlinearities of the system. The algorithm for solving the LO equations, with iteration index l , is defined as

1. Initialize $T^{*,l}$ unknowns using T^n or the last estimate of T^{n+1} from previous LO solve
2. Build the LO system based on the effective scattering $(1 - f^{*,l})$ and emission terms evaluated using $T^{*,l}$.
3. Solve the linearized LO system to produce a new estimate $\phi^{n+1,l+1}$.
4. Evaluate a new estimate of $T^{n+1,l+1}$ with energy update equations, e.g., Eq. (A.14).
5. $T^{*,l+1} \leftarrow T^{n+1,l+1}$.
6. Repeat 2-5 until $(T^{n+1,l})^4$ and $\phi^{n+1,l}$ are converged.

Convergence is based on the relative L_2 spatial norm of the change in $\phi^{n+1,l}$ and the emission source $\sigma_{ac}(T^{n+1,l})^4$.

A.2.1 Damped Newton Iterations

The algorithm in the previous section can be modified to improve the stability of convergence by including a fixed damping factor ξ . In this work, the Newton's method is formulated to directly estimate the final solution each step, rather than in terms of the change in the solution between steps. Thus, an intermediate solve based on the algorithm in the previous section is performed, followed by a damped update of the unknowns. The damped Newton's method algorithm is as follows:

1. Choose a damping factor $\xi \in (0, 1)$
2. Initialize $T^{*,l}$ unknowns using T^n or the last estimate of T^{n+1} from previous LO solve.
3. Build the LO system based on the effective scattering $(1 - f^{*,l})$ and emission terms evaluated using $T^{*,l}$.
4. Solve the linearized LO system to produce an estimate $\phi^{n+1,l+1/2}$.
5. Evaluate a new estimate of $T^{n+1,l+1/2}$ with energy update equations, e.g., Eq. (A.14).
6. Compute new temperatures and intensities as

$$\begin{aligned}\phi^{n+1,l+1} &= \phi^{n+1,l} + \xi (\phi^{n+1,l+1/2} - \phi^{n+1,l}) \\ T^{n+1,l+1} &= T^{n+1,l} + \xi (T^{n+1,l+1/2} - T^{n+1,l})\end{aligned}$$

7. $T^{*,l+1} \leftarrow T^{n+1,l}$.

8. Repeat 2-5 until $(T^{n+1,l})^4$ and $\phi^{n+1,l}$ are converged.

A.3 Analytic Error Contribution for LDD Trial Space

In this section, the treatment of the outflow discontinuity residual source and error tallying is detailed. Define the additional error contribution from the face sources at $x_{i+1/2}$ as $\delta\epsilon^{(m)}$. We have chosen to tally the contribution from these sources with MC everywhere except for at $x_{i+1/2}$. Thus, we need to solve for $\delta\epsilon^{(m)}$ at each face $x_{i+1/2}$ and add that contribution to the tallies $\epsilon(x_{i+1/2}, \mu)$, which include the contribution from all other sources. The transport equation satisfied by $\delta\epsilon^{(m)}$, for positive μ and effective total cross section $\hat{\sigma}_t$, is

$$\mu \frac{\partial \delta\epsilon^{(m)}}{\partial x} + \hat{\sigma}_t \delta\epsilon^{(m)} = r_{\text{face}}(x_{i+1/2}^-) \delta^-(x - x_{i+1/2}) + r_{\text{face}}(x_{i+1/2}^+) \delta^+(x - x_{i+1/2}) \quad (\text{A.15})$$

This equation is integrated from $x_{i+1/2} - \alpha$ to $x_{i+1/2}$ to produce

$$\begin{aligned} \mu \delta\epsilon^{(m)}(x_{i+1/2}, \mu) - \mu \delta\epsilon^{(m)}(x_{i+1/2} - \alpha, \mu) + \int_{x_{i+1/2} - \alpha}^0 \hat{\sigma}_t \delta\epsilon^{(m)} dx \\ = r_{\text{face}}(x_{i+1/2}^-) + \int_{x_{i+1/2} - \alpha}^0 r_{\text{face}}(x_{i+1/2}^+) \delta^+(x - x_{i+1/2}) dx. \end{aligned} \quad (\text{A.16})$$

The integral on the right side of the equation is zero because $\delta^+(x - x_{i+1/2})$ is zero for $(-\infty, x_{i+1/2}]$. The limit of the above equation is taken as $\alpha \rightarrow 0$, i.e.,

$$\lim_{\alpha \rightarrow 0} \left(\mu \delta\epsilon^{(m)}(x_{i+1/2}, \mu) - \mu \delta\epsilon^{(m)}(x_{i+1/2} - \alpha, \mu) + \int_{x_{i+1/2} - \alpha}^0 \hat{\sigma}_t \delta\epsilon^{(m)} dx \right) = \lim_{\alpha \rightarrow 0} r_{\text{face}}(x_{i+1/2}^-) \quad (\text{A.17})$$

The integral goes to zero because $\delta\epsilon^{(m)}$ is smooth on the interior of the cell, and $\mu\delta\epsilon^{(m)}(x_{i+1/2} - \alpha, \mu)$ goes to zero because there is no source upstream of $x_{i+1/2}^-$. Thus, the final solution is

$$\delta\epsilon^{(m)}(x_{i+1/2}, \mu) = \frac{r_{\text{face}}(x_{i+1/2}^-)}{\mu} = \tilde{I}^{(m)}(x_{i+1/2}^-, \mu) - \tilde{I}^{(m)}(x_{i+1/2}, \mu). \quad (\text{A.18})$$

The update equation for $I(x_{i+1/2}, \mu)$ is thus

$$\tilde{I}^{(m+1)}(x_{i+1/2}, \mu) = \tilde{I}^{(m)}(x_{i+1/2}, \mu) + \epsilon^{(m)}(x_{i+1/2}, \mu) + \delta\epsilon^{(m)}(x_{i+1/2}, \mu) \quad (\text{A.19})$$

$$= \tilde{I}^{(m)}(x_{i+1/2}^-, \mu) + \epsilon^{(m)}(x_{i+1/2}, \mu). \quad (\text{A.20})$$

A.4 Analytic Neutronics answer for Source fixup

In this section we model a fixed-source, pure-absorber neutronics calculation where we know the analytic answer to test our fixup. If we make the mesh thick enough, we can set the floor value to be the equilibrium answer $I(x) = \frac{q(x)}{2\sigma_a}$. For a general isotropic source $Q(x)$, the 1D transport equation to be solved is

$$\mu \frac{\partial I}{\partial x} + \sigma_a I(x, \mu) = \frac{q(x)}{2} \quad (\text{A.21})$$

with boundary condition $I(0, \mu) = I_{\text{inc}}$, $\mu > 0$ and $I(x_R, \mu) = \frac{q(x_R)}{2\sigma_a}$ for $\mu < 0$, where x_R is the right boundary. This first order differential equation is solved using an integration factor. The solution to this equation for $\mu > 0$ is given by

$$I(x, \mu) = I_{\text{inc}} e^{\frac{-\sigma_a x}{\mu}} + \int_0^x \frac{q(x')}{2\mu} e^{\frac{-\sigma_a(x-x')}{\mu}} dx', \quad \mu > 0 \quad (\text{A.22})$$

Integration of this result over the positive half range of μ gives

$$\phi^+(x) = I_{inc} E_2(\sigma_a x) + \frac{1}{2} \int_0^x q(x') E_1[\sigma_a(x - x')] dx'. \quad (A.23)$$

In the simplification of a constant source, the integral reduces to

$$\phi^+(x) = I_{inc} E_2(\sigma_a x) + \frac{q}{2\sigma_a} (1 - E_2(\sigma_a x)). \quad (A.24)$$

Also, for a constant source the solution for the negative half range becomes a constant, i.e.,

$$\phi^-(x) = \frac{q}{\sigma_a} \quad (A.25)$$

Combination of the above two equations gives the solution for the mean intensity:

$$\phi(x) = I_{inc} E_2(\sigma_a x) + \frac{q}{2\sigma_a} (1 - E_2(\sigma_a x)) + \frac{q}{\sigma_a}. \quad (A.26)$$

This expression can be integrated over any spatial cell, via quadrature, to accurately approximate moments of the mean intensity.

A.4.1 Spatially Varying Cross Sections

To test the fixup we want to imitated the two-material problem in Sec. ??, but with an analytic answer. We will set the floor to zero, as that is the easiest case. We do not have an internal source to simplify evaluation of the integrals. The derivation proceeds the same as in the above section, but now the integration factor is $\exp(\int_0^x \sigma_a(x')/\mu dx')$. With no internal volumetric source and no boundary source for negative μ , the solution becomes

$$\phi(x) = I_{inc} E_2 \left(\int_0^x \sigma_a(x') dx' \right) \quad (A.27)$$

where the argument of E_2 is clearly just the total number of mfps traveled up to that point.

To include an internal volumetric source, we can make the source $q(x) = q_0\sigma_a(x)$. This will ensure that the negative half range in negative μ , the solution is $q_0/2$.

APPENDIX B

DERIVATION OF THE WLA-DSA EQUATIONS

In this section, we derive the discretized diffusion equation and LD mapping equations that are used in the WLA-DSA equations. To simplify notation, we derive the equations from a generic transport equation (rather than the error equations) with isotropic scattering and source q_0 , i.e.,

$$\mu \frac{\partial I}{\partial x} + \sigma_t I = \frac{\sigma_s}{2} (\phi(x) + q_0). \quad (\text{B.1})$$

B.1 Forming a Continuous Diffusion Equation

First, a continuous spatial discretization of a diffusion equation is derived. The mean intensity ϕ will ultimately be assumed continuous at faces to produce a standard three-point finite-difference diffusion discretization. The zeroth and first μ moment of Eq. (B.1) produce the P_1 equations [22, 38], i.e.,

$$\frac{\partial J}{\partial x} + \sigma_a \phi = q_0 \quad (\text{B.2})$$

$$\sigma_t J + \frac{1}{3} \frac{\partial \phi}{\partial x} = 0. \quad (\text{B.3})$$

The spatial finite element moments (defined by Eq. (3.3) and (??)) are taken of the above equations. The mean intensity is assumed linear on the interior of the cell, i.e., $\phi(x) = \phi_L b_L(x) + \phi_R b_R(x)$, for $x \in (x_{i-1/2}, x_{i+1/2})$. Taking the left moment, evaluating integrals, and rearranging yields

$$J_i - J_{i-1/2} + \frac{\sigma_{a,i} h_i}{2} \left(\frac{2}{3} \phi_{L,i} + \frac{1}{3} \phi_{R,i} \right) = \frac{h_i}{2} \langle q \rangle_{L,i}, \quad (\text{B.4})$$

where J_i is the average of the flux J over the cell. The moments of q are not simplified to be compatible with the error equations which are in terms of moments. For the R moment

$$J_{i+1/2} - J_i + \frac{\sigma_{a,i} h_i}{2} \left(\frac{2}{3} \phi_{L,i} + \frac{1}{3} \phi_{R,i} \right) = \frac{h_i}{2} \langle q \rangle_{R,i} . \quad (\text{B.5})$$

The equation for the L moment is evaluated for cell $i+1$ and added to the R moment equation evaluated at i . The flux J is assumed continuous at $i+1/2$ to eliminate the face fluxes from the equations. The sum of the two equations becomes

$$J_{i+1} - J_i + \frac{\sigma_{a,i+1} h_{i+1}}{2} \left(\frac{2}{3} \phi_{L,i+1} + \frac{1}{3} \phi_{R,i+1} \right) + \frac{\sigma_{a,i} h_i}{2} \left(\frac{1}{3} \phi_{L,i} + \frac{2}{3} \phi_{R,i} \right) = \frac{h}{2} (\langle q \rangle_{L,i+1} + \langle q \rangle_{R,i}) . \quad (\text{B.6})$$

The mean intensity is approximated as continuous at each face, i.e., $\phi_{L,i+1} = \phi_{R,i} \equiv \phi_{i+1/2}$. Adding the L and R moments of Eq. (B.3) together, with the continuous approximation for $\phi_{i+1/2}$, produces a discrete Fick's law equation [33]

$$J_i = -D_i \frac{\phi_{i+1/2} - \phi_{i-1/2}}{h_i}, \quad (\text{B.7})$$

where $D_i = 1/(3\sigma_{t,i})$. Substitution of Eq. (B.7) into Eq. (B.6) and rearranging yields the following discrete diffusion equation:

$$\begin{aligned} \left(\frac{\sigma_{a,i+1} h_{i+1}}{6} - \frac{D_{i+1}}{h_{i+1}} \right) \phi_{i+3/2} + \left(\frac{D_{i+1}}{h_{i+1}} + \frac{D_i}{h_i} + \frac{\sigma_{a,i+1} h_{i+1}}{3} + \frac{\sigma_{a,i} h_i}{3} \right) \phi_{i+1/2} \\ + \left(\frac{\sigma_{a,i} h_i}{6} - \frac{D_i}{h_i} \right) \phi_{i-1/2} = \frac{h_{i+1}}{2} \langle q \rangle_{L,i+1} + \frac{h_i}{2} \langle q \rangle_{R,i} . \end{aligned} \quad (\text{B.8})$$

To allow for the use of lumped or standard LD in these equations, we introduce the factor θ , with $\theta = 1/3$ for standard LD, and $\theta = 1$ for lumped LD. The diffusion

equation becomes

$$\begin{aligned} & \left(\frac{\sigma_{a,i+1}h_{i+1}}{4} (1 - \theta) - \frac{D_{i+1}}{h_{i+1}} \right) \phi_{i+3/2} + \left(\frac{D_{i+1}}{h_{i+1}} + \frac{D_i}{h_i} + \left(\frac{1 + \theta}{2} \right) \left[\frac{\sigma_{a,i+1}h_{i+1}}{2} + \frac{\sigma_{a,i}h_i}{2} \right] \right) \phi_{i+1/2} \\ & + \left(\frac{\sigma_{a,i}h_i}{4} (1 - \theta) - \frac{D_i}{h_i} \right) \phi_{i-1/2} = \frac{h_{i+1}}{2} \langle q \rangle_{L,i+1} + \frac{h_i}{2} \langle q \rangle_{R,i} . \quad (\text{B.9}) \end{aligned}$$

Summation over all cells forms a system of equations for ϕ at each face.

B.1.1 Diffusion Boundary Conditions

The upwinding in the LO system exactly satisfies the inflow boundary conditions, therefore a vacuum boundary condition is applied to the diffusion error equations. The equation for the left moment at the first cell is given by

$$J_1 - J_{1/2} + \frac{\sigma_{a,i}h_i}{2} \left(\frac{1 + \theta}{2} \phi_{L,i} + \frac{1 - \theta}{2} \phi_{R,i} \right) = \frac{h_i}{2} \langle q \rangle_{L,i} , \quad (\text{B.10})$$

The Marshak boundary condition for the vacuum inflow at face $x_{1/2}$ is given as

$$J_{1/2}^+ = 0 = \frac{\phi_{1/2}}{4} + \frac{J_{1/2}}{2}, \quad (\text{B.11})$$

which can be solved for $J_{1/2}$. Substitution of the above equation and Eq. (B.7) into Eq. (B.10) gives

$$\left(\frac{1}{2} + \sigma_{a,1}h_1 \frac{1 + \theta}{4} - \frac{D_1}{h_1} \right) \phi_{1/2} + \left(\sigma_{a,1}h_1 \frac{1 - \theta}{4} - \frac{D_1}{h_1} \right) \phi_{3/2} = \frac{h_1}{2} \langle q \rangle_{L,1} \quad (\text{B.12})$$

A similar expression can be derived for the right-most cell.

B.2 Mapping Solution onto LD Unknowns

Solution of the continuous diffusion equation will provide an approximation to ϕ on faces, denoted as $\phi_{i+1/2}^C$. We now need to map the face solution onto the LD

representation of ϕ . To do this, first we take the L and R finite element moments of the P_1 equations. A LDFE dependence is assumed on the interior of the cell for J and ϕ . Taking moments of Eq. (B.2) and simplifying yields

$$J_{i+1/2} - \frac{J_{L,i} + J_{R,i}}{2} + \frac{\sigma_{a,i} h_i}{2} \left(\frac{1}{3} \phi_{L,i} + \frac{2}{3} \phi_{R,i} \right) = \frac{h_i}{2} \langle q \rangle_{R,i} \quad (\text{B.13})$$

$$\frac{J_{L,i} + J_{R,i}}{2} - J_{i-1/2} + \frac{\sigma_{a,i} h_i}{2} \left(\frac{2}{3} \phi_{L,i} + \frac{1}{3} \phi_{R,i} \right) = \frac{h_i}{2} \langle q \rangle_{L,i} \quad (\text{B.14})$$

The moment equations for Eq. (B.3) are

$$\frac{1}{3} \left(\phi_{i+1/2} - \frac{\phi_{i,L} + \phi_{i,R}}{2} \right) + \frac{\sigma_{t,i} h_i}{2} \left(\frac{1}{3} J_{L,i} + \frac{2}{3} J_{R,i} \right) = 0 \quad (\text{B.15})$$

$$\frac{1}{3} \left(\frac{\phi_{i,L} + \phi_{i,R}}{2} - \phi_{i-1/2} \right) + \frac{\sigma_{t,i} h_i}{2} \left(\frac{2}{3} J_{L,i} + \frac{1}{3} J_{R,i} \right) = 0 \quad (\text{B.16})$$

The face terms $J_{i\pm 1/2}$ and $\phi_{i\pm 1/2}$ need to be eliminated from the system. First, the scalar intensity is assumed to be the value provided by the continuous diffusion solution at each face, i.e., $\phi_{i\pm 1/2} = \phi_{i\pm 1/2}^C$. Then, the fluxes are decomposed into half-range values to decouple the equations between cells. At $x_{i+1/2}$, the flux is composed as $J_{i+1/2} = J_{i+1/2}^+ + J_{i+1/2}^-$, noting that in this notation the half-range fluxes are $J_{i+1/2}^\pm = \pm \int_0^\pm \mu I(x_{i+1/2}, \mu) d\mu$ ¹. We approximate the incoming fluxes, e.g., $J_{i+1/2}^-$, based on $\phi_{i+1/2}^C$ and a P_1 approximation. The P_1 approximation provides the following relation [38]

$$\phi = 2(J^+ - J^-). \quad (\text{B.17})$$

At $x_{i+1/2}$, the above expression is solved for the incoming current $J_{i+1/2}^-$. The total

¹Typically, the half-range fluxes are defined with integrals weighted with $|\mu|$, but this notation would not be consistent with our definition of the half-range consistency terms

current becomes

$$J_{i+1/2} = J_{i+1/2}^+ - J_{i+1/2}^- = 2J_{i+1/2}^+ - \frac{\phi_{i+1/2}^C}{2}, \quad (\text{B.18})$$

In the positive direction, at the right face, the values of ϕ and J are based on the LD representation within the cell at that face, i.e., $\phi_{R,i}$ and $J_{R,i}$. The standard P_1 approximation for the half-range fluxes is used[33], i.e.,

$$J^\pm = \frac{\gamma\phi}{2} \pm \frac{J}{2}, \quad (\text{B.19})$$

where γ accounts for the difference between the LO parameters and the true P_1 approximation. Thus, for the right face and positive half-range,

$$J_{i+1/2}^+ = \frac{\gamma}{2}\phi_{i,R} + \frac{J_{i,R}}{2} \quad (\text{B.20})$$

A similar expression can be derived for $x_{i-1/2}$. The total fluxes at each face are thus

$$J_{i+1/2} = \gamma\phi_{i,R} + J_{i,R} - \frac{\phi_{i+1/2}^C}{2} \quad (\text{B.21})$$

$$J_{i-1/2} = \frac{\phi_{i-1/2}^C}{2} - \gamma\phi_{i,L} + J_{i,L} \quad (\text{B.22})$$

Substitution of these results back into the LD balance equations and introduction of the lumping notation yields the final equations

$$\left(\gamma\phi_{i,R} + J_{i,R} - \frac{\phi_{i+1/2}^C}{2} \right) - \frac{J_{L,i} + J_{R,i}}{2} + \frac{\sigma_{a,i}h_i}{2} \left(\frac{(1-\theta)}{2}\phi_{L,i} + \frac{(1+\theta)}{2}\phi_{R,i} \right) = \frac{h_i}{2}\langle q \rangle_{R,i} \quad (\text{B.23})$$

$$\frac{J_{L,i} + J_{R,i}}{2} - \left(\frac{\phi_{i-1/2}^C}{2} - \gamma \phi_{i,L} + J_{i,L} \right) + \frac{\sigma_{a,i} h_i}{2} \left(\frac{(1+\theta)}{2} \phi_{L,i} + \frac{(1-\theta)}{2} \phi_{R,i} \right) = \frac{h_i}{2} \langle q \rangle_{L,i} \quad (\text{B.24})$$

$$\frac{1}{3} \left(\phi_{i+1/2}^C - \frac{\phi_{i,L} + \phi_{i,R}}{2} \right) + \frac{\sigma_{t,i} h_i}{2} \left(\frac{(1-\theta)}{2} J_{L,i} + \frac{(1+\theta)}{2} J_{R,i} \right) = 0 \quad (\text{B.25})$$

$$\frac{1}{3} \left(\frac{\phi_{i,L} + \phi_{i,R}}{2} - \phi_{i-1/2}^C \right) + \frac{\sigma_{t,i} h_i}{2} \left(\frac{(1+\theta)}{2} J_{L,i} + \frac{(1-\theta)}{2} J_{R,i} \right) = 0. \quad (\text{B.26})$$

The above equations are completely local to each cell and fully defined, including for boundary cells. For simplicity, we just take $\gamma = 1/2$. The system can be solved for the desired unknowns $\phi_{i,L}$, $\phi_{i,R}$, $J_{i,L}$, and $J_{i,R}$, which represent the mapping of $\phi_{i+1/2}^C$ onto the LD representation for $\phi^\pm(x)$.